FUNCTIONAL MATERIALS FOR THERMAL MANAGEMENT APPLICATIONS

A Dissertation

by

NIRUP KUMAR NAGABANDI

Submitted to the Office of Graduate and Professional Studies of
Texas A&M University
in partial fulfillment of the requirements for the degree of

DOCTOR OF PHILOSOPHY

Chair of Committee,	Mustafa Akbulut
Committee Members,	Micah Green
	Jodie Lutkenhaus
	Oleg Ozerov
Head of Department,	Nazmul Karim

December 2017

Major Subject: Chemical Engineering

ABSTRACT

The inefficient dissipation of heat is a crucial problem that limits the reliability and performance of all electronic systems. As electronic devices get smaller and more powerful, and moving components of machinery operate at higher speeds, the need for better thermal management strategies is becoming increasingly important. Heat removal during the operation of electronic, electrochemical, and mechanical devices is facilitated by high-performance thermal interface materials (TIMs), which are utilized to couple devices to heat sinks. Herein, we report a new class of TIMs involving the chemical integration of boron nitride nanosheets (BNNS), soft organic linkers, and a metal matrix - which are prepared by chemisorption coupled electrodeposition approach. Thermal and mechanical characterization of the copper-based hybrid nanocomposites involving thiosemicarbazide demonstrates bulk thermal conductivities ranging from 211 to 277 W/(m.K), which are very high considering their relatively low elastic modulus values on the order of 15 to 30 GPa. The synergistic combination of these properties leads to the lowest measured total thermal resistivity to date for a TIM with a typical bondline thickness of 30-50 μm: 0.38 to 0.56 mm^2.K/W. Moreover, its coefficient of thermal expansion (CTE) is 11 ppm/K, forming a mediation zone with a low thermally-induced axial stress due to its close proximity to the CTE of most coupling surfaces needing thermal management. Furthermore, preliminary electrochemical tests revealed that the presence of organic ligands and BNNS in the hybrid nanocomposite TIMs improves the corrosion protection behavior of the TIMs by nearly 72%.

Further analysis of the hybrid nanocomposite TIMs included the replacement of thiosemicarbazide with various organic ligands and the replacement of copper matrix with silver. Compared to all the ligands that were used in copper-based hybrid nanocomposites, the most promising thermal and mechanical test results were obtained from thiosemicarbazide. On the other hand, the best silver-based nanocomposite TIM was determined to be the one involving the ligand 2-mercapto-5-benzimidazolecarboxylic acid, in which the thermal conductivity was near 360 W/m.K, and elastic modulus and hardness were about 35 GPa and 0.25 GPa, respectively. The promising results indicate that metal-inorganic-organic nanocomposite TIMs can be great alternatives to currently used TIMs in the market.

Additionally, polystannane nanocomposite involving graphene nano particles as fillers were synthesized, which showed thermal conductivities up to 40 W/m.K at 10 wt% loading. Also, these composites were found to have higher stability in ambient conditions towards humidity and light where the degradation kinetics of first order showed 10-fold decrease in rate constant. These improvements in thermal properties and stability can allow the polymeric metals in application towards thermal management.

DEDICATION

The humankind has come from living in tribes in forests to endeavoring on to Mars but there still exist a lot of underprivileged children who are unable to get the basic education. I dedicate this work to all the children who are unable to access basic education in hope that this will change soon.

ACKNOWLEDGEMENTS

Firstly, I take this chance to thank my advisor Dr. Mustafa Akbulut. He has been an exceptional mentor to me. He is tremendous support in research and professional life by guiding me at every step. Not just research, but he has played a great role in my overall progress as a graduate student and be ready to do independent research as I go forward. I think I did the first part of the saying, “work under great boss to become great.”

I would also like to thank my committee members, Dr. Micah Green for being so engaging and letting me work with his students and in his lab for broader understanding of things. Dr. Jodie Lutkenhaus for letting me use the equipment in her lab as and when I ask. And Dr. Oleg Ozerov for agreeing to be part my committee immediately and constant support throughout.

Next, I thank Dr.Cengiz Yegin, for working with me in my first 3 years and giving invaluable advice whenever possible. Also, for being accommodative in all the hard times of work and making my journey much smoother than it could be. I also want to thank other members of my group, Dr.Ming Zhang for helping me in many experiments in my initial days and later on. Dr. I-Cheng Chen for his research inputs on several occasions. Dr. Jun-Kyun-Oh for helping me in the lab and research whenever I asked for. Dr. Blake Teipel for providing me invaluable inputs in all aspects of life including research. Also, Yagmur Yegin, Varsha Talari, Li Hao, Shuhao Li for sharing all moments in the lab and always being there to share thoughts and light moments.

I thank our collaborators at National Renewable Energy Laboratories (NREL), Colorado. Especially Dr. Sreekanth Narumanchi for his valuable inputs regarding papers

and research in characterizing our samples and Dr. Xuhui Feng for conducting all our experiments at NREL and analyzing the results for us. A special thanks to our collaborators Dr. A.V. Sokolov from astronomy and physics department at Texas A&M university and Dr. Lei Fang from chemistry department.

I also want to take this opportunity to thank the staff and technical personnel at the MCF, MIC and chemical engineering for helping promptly whenever required and providing hassle free work environment.

Finally, words cannot express how grateful I am to my mother and father for supporting me throughout my life. My uncle and aunt for being great mentors in my life and becoming second father and mother in my life.

CONTRIBUTORS AND FUNDING SOURCES

This work was supervised by a dissertation committee consisting of Dr. Mustafa Akbulut (chair), Dr. Micah Green and Dr. Jodie Lutkenhaus of the Artie McFerrin Department of Chemical Engineering., and Dr. Oleg Ozerov of the Department of Chemistry.

All work for the dissertation was completed by the student, in collaboration with Cengiz Yegin of the Department of Materials Science and Engineering. Also certain experimental contributions were made by Dr. Alexei Sokolov and Ansam Talib of the Department of Physics and Astronomy, Dr. Stanislav Verkhoturov of the Materials Characterization Facility and Dr Lei Fang and Mariela Vazquez from Department of Chemistry with in Texas A&M University. Collaborators outside of Texas A&M helped experimentally are Dr. Xuhui Feng, Dr. Charlie King and Dr. Sreekant Narumanchi of National Renewable Energy Laboratory (Golden CO), Dr. Massimo Catalano and Dr. Moon J. Kim of the University of Texas at Dallas.

This work was made possible in part by DARPA of the U.S. Department of Defense under Grant Number D13AP00040. Its contents are solely the responsibility of the authors and do not necessarily represent the official views of the DARPA.

NOMENCLATURE

A	Hamaker Constant
AFM	Atomic force microscopy
ATR-FTIR	Attenuated total reflectance-Fourier transform infrared
BNNS	Boron nitride nanosheets
C_p	Specific heat capacity
CTE	Coefficient of thermal expansion
DLF	Discovery laser flash
DLS	Dynamic light scattering
E	Elastic modulus
E_r	Reduced elastic modulus
EDS	Energy dispersive X-ray spectroscopy
EDTA	Ethylenediamine tetraacetic acid
ESEM	Environmental scanning electron microscopy
f-BNNS	Functionalized boron nitride nanosheets
GNP	Graphene nanoparticles
GPa	Gigapascal
H	Hardness
h-BN	Hexagonal boron nitride
k	Boltzmann constant
K	Thermal conductivity
LFD	Laser flash diffusivity

NMR	Nuclear magnetic resonance
NPs	Nanoparticles
OP	Over-potential
OTS	Octadecyltrichlorisilane
pK_a	Acid dissociation constant
PolySn	Polystannane
p-TC	p-toluoyl chloride
PVB	Polyvinyl butyral
PEG-D	Polyethylene glycol dithiol
PSTTR	Phase sensitive transient thermoreflectance
R	Resistance
SEM	Scanning electron microscopy
SIMS	Secondary ion mass spectrometry
T	Temperature
TD	Terepthalic dihydrazide
TEM	Transmission electron microscopy
TGA	Thermogravimetric analysis
TIM	Thermal interface material
TSC	Thiosemicarbazide
XPS	X-ray photoelectron spectroscopy
vdW	van der Waals
2-MBC	2-mercapto-5-benzimidazole carboxylic acid

4-ABT	4-aminobenzenethiol
4-BBC	4-bromobenzoyl chloride
4-CBC	4-cyanobenzoyl chloride
4-MBA	4-mercaptobenzoic acid
4-MPA	4-mercaptopropionic acid
4-MT	4-mercaptotoulene
4-NBC	4-nitrobenzoyl chloride
α	Thermal diffusivity
ρ	Density
υ	Poisson`s ratio

TABLE OF CONTENTS

Page

LIST OF FIGURES

LIST OF TABLES

1. INTRODUCTION

1.1 Objective

The objective of this work is to synthesize advanced materials that can be considered as the next generation materials in the field of thermal management. The work focuses on thermal interface materials (TIM) which are essential in conductive heat transfer for thermal management in various fields like electronics, communications, power storage, invertors and lighting systems.

To realize the objective, two novel nanocomposite materials were synthesized involving metals like copper, silver, tin and 2-D nanoparticles of boron nitride and graphene. The first material is a metallic- organic-inorganic nanocomposite with boron nitride nanosheets dispersed in copper or silver matrices and qualify as a totally new class of thermal interface materials. The second material is a nanocomposite of graphene nanosheets and polymeric tin which falls in to the category of polymeric TIMs but totally outclasses the currently available materials in terms of properties. In both cases, the relevant properties clearly establish that these materials are true next generation thermal interface materials.

1.2 Motivation

In an electronic ensemble, the most important part is a chip which is made up of transistors and capacitors of finite resistance and they produce heat each time the electrons flow through them in the form of current to carry out the defined task[1]. A chip has a finite life time and operating it at higher than optimal temperature will quickly reduce the life

time and performance of the chip[2]. Michael Allen[3] reported that the operating life of a capacitor, a integral component of a chip degrades exponentially with operating temperature as shown in the Figure 1.

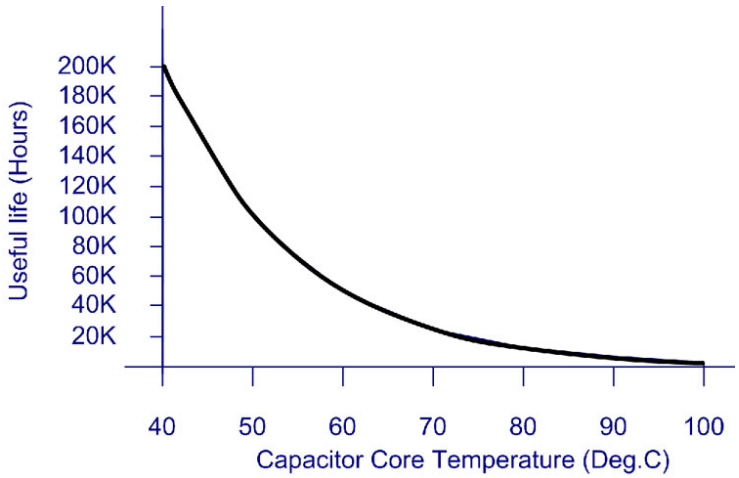

Figure 1 Graph showing the exponential decrease in the useful hours of a capacitor with increase in operating temperature[3]

A continuous operation of an electronic device will lead to continuous output of heat and it is important to remove the evolved heat to maintain the temperature of the chip. This removal of heat is typically achieved by conductive transfer to a heat sink[4,5], generally made up of copper or aluminum at the chip level and then convective cooling of the heat sink using fans or cooling liquids. As shown in the schematic of a chip in Figure 2, at the chip level, the chip is housed in a chip carrier to ensure no major mechanical stress is felt on the chip due to thermal expansions and be able to use ruggedly. The heat produced by

the chip is transported to the out of chip carrier via conduction, convection and radiation. The top or bottom of the chip carrier is connected to the heat sink via TIM.

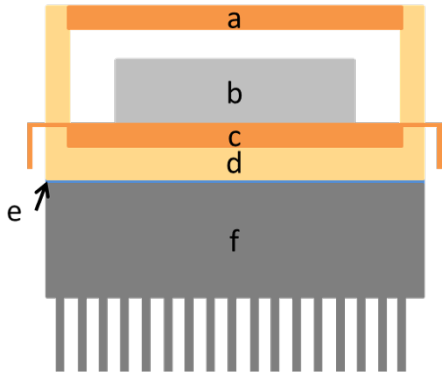

Figure 2 Schematic Figure of a chip. a) Lid b) Chip c) DBC with electrical connections d) Chip Carrier e) TIM f) Heat sink with fins

TIM is used as a connector because of the micro/nano roughness and rigidness of the heat source and sink doesn't allow full contact between them for thermal transport. As we know that any two rigid planar objects can be in contact only at finite number of points[6], when these two rough surfaces are got in to contact, effective area of contact for thermal transport is greatly lesser than the actual area and the gaps are filled by air which is much less thermally conductive thermally. Application of a TIM, which is a soft but conducting material in between these surfaces improves the overall system by confirming in to the asperities and replacing air. The utility of a TIM is illustrated in the Figure 3.

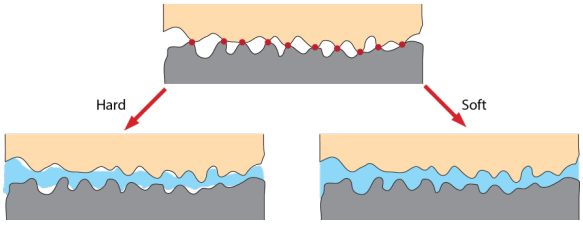

Figure 3 Schematic showing the advantage of TIMs

As per Moore's law[7], the number of transistors on a chip doubles every year which also indirectly suggests that the amount of heat emitted from a chip increases. The semiconductor industry created break through up on break through to keep up with Moore's has and increased the number of transistors on a chip to 1.2 billion in 2011 compared to 2300 in 1971[8]. This trend can be easily understood by looking at Figure 4 which shows the number of transistors on a chip introduced in specific years by intel corporation.

This chip development aided by the miniaturization of devices has led to emission of higher and higher amounts of heat flux but on the contrary the development on the side of TIMs wasn't as impressive. For example, the thermal resistance, an important metric for thermal interface materials of best TIM on market has only reduced from 25 W/m.K in 1995 to 10 W/m.K in 2014 across all classes of TIMs compared to the heat output of the intel chip released during the same period has changed from 30 W to 150 W. This slow development of TIMs has caused the developed chips to be used with less reliability and often led to the failure of miniature and heavy application devices. Also the development of high performance systems and electronic clusters in other fields like power storage,

automobiles, communications, LEDs, military equipment and aviation demands for the immediate development of TIMs for more reliability and further development of these systems[9–19]. To this end, we had targeted to synthesize TIMs which can exhibit a thermal resistance of 0.1 W/m.K, a order magnitude lower than the currently available best TIMs across all classes, which typically are in the range of 5-10 W/m.K.

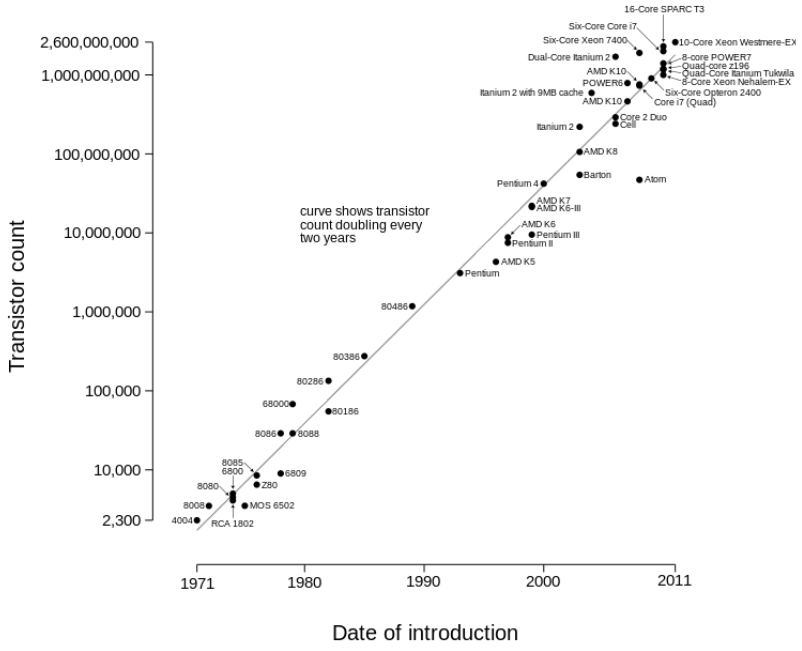

Figure 4 Development of the intel chips used in personal computers[8]

1.3 Dissertation Layout

The dissertation starts off with "introduction chapter", where the reader is introduced the to objective of this work and why this the author has decided to work on this objective. It also introduced what is a TIM and clearly conveys that two new

nanocomposite TIMs were synthesized in this work. Next the "chapter of literature and concepts" helps the reader to understand various concepts used in this work and also relevant literature about TIMs and Boron nitride.

Chapter three discusses about the approach to create a metallic-organic-inorganic nanocomposites and how the approach was used to synthesis copper based TIMs. Chapter four talks about the several effects of organic linker on the properties of the copper based TIM synthesized in chapter three. Later on in chapter five, preparation of such TIMs with silver as base were discussed and similarly the effects of the organic molecules were discussed in addition to comparing the properties with the copper based TIMs. Chapter six then talks about the synthesis of second type of TIM, a nanocomposite of polymeric tin and graphene and how they can be used as TIMs. Conclusions are then presented in chapter seven in addition to some insights in to future work. Later in the Appendix A, principles of the important experimental techniques used in this work were discussed.

2. LITERATURE AND CONCEPTS

History is always important in order lay road for the future as it gives insights in to the available information and equips us on taking a more knowledgeable decision. In this light, I want to present some literature on TIMs and briefly comment on aspects of design of a material for application as a TIM. Later on in the chapter I will discuss about properties of boron nitride nanosheets and its functionalization, properties of graphene nanoparticles, electro deposition of metals and synthesis of poly stannate (PolySn) which will aid in better understanding of the overall script.

2.1 Thermal Interface Materials

2.1.1 Thermal resistance of a TIM

TIMs are bonding materials between heat sink and a heat source which improve the overall thermal transport across the interface[20]. Usage of TIMs majorly started with the advent of electronic devices to tackle the heat produced inside the chip chamber in order to keep the performance and life of the chip to optimum. When a TIM is applied between two surfaces, one important aspect is the thickness of the TIM, which is called bond-line thickness (BLT). As the heat flows through the heat source in to the TIM and then in to the heat sink due to the temperature difference, a finite resistance to this flow is encountered at the source-TIM interface ($R_{(source\text{-}TIM)}$), bulk of the TIM (R_{TIM}) and the TIM-sink interface ($R_{(TIM\text{-}sink)}$) through which the heat carriers have to travel[21,22]. So, the overall resistance (R_{total}) across the interface can be taken as the sum of these three

resistances in series as given in equation 1[23] and the objective any TIM is to minimize this overall resistance to maximize the heat transfer[24–26].

$$R_{total} = R_{(source-TIM)} + R_{TIM} + R_{(TIM-sink)} \quad (1)$$

The bulk thermal resistance of a material can be given by the equation 2 where k is the thermal conductivity of the material and the t is the thickness of the sample. In the case of a TIM, the thickness is BLT. Equation 3 gives an empirical relation for thermal resistance at interfaces[27,28], where where k_{int} is the harmonic mean thermal conductivity of the contacting surfaces, m is the effective absolute surface slope, σ is the effective rms roughness, P is the contact pressure, and H is the micro-hardness of the softer material. By combining equations 1 and 2, equation 4 can be written and by observing equation 3 and 4 it can be commented that the overall resistance is proportional to H/k of the TIM.

$$R_{TIM} = {}^{t}/_{k} = {}^{BLT}/_{k} \quad (2)$$

$${}^{1}/_{R_{interface}} = 1.25 k_{int} \, {}^{m}/_{\sigma} * ({}^{P}/_{H})^{0.95} \quad (3)$$

$$R_{total} = R_{(source-TIM)} + {}^{BLT}/_{k} + R_{(TIM-sink)} \quad (4)$$

2.1.2 Material design aspects of a TIM

The ideal TIM would have infinite conductance through the interface and offer least bulk resistance and to obtain most effective TIM, the idea is to reduce the overall resistance. By reading more in to the equations 3 and 4, the material design aspect is to obtain a material with high bulk thermal conductivity and a low micro-hardness. Though this is the most important metric, it is also essential that the TIM material shouldn't

corrode or react with the sink or source, have a long life for itself without degrading either chemically or property wise, mechanically tough enough to handle the thermal stresses caused by the thermal cycles of cooling and heating and have a coefficient of thermal expansion (CTE) that can bridge the sink and the source. In this work, though the emphasis was on obtaining the least thermal resistance possible out of a material which is the most important metric, other properties were also tested.

2.1.3 Types of TIMs

Three decades of research and manufacturing of TIMs during 1980's -2010's has given 1000s of TIMs but almost all of them can be classified in to 4 different classes namely solder TIMs, thermal greases, polymeric TIMs and phase change material (PCM) TIMs. Each class of TIMs have progressed over years but the progress has reached a saturation point due to certain limitations in these class of materials which will be discussed below. A few researches in last decade are taking a different approach with the advent of fundamental concepts in nano materials and produced TIMs which don't exactly fall in to any of the classical 4 types but these still possess drawbacks of their own.

Solder TIMs

Solders which typically are alloys of lead are low melting and posses high thermal conductivities in the range of 20 – 80 W/m/K[29–34] are used as a TIM because of the ease of application. Although tin/lead alloys have been the most commonly used solder[30], tertiary elements have been added depending on the specific needs such as addition of bismuth for lowering melting point and increase wettability[31,34], and addition of antimony for increasing the strength of the alloy[32,33]. But, due to high thickness and stiffness of the

solders, thermal stresses are developed[35] which compromise the overall device and led to the discontinued use of solders in todays world. Also, solders react with common heat sink materials like copper[36] to form intermetallic compounds which reduce the thermal conductivity and tackle the heat dissipation poorly. Though soft solder usage looks promising, they have poor thermal fatigue resistance[37] and hence solder of any kind doesn't sound great. Recent work by Dutta et al[29], suggested usage of indium in tin solders as cost effective, high thermal conductivity TIMs but authors didn't try to address mechanical issues associated with the solder.

Thermal grease

Thermal grease is two component based product, typically consisting a fluidic base and ceramic or metallic fillers for thermal conductivity. In thermal greases, thermally conductive fillers are typically dispersed in silicone, sodium silicate, or a hydrocarbon oil to form a paste[38,39]. As a filler, CNT,[40–42] diamond powder,[43] silver,[44] and copper,[45–47] beryllium oxide[48], aluminum nitride[49–51], aluminum oxide[49,51,52] and zinc oxide[45,53,54] have been employed in current thermal grease formulations. Being viscous liquids, thermal grease flow easily in to the voids of the mating surfaces and eliminate air thus creating a much better thermal pathway for heat to dissipate. Typical thermal conductivity value of these kind of TIMs is between 0.5 – 7 W/m/K[38-54]. In general a higher filler loading contributes to higher thermal conductivity but also increases viscosity and reduces wettability. As wettability is a key factor in these kind of TIMs, it limits the particle filler loading and hence the thermal conductivity. It is understood that optimized particle size distribution will give a lower viscous material for same filler loading compared to mono

dispersed filler particles.[55] But, they flow out up on application, which might contaminate other materials in the device. Also, there might be a pump out effect due to thermal cycling or dry out over time which will eventually result in rise of thermal resistance[56]. Study by Viswanath et al[57] found that the thermal resistance increases 4-6 times for 7500 cycles from 0 ^{o}C to 100 ^{o}C. Another study[58] reports a new type of grease based TIM, which is dry to touch, MicroFaze® and claims to be the first non-silicone thermal grease that can solve contamination and migration problems that are typically associated with silicone-based products but without any improvements in the thermal conductivity.

Phase Change Materials (PCM)

A PCM can be a homogenous or heterogeneous material which changes phase up on heating in the range of the electronic operating limit. PCMs are designed with the base as paraffin, polymer, co-polymer having suspensions of micro-macro particles of high thermal conductivity to change the phase near the optimal performance temperature. As the PCM melts, it turns in to a liquid or reduces viscosity and flows into the cavities in the interfacial region and occupies the air voids. Most cited PCMs theoretically show higher thermal performance than thermal greases and are easy to work with unlike thermal greases but the mechanical shocks and handling are not well studied. Moreover, the frequent changing of phase might result in reacting with mating surfaces and damage them[56]. Another class of PCMs is low melting alloys[59,60], based on bismuth, indium, gallium and tin[60] work similar to the solders but are low melting and hence fill in to the voids of the mating surfaces. Though cadmium, mercury and lead fall in same category of low melting point metals, these are avoided because of their toxicity[37]. Formation of

intermetallic compounds, corrosion due to oxidation may lead to the lower performance over time and eventually fail the device[59]. An interesting PCM is proposed by Chen[61] where the author coupled shape memory alloy (SMA) in to thermal grease. In the silver or silicon colloid which is thermal grease, several SMA fillers such as nano-CuNiTi, nano-CuAlZn, and nano-NiTiAlZ with particle diameters ranging from 10 to 100 nanometres are tried. It is theorized that, SMA changes its shape during temperature change and conforms on to mating surfaces. After initial treatments, SMA memorizes its relative position in the bulk layer of TIM with temperature and delivers required performance. However, the long term reliability and interaction with mating surfaces with PCM remains a challenge. PCMs have a typical thermal resistance of 10 Kmm^2/W. and in the range of 4 – 60 $K.mm^2/W$.

Filled Polymeric Matrices

These are most widely used TIMs in the electronics industry as these offer the performance of thermal greases but are much easier to work with and assemble. Polymer-matrix composite TIMs typically involve the addition of thermally conductive particles like silver[62], copper, aluminum nitride[63] and several other particles[37,49,64–69] into a polymer matrix like epoxy, polyurethane, and polyvinyl chloride. Recent studies have synthesized epoxy composite TIMs containing novel types of fillers such as graphite,[70] graphene,[71,72] and CNTs[73–76]. Though these TIMs presented few problems, there thermal conductivity remained in the range of 0.5 – 7 W/m/K. and a typical contact thermal resistance of 10 $K.mm^2/W$. and in the range of 3 – 80 $K.mm^2/W$.

Non-conventional TIMs

The past decade and a half has approached the problem of creating new TIMs in new ways which does not truly belong to any of the above four classes. In 2004, Quoc Ngo et al[77] presented the idea of using the arrays of carbon nano fibers (CNF) as a TIM by fabricating a vertically aligned free standing CNF on a silicon using PECVD[78] and then filling the gaps in this high aspect ratio array with copper via electroplating. This CNF-copper composite exhibited a contact thermal resistance of 25 $K.mm^2/W$ for BLTs of 30 micron. Though the value is not a great improvement from state of the art of the current TIMs, it paved a way forward for novel TIMs. Similar work is done with carbon nano tubes (CNT)[76,79] which exhibited a thermal resistances in the range of 20-30 $K.mm^2/W$. Recently, Tong et al[80] improvised the above concept by applying 1-micron indium layer at the ends of CNTs for better heat transport and reduced thermal resistance value to as low as 15 $K.mm^2/W$, forwarding the earlier research.[76–78] However, the challenges in this type of TIM lie in achieving uniform heat profile with 1-micron indium layer as it is not enough to conform to the mating surfaces. Xu et al further explored the idea by making layers of CNTs and PCM[81], which exhibited a contact thermal resistance as low as 5 $K.mm^2/W$ and later on just 4 $K.mm^2/W$ as measured by photoacoustic technique[82]. Another concept of double sided CNTs[76] also reported 5 $K.mm^2/W$. This new class of CNT array based materials looks promising as next generation TIMs but the challenge lies in the uniform production of CNT in mass scale without defects. A high thermal conductivity of 3000 W/m/K is reported[83] for MWCNT but also other studies[84,85] report 15 W/m/K and 27 W/m/K respectively as the thermal conductivity of CNT arrays fall

rapidly with the number of defects and impurities[86]. Typical defects are orientation mismatch and multiple contacts of the CNT arrays because of uncontrolled CVD growth. Large scale production of uniform CNTs remain a challenge which will have to be answered before this technology can develop further[87]. Also, most studies don't report the mechanical reliability of this class of materials which is very important. So, it is in future that, thermo-mechanical properties and reliability has to be well established.

Another new approach is the idea of making metals and polymers in to a composite material. Usage of metals for high thermal transport and polymers for their mechanical virtues is the basic idea. Carlberg et al[88] have presented the idea of incorporating metal-polymer nanocomposites by fabricating a highly porous polymeric matrix of TPE via electro-spinning and infusing it with low melting metal alloy (In/Bi/Sn) for continuous thermally conductive pathways. In addition to showing mechanical reliability they measured a thermal resistance as low as 8.5 K.mm^2/W at 70-micron BLT. By optimizing the polymeric matrix synthesis in the above work, Zanden et al[89] found that, thermal resistances as low as 1.5 K.mm^2/W can be obtained. A similar ideas used by Shuangxi Sun and co-workers[90] resulted in a TIM with a thermal resistance of less than 2 mm^2.K/W. Xin luo et al[91] reported TIMs made up of boron nitride nanofibers and indium. BNNFs for the basic structure by electrospinning which are infused with indium. This composite exhibits an in-plane thermal conductivity of 60 W/m K and a thermal resistance of just 1.2 mm^2.K/W. It is also important to note that, long term reliability of this technology has not been studied yet. Involvement of metals like indium, bismuth poses the risks of the low melting solders and low meting metal PCMs; contamination and pump out effects. Also,

the interaction of metal with polymer in high number of thermal cycles has to be characterized before this technology can move forward.

A different concept of nano-sponge was introduced by Wunderle[92], where the authors created a porous nano sponge of gold with reliable mechanical properties. Though the work doesn't report the thermal properties, it is understood that, being a high thermal conductivity metal, it will have low thermal resistance. However, questions remain about the grain coupling and Ostwald ripening[93] with several heating cycles and sponge being destroyed overtime to give hard material which will be anything opposite to a TIM rather than being a TIM.

Another important type of TIM is highly oriented pyrolytic graphite, which has very high thermal conductivity along the in-plane direction (600-1700 $W/m^2.K$) and low thermal conductivity in the out-of-plane direction (10-20 $W/m^2.K$). However, most thermal management applications require a high thermal conductivity in the out-of-plane (z-) direction between heat spreader and sink. While graphene-based TIMs achieved thermal resistances as low as 1.5×10^{-2} $mm^2.K/W$ at nanoscale,[11,94] their device scale forms and highly oriented pyrolytic graphite sheets with a thickness of 50-100 μm have been reported to result in a total resistance in the order of 20 $mm^2.K/W$.[95] The delamination and flaking off are other challenges associated with pyrolytic graphite sheets.

Recent work on TIMs[91,96–107] has mostly taken the direction of incorporating high aspect ratio fillers in to polymer matrices or infusing metals in to polymer matrices. Most famous choices for fillers are CNT, graphene and BNNS for their high thermal properties and modified CNT and BNNS as they offer different properties with modification which

can improve thermal transport by reducing boundary scattering of phonons and phonon-phonon scattering. But, none of the works with polymeric matrices report less than 5 $K.mm^2/W$ thermal resistances. Though new ideas are presented, most fall short in addressing the anticipated shortcomings like pump out, internal chemical degradation or reaction, long term reliability. So, it is essential to develop novel TIMs with much less thermal resistance, be reliable in long term and comply mechanically.

2.2 Approach to Create Novel TIM

There are two potential routes for reducing the total thermal resistance of TIMs that are needed to satisfy stringent thermal needs of emerging advanced applications: either by further improving the thermal properties of a compliant matrix, or by further improving the mechanical properties of a high-thermal-conductivity matrix. Currently, as the majority of research is focused on the former approach and we primarily targeted the novel approach of enhancing the mechanical properties of the metal matrix and then we also tried another novel approach of using a compliant conductive matrix and improving the properties and its workability.

Firstly, we developed a new class of nanocomposite TIMs by covalently integrating boron nitride nanosheets (BNNS) functionalized with soft organic linkers and a copper matrix. Here, BNNS is selected as filler because of its extremely high in-plane thermal conductivity (300-2000 W/(m.K)), low coefficient of thermal expansion, and superior thermal and chemical stability.[108–111] Copper is a well-known matrix material with high thermal conductivity. We were able to realize the synthesis of metal-BN composite which otherwise would be impossible via available compounding techniques

by developing a novel electro-co-deposition technique. Thus developed TIMs possessed thermal conductivities in the range of 220 – 300 W/m/K, atleast 5 times better than any of the currently available TIMs and also show thermal contact resistances of 0.06 - 0.1 mm2.K/W with an overall thermal resistance of 0.35 – 0.55 mm^2.K/W for a BLT of 30 to 50 microns, beating any current TIM by an order of magnitude.

Second, currently the polymeric matrices being used are carbon based which typically have a very low thermal conductivity and also have no possibility of synergistic combination for thermal transport. We use a unique metallic polymer, "polystannane" as the polymeric base to create a nanocomposite with graphene nanoparticles. Graphene is chosen here because of its intrinsic high thermal conductivity and light blocking ability. Though polystannate is a high conductive polymer, it is very sensitive to light and humidity and the typical life is less than an hour in ambient conditions before degrading in to oligomers of tin. By using graphene, we were able to improve the stability of the polymer to more than 24 hours in ambient conditions besides improving the thermal conductivity 10 fold.

2.3 Boron Nitride

Introduction

Boron Nitride (BN) is a group III-V compound and is isoelectronic to Carbon (C). By the virtue of same electron count, BN can exhibit similar crystalline forms to C. hexagonal-BN (h-BN) is analogous to graphite in structure with layered structure and hexagonal packing within a layer. Cubic-BN (c-BN) is analogous to diamond form of C. BN is not naturally occurring material and is first synthesized by Balmain[112] in 1842 but

the group III nitride was fairly unexplored until recently. Recent interest in the material lead to developments in bulk and nano scale understanding and stable processing of the materials[113]. More importantly, nanomaterials of the BN were synthesized only recently, boron nitride nano tubes (BNNTs) in 1995[114] and hexagonal-boron nitride nanosheets (h-BNNS) in 2005[115]. BNNTS and h-BNNS are different crystalline forms of the h-BN which are analogous to carbon nanotubes (CNTs) and graphene respectively. Figure 5 shows the different h-BN nanomaterials.

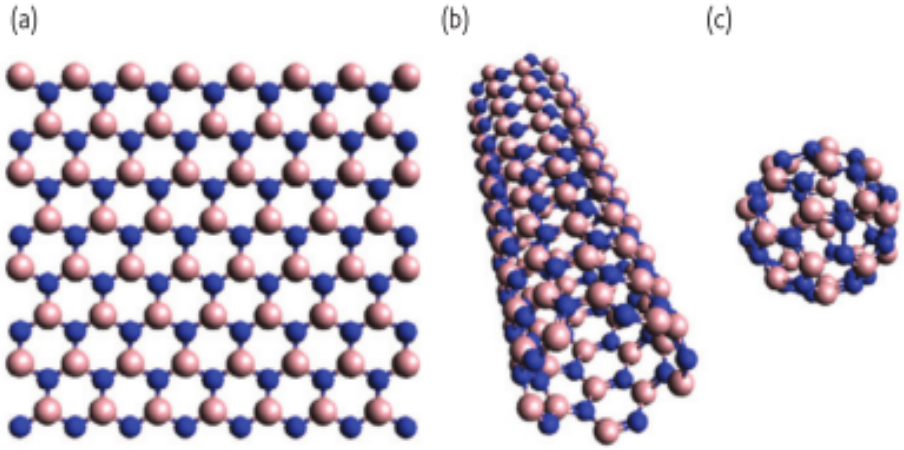

Figure 5 Structural models of BN nanomaterials. (a) 2D - BNNS (b) 1D - BNNT (c) 0D - fullerene[116]

Synthesis

For the last decade, several research efforts have studied different synthesis routes for BNNTs and BNNS. BNNTs are in general produced by arc discharge[114], laser ablation[117], carbothermal methods[118] and chemical vapor deposition[119]. Similarly, BNNS

can be prepared in various methods which are inspired from graphene synthesis and are discussed below.

Micro-mechanical Cleavage

In mechanical cleavage, layers of h-BN are peeled off from the bulk using an adhesive tape. The layers are easily peeled because, the boding between sp^2 in-plane BN atoms is much stronger than the weak van der Walls attractions between layers of h-BN and keeps the sheet in place. This method was employed by Zettl's group and produced h-BN atomic layers in the range of 3.5 nm to 80 nm thickness[120]. The above results are shown in Figure 6. Also, shear forces can be used to cleave the bulk h-BN to obtain h-BNNS which is studied by Li et al[121]. in a ball milling experiment. They were able to produce 3-10 layers of h-BNNS. The resulting h-BNNS are shown in Figure 7. Despite being fast, cheap and easy method, this method does not have precise control on the number of layers of BNNS.

Self- Assembly

The earliest h-BNNS were prepared by self-assembly process. Atomically clean Rh (111) was exposed to borozine vapor at 800^0C at an ultra high vacuum and then consecutively cooled to room temperature. This method witness assembly of ordered mesh oh the metal surface. The structure was probed by Scanning Tunneling Microscopy (STM) and the observation is that the lattice mismatch between BN and Rh drove the hole formation[122]. Similar observations are made on Ni[123] and W[124] surfaces in earlier studies.

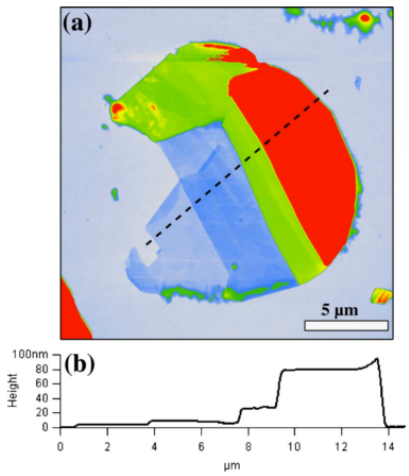

Figure 6 (a) AFM image of a obtained h-BN flake. (b) Height profile along the dashed line.[120]

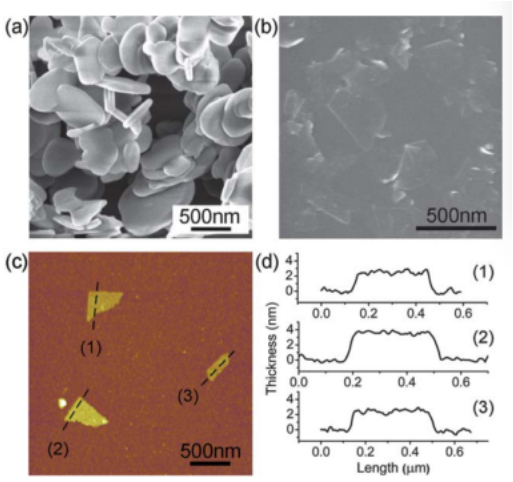

Figure 7 (a) SEM of the bulk h-BN. (b) SEM of the exfoliated h-BNNS. (c) AFM image of three h-BNNS. (d) Height profiles of the sheets in AFM.[121]

Figure 8 shows the STM micrographs of the produced h-BNNS on Rh(111) at several different parameters and serve as the proof to the above discussed mechanism. This process has been very efficient to obtain and control the monolyaer nad bilayer growth but

this is a very elaborate process. Also, peeling off the h-BNNS from the metal surface without damaging is a challenge.

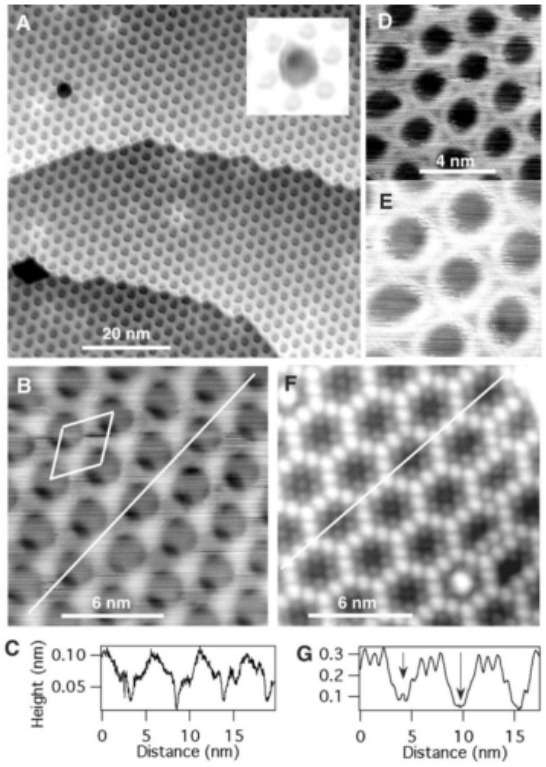

Figure 8 (a) Atomic steps of BNNS on Rh(111). (b) High resolution image showing two layers of BNNS. (c) height profile of the line in B. (d)-(f) several images with different STM parameters. (g) Height profile of the line in image F.[122]

Chemical exfoliation method

BNNS can also be prepared by sonicating the bulk BN sheets in organic solvents. This approach was used by Han et al.[125] in 2008 where they exfoliated mono and few layer h-BNNS as observed under HR-TEM. It is understood that the optimizing the solvent

surface energy very close to the surface energy of the BNNS will give maximum yield of the h-BNNS and on this line, several studies were done to find the best solvent for BNNS[126]. Also, other important work in this aspect is the bulk preparation of h-BNNS possible using this method. Zhi et al.[127] were able to prepare milligrams of the 2-10 nm thick BNNS.

Chemical vapor deposition (CVD)

Currently, the most common lab scale method to prepare pure and controlled h-BNNS is CVD. This is a well established process now du to many efforts from the previous research. In the early process, mixed powders of B_2O_3 and melamine were placed in an induction furnace and treated at 1000^{o}C to 1300^{o}C under nitrogen flow for one hour. Depending up on the temperature h-BNNS layers of 25-50 nm thickness were obtained.[128] Later, under ammonia borane flow, modified CVD process gave 2-5 atomic layer sheets on a Cu-foil.[129] Further improvements to CVD are understood when Shi et al. developed an ambient pressure CVD process on a Ni substrate that can create 5-50 nm thickness sheets.[130] The most important development for in this filed is the monolayer h-BN growth on Cu foils by using NH_3–BH_3 using low-pressure CVD with two heating zones.[131]

Most of the h-BNNS are now obtained either by CVD growth or by exfoliation in bulk. Some other techniques employed to synthesize the h-BNNS are high energy electron irradiation, unzipping of BNNTs and solid state reactions followed by exfoliation or cleaving.

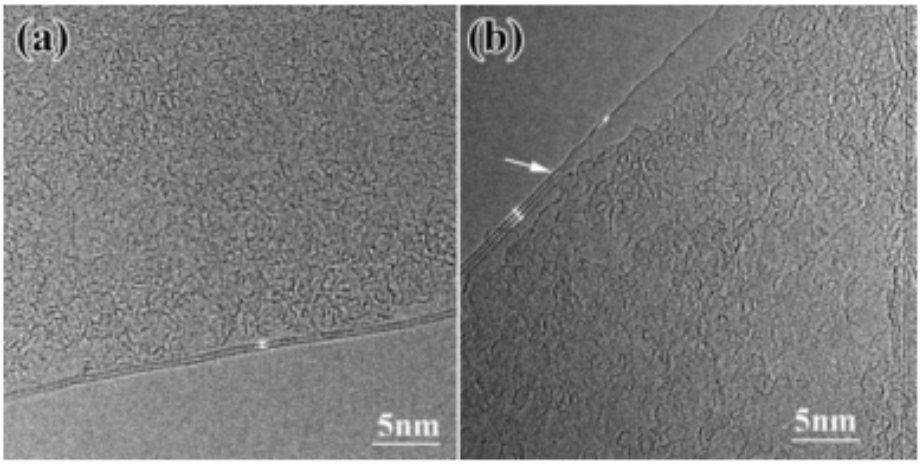

Figure 9 (a) TEM image of the h-BNNS of 2 layers. (b) h-BNNS with three and single layers[125] produced in a chemical exfoliation method.

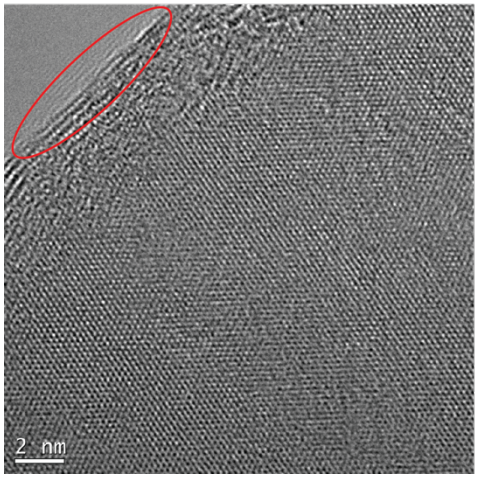

Figure 10 HR-TEM micrograph showing 3-layer h-BNNS produced in our lab in NMP solution[231]

Structure

h-BNNS are very similar to graphene in structure and its bulk counter part is similar to graphite in structure. The atoms in-plane form a hexagonal structure and are

alternating B and N atoms but are attracted via weak van der Walls interactions with other planes. The B and N are stacked on top of each other in adjacent layers giving a AA' stacking. The main role of the van der Waals forces is to anchor the BN layers at a fixed distance, whereas the electrostatic forces dictate the optimal stacking mode and the interlayer sliding corrugation.[132] Table 1 summarizes the crystal constants.[133]

Table 1 Crystal parameters for graphite and h-BN[133]

Material	Crystal structure	Nearest neighbor distance (nm)	Lattice parameters (nm)	Inter layer spacing (nm)
h-BN	Hexagonal	0.144	a: 0.250 c: 0.666	0.333
Graphite	Hexagonal	0.142	a: 0.246 c: 0.670	0.335

Structural studies using TEM, HR-TEM and STEM have revealed that inter layer distance, distance between adjacent atoms within a layer can be measured and these are 0.33-0.34 nm and 0.25 nm respectively in BN (100) atomic plane. In general, fringes at the edges and curls of the sheets allow us to count the number of layers and inter layer distance in the TEM micrographs and HR-TEM can image B and N atoms which leads to measure inter atomic distance.

Properties

The most important properties of BNNS required in this work are the thermal properties. BNNS exhibit a extremely high in-plane thermal conductivity (300-2000 W/(m.K)) in addition to low coefficient of thermal expansion, and superior thermal and chemical stability.[108–111]. h-BNNS are very anisotropic and show only to 40 W/m/K in out-of plane direction which is also the bulk thermal conductivity of the h-BNNS. Single sheet thermal conductivities are very high in-plane due to their low resistance to phonon propagation since no boundary scattering is present. As more layers are added, boundary phonon scattering becomes prominent in addition to increased phonon-phonon scattering and even at nanoscale by 10 layers h-BNNS show bulk properties.

Functionalization

As the central idea of this project lies with incorporating BNNS in to incompatible metallic matrix via organic linkers, it is only logical that the attachment of organic linkers to BNNS must be first strategized. BNNS have a strongly interconnected matrix which is bonded together by partly covalent and partly ionic bond between B and N atoms. It is very stable to oxidation up to 800 ^{O}C and unreactive. But, the reactivity of BN depends on the type of reaction. Possessing good amount of ionic characters, BNNS are readily soluble in several solvents but the covalent chemistry of BNNS is complicated and various strategies have to be employed to achieve this. We are interested in covalent functionalization as we want to tailor functional ligands such that, the other end of the ligand can adhere to metal. This kind of functionalization can be difficult with ionic reactions.

A lot of theoretical studies are done regarding the modification of BNNS. But, unfortunately very little work is experimentally realized. As we want to experimentally modify BNNS for a product, we look at some previous modifications of BNNS. Zhi et al.[127] reported a high level of solubility of BNNS in DMF, an aprotic solvent. Further studies revealed that the solubility is because of Lewis-acid base reaction between B of BN and O of DMF. Further work is done on this concept on how to optimize and maximize the solubility by using different polar organic solvents[109] or even a solvent mixture.[134] We can say that Lewis acid base reaction of BNNS is well established. More non covalent chemistry is observed by Smith et al[135] when they dispersed BNNS by using sodium cholate as surfactant. Similar chemistry has been reported with several other polymers in following works[125,136]. Lewis acid base reactions are found more prominently in the work of Lin et al[137] and all other works[138–143]. Typically, the best possibility of the reaction to happen is the defect sites, where B or N is defective and ready to react.

It is more important to understand the covalent chemistry of BNNS because; covalent chemistries open more possibilities than ionic chemistry. Sainsbury et al[144] showed the direct reaction of nitrene radicals and oxygen radicals[145] with BNNS. As we know the strength of direct nitrene and oxygen radicals, this work gives us an understanding of how difficult covalent chemistry of BNNS is. BNNS require very reactive species to react covalently. Similar to non-covalent chemistry, covalent chemistry will definitely benefit from defects on BNNS. Defective nitrogen can act as a nucleophile and so does a defective B can act as an electrophile. As BNNS have partly ionic characters, defective nitrogen is actually a very strong nucleophile as it will carry more negative

charge than normal lone pair of nitrogen. Nazarov et al[146] reported exfoliated BNNS with 6-7 wt% of oxygen by treating BNNS with H_2O_2, HNO_3/H_2SO4 mixture and oleum at 100-150 ^{O}C. Ikuno et al[138] reported the functionalization of BNNS with amine groups by plasma irradiation. These amino functional groups are further used to react with 3-bromopropanoyl chloride (BPC) and formation of amide is reported. Zhi et al[147] reported a similar reaction of formation of amide from benzoyl chloride and amine on BNNS. Once amine groups are introduced on to BNNS, a lot of amine functional group reactions can be carried out. Similar is the case with oxygen functionalization and nitrene addition. Wu et al[142] reported adsorption way to introduce amine groups on to BNNS which is eventually understood to be chemical adsorption in nature. Cui et al[148] reported formation of GO analog of BN by heating BNNS up to 1200 ^{O}C in oxygen environment. Han et al[149] decorated BNNS with stannic oxide with covalent reaction and adsorption. Similar reactions were reported in these works[150–152] where BNNS were decorated with Ag and Au.

Though it is not easy to modify the BNNS chemically, it is not impossible and can be done either ionically or covalently if harsh enough conditions were provided. We followed certain previously reported functionalizations and also created a new functionalization in the process of preparing TIMs.

In summary, boron nitride can form several crystalline nanomaterials like BNNTs and BNNS and reliable synthesis methods are well studied now to produce these nano-materials. A large scale industrially viable process is still a question but not very far away with large scale exfoliations and CVD methods yielding in milligram to gram quantities.

These nanomaterials show interesting properties in terms of electrical, thermal, mechanical, optical and morphological which are also tunable by introducing defects or by substituting with other atoms. Especially, functionalization with bi-functional ligands can help to chemically integrate these BNNS into other matrices and is the important concept in preparation of metallic TIMs based on copper or silver.

2.4 Electrodeposition

Electro deposition the technique of depositing metals on to a substrate by using electric field in a cell filled by electrolyte. When an external electric field is applied on to electrodes they turn into cathode and anode by assuming negative and positive charge respectively. In electrodeposition, typically anode is a sacrificial electrode as it dissolves in to the solution and typically deposits on to the cathode. During this electro deposition, several parameters like electrolyte concentrations, applied external electric field, temperate of the bath can be varied to get the required quality of the deposit. To understand more basics, certain concepts are presented below.

Electrode potential

When a metal is immersed in to aqueous solution, it immediately acquires a potential due to the electric interphase created by the interchange of metal ions between the crystal and the solution. The interchange of the ions soon reaches an equilibrium and the potential becomes constant called equilibrium potential (E). The aforementioned potential difference is measured with respect to standard hydrogen electrode (SHE). This potential can be calculated by Nernst equation which is given the equation 1.

$$E = E^0 + 2.303\ {}^{RT}/_{zF} \ln\ a(M^{z+}) \quad (5)$$

where T is the temperature, z is the metals oxidation state, F is the faraday constant and a is the activity of the metal ions in the solution. In the case of mixed ion solutions, the activity is calculated by the stability constant of the complex.

In an electrochemical cell, external electric field is applied on to electrodes and for this the reason the electrode assumes a different electrode potential than the equilibrium electrode potential and this difference is called overpotential (η). This overpotential decides the current that flows through the electrochemical cell and overpotential can be positive (anode) or negative (cathode). The relation for the overpotential and the current (i) flowing through the cell can be given by the equation 6

$$\eta = a + b\ log|i| \quad (6)$$

where a and b are constants given by the following equations for a cathode

$$a = {}^{2.303RT}/_{\alpha zF} \log i_0 \quad (7)$$

$$b = {}^{2.303RT}/_{\alpha zF} \quad (8)$$

where i_0 is the current when overpotential is zero, i.e., when no external electric filed is applied and α is the transfer coefficient.

These equations are valid only in the regime of kinetic control of the charge transfer, that is the current (charge flow) is slower than the diffusion of the metal ions in the solution. Current can never be more than the diffusion/transport of the ions in the solution to the electrode since they are the charge carriers and hence a limiting current is dictated by the mass transport of the ions in the solution. This limiting current is given by

the equation x. The quality of the deposit depends on the relative value of the current forced through the cell to the limiting current.

$$i_L = (^{nFD}/_{\delta})c_b \quad (9)$$

where n is the number of electrons involved in the reaction, D is the diffusion coefficient of the ions, δ is the thickness of the Nernst diffusion layer and c_b is the bulk concentration of the metal ions in the solution. A typical quality of the deposit is given in later chapters.

The quantity (weight) of the deposit can be calculated by the equation x given below where Z is the electrochemical equivalent, i is the current flowing through the system and t is the time elapsed.

$$w = Zit \quad (10)$$

The w can be used to calculate the thickness of the deposit which is more more importance by calculating the area of the deposit and known density of the deposit material assuming no air gaps are created in the matrix while depositing.

Now, as the deposit grows in to a film, several theories are put forward regarding how ions are transferred on to the deposit and how the film grows. There are mainly two mechanisms for the ion transfer on the films and are called step-edge ion-transfer mechanism and terrace-ion transfer mechanism. Also, the growth of the film is believed to happen in either of the two mechanism called layer growth mechanism and 3D crystallite growth mechanism. The details of these above mentioned mechanism is beyond the scope of this work and many details can be found else where. However, both growth

mechanism eventually gives polycrystalline films, where each crystal can be called as a grain and the separation between two grains is called a grain boundary. The size of the grains highly depends on the overpotential and constituents of he electrolyte bath.

Pulse electrodeposition is an important technique in the electrodeposition in which overpotential is not a direct current DC but a pulse or wave. This technique is used to control the quality of the deposit by dynamically modifying the Nernst diffusion layer at the electrode-solution interphase and forcing different amount of ions in to this region. In pulse deposition, a suitable waveform is created as the overpotential and this waveform typically consists of on and off times. The on time is when the potential difference is applied and off time is when the current forced through the cell is zero or negative which will allow the recently deposited atoms to move in to the most stable position before other atoms are deposited on to it. The waveform can be rectangular or sinusoidal or any other form which will best suit the deposition.

Electrodeposition can be employed not only to deposit pure metals but also to create alloys or multilayers or composite materials by specific engineering. For alloy depositions, the electrolyte solution has to be carefully engineered for the concentrations of the involved ionic such that the they should have same or very comparable overpotential. Also, according the depletion rates of the ionic species, they have to be replenished to have same concentration through out the film thickness. More importantly, it can be summarized that electrodeposition can be innovatively used to obtain new type of materials or composites. We exploited this principle of electrodeposition by infusing functionalized BNNS in to the copper and silver electrolyte solutions and electro-co-

depositing these nanoparticles with metal ions into the metal matrices to form homogenous composites.

2.5 Graphene

Graphite is a carbon form with hexagonal honeycomb like unit cell and stacked up layers weakly adhered to one another by van-der Walls interactions. It was understood that the reduction of number of layers in graphite gave rise to interesting properties and many studies were underway in this field, isolation of single layer graphite; graphene by Geim and co-workers[153] at Manchester University in 2004 changed nanotechnology forever. The stable isolation of graphene spiked the interest and since then a lot of development took place in the synthesis of graphene and other 2D nano-materials which also led to increasing application of graphene in several fields like electronics, composites, bio-medical applications.[94,154]

Graphene is a 2D material which is made up for sp^2 hybridized carbons arranged in a hexagonal fashion. Graphene is initially extracted in micro-mechanical cleavage fashion but soon liquid exfoliation and CVD techniques [similar to BNNS discussed above] evolved in hope to control the quality of the graphene produced but were unable to scale up easily due to cost issues.[154,155] The new advancement of producing graphene via Graphene Oxide method looks promising to scale up at low cost. In GO method, graphite is first modified in to graphite-oxide and then the material can be easily exfoliated in water at low mechanical energy due to improved interaction of oxide groups with water rather than just carbon groups. Once, the single layer GO sheets are obtained, they are reduced to form graphene sheets.[156–158] Though there are certain challenges in reducing

the single layer GO without reassembling them again or breaking them, few studies claim to overcome them by using a higher pH water or using hydrazine as solvent for the overall process.[159,160]

In this project, graphene is used to make nanocomposites with polystannate with the aim to improve the thermal conductivity of the polymer and also improve the stability of the polystannate in ambient conditions by making use of thermal and optical properties of the graphene respectively. Firstly, graphene is 97.7% transparent in the visible range but soon turns in to opaque as the layers stack up. When few layer graphene is considered, it absorbs most of the visible range wavelength and easily makes a light blocking element[161,162]. Most importantly, graphene is highly thermally conductive, not due to presence of free moving electrons but due to very low phonon-phonon scattering and highly reduced phonon-boundary scattering. In theory, it is calculated that graphene can have thermal conductivities up to 6000 W/m/K but experimentally graphene layers showing thermal conductivities ranging from 5000 – 2400 W/m/K were produced reliably and this value is dependent on the size of the layers[4,155,163,164]. The thermal conductivity of graphene saturates in the range of 4 - 7 layers and reaches a graphitic value of 2000 W/m/K at 7 layers which is still very high compared to any metal at room temperature[94]. Like BN, graphene is also much less thermally conductive in the out-of plane direction for the same reasons of the high boundary scattering faced by phonons and in fact for graphite, this conductivity is as low as 6 W/m/K.[165,166]

2.6 Polystannate

Organo-metallic polymers such as polystannanes with tin as the backbone repeating unit, (-SnR2-)n, has gathered a lot of attention recently. The first report of these materials dates back to 1852 by Lowig[167]. Polystannanes can be synthesized via the Wurtz reaction[168,169] in which dichlorortin compounds are reduced using sodium metal, electropolymerization[170] in which dihalotin compounds are directly reduced in a electrochemical cell to form the polymers, and catalytic dehydro-polymerization[171] of hydridies of tin. All the above synthesis reported resulted in low yields or had detectable levels of oligomers or other by-products. Comprehensive techniques were recently developed for higher yields and lower contaminants[172,173]. These recent advancements in the synthesis of polystannanes furthered the exploration of these materials for a wider scope of applications. The polymeric structure of these materials make them mechanically compliant and the metal centers along the backbone form a chain of sigma bonds that facilitate the electronic transport. These polymers are soft while being thermally conductive which make them ideal candidates for applications towards heat management, advanced functional materials, bendable electrodes, coatings for electronic applications, etc.. The recently improved electrochemical polymerization has acceptable yields in the range of 30-70% depending on the monomer and promises to be scalable in higher through-put synthesis[170,174,175]. However, polystannanes have proven to be sensitive to light[168,176–179] and moisture[170] making it difficult to process and handle in ambient condition.

In the electro polymerization reaction, monomers like dibutyldichlorotin are dissolved in a suitable solvent like DME which can dissolve the monomer and can act as a medium for electron transfer. During the reaction, electrons running through the solvent are utilized by the monomer to form a polymer.

The polymer synthesized in this work made use of dichloro dibutyl tin as monomer and it easily decomposed in to oligomers with exposure to ambient conditions for less than an hour. Nanocomposite of the produced polymer and graphene nanoparticles were made to improve the thermal conductivities from 3-5 W/m/K to up to 40 W/m/K and also improve the stability in ambient conditions from less than hour to 24 hours.

3. COPPER BASED METAL- ORGANIC- INORGANIC NANOCOMPOSITES*

This chapter gives the details of the synthesis of metallic-organic-inorganic nanocomposites in which copper is the metal matrix and the fillers are boron nitride nanosheets that are modified with thiosemicarbazide (TSC).

3.1 Materials and Methods

3.1.1 Materials

Hexagonal Boron Nitride, h-BN (98%, APS: 0.5 micron), produced by the reaction of boric acid and ammonia at 900 ^{O}C ($B(OH)_3 + NH_3 \rightarrow BN + 3H_2O$) was received from Lower Friction-M.K. IMPEX Corp, (Mississauga, Ontario, Canada). Sulphuric Acid (H_2SO_4, ACS reagent, 95.0-98.0%), Copper (II) Chloride ($CuCl_2$, 99%) and Copper Sulfate pentahydrate ($CuSO_4.5H_2O$, ≥98%) were obtained from Sigma Aldrich (St. Louis, MI). Thiosemicarbazide (CH_5N_3S, >98%) and 1,3,4-Thiadiazole-2,5-dithiol ($C_2H_2N_2S_3$, >95%) were obtained from TCI America (Portland, OR). N-methlyl-2-pyrrolidone (C5H9NO, 99%) (NMP) was obtained from VWR (Radnor, PA). Copper sheets were obtained from McMaster Carr (Elmhurst, IL) and aluminum substrate was obtained from Metals Depot (Winchester, KY). Silicon wafers (Silicon <100> P/Boron, >5000 ohm-cm, double side polish, <10 Angstrom Ra) were received from University Wafer (Boston, MA).

*Reprinted with permission from "Metal–Organic–Inorganic Nanocomposite Thermal Interface Materials with Ultralow Thermal Resistances" by Yegin Cengiz et al., 2017. *ACS Applied Materials and Interfaces*, 9, 10120-10127, Copyright 2017 by American chemical society

3.1.2 Preparation and characterization of BNNS and f-BNNS

Preparation of BNNS

The h-BN powder (98%, APS: 500μm) dispersed in N-Methyl-2-Pyrrolidone (NMP) was exfoliated by ultrasonic dispersion using a SYCLON ultrasonic cell crusher (Syclon Electr. Instr. Comp., Zhejiang, China). A suitable polar solvent having a similar surface energy to that of h-BN can be efficiently used for exfoliation. For this purpose, NMP (surface energy: 40.5 mJ/m^2 at RT) was selected as the solvent for exfoliation of h-BN (surface energy: 65 mJ/m^2).

Characterization of BNNS

The dispersion containing the nanosheets was diluted and dropped onto a silicon wafer, and dried at 75 ^{O}C for 24 hours for Atomic force microscope analysis. Height sensor images were obtained via a Bruker Dimension Icon AFM (Bruker, Santa Barbara, CA) at 0.5 Hz scan rate 512 samples/line. Several images were obtained to statistically determine the size and height distribution of BNNS via Nanoscope Analysis Software. Particle size distribution of the BNNS was also confirmed using dynamic light scattering (DLS) (Zetasizer Nano ZS90, Malvern Instr.Inc., Westborough, MA).

High resolution transmission electron microscopy (HR-TEM) was performed in a JEOL ARM200F with electron probe aberration (Cs) corrector operated at 200 kV, also equipped with an Oxford Instruments X-MaxN 100TLE 100 mm^2 detector for energy dispersive X-ray (EDX) spectroscopy and a Gatan Enfina spectrometer for electron energy loss spectroscopy (EELS). High angle annular dark field (HAADF) and annular bright

field (ABF) Scanning transmission electron microscopy (STEM) imaging techniques were used to characterize the nanostructure morphology of the BNNS samples.

Synthesis of f-BNNS

Covalent functionalization of BNNS was achieved by reacting exfoliated BNNS with thiosemicarbazide (>98%) in NMP (1:10:100 in weight). The reaction took place at 170 ^{O}C for 30 hours under nitrogen flow. The obtained product was dialyzed in NMP for 10 hours to remove the unreacted ligands, followed by centrifugation at 3500 rpm for 15 minutes. Next, the supernatant was removed, the precipitate (f-BNNS) was dried at 75 ^{O}C in a vacuum furnace for further removal of the remaining NMP from f-BNNS powder. Thus obtained f-BNNS are further washed in acetone and dried at 50 ^{O}C overnight.

Characterization of f-BNNS

Nuclear magnetic resonance (NMR) spectra in solid state were obtained on AVANCE-400 instrument. ^{11}B shifts are reported relative to $BF_3(OEt_2)$. High-power proton decoupling was applied with a 90° pulse time of 5 μs, a contact time of 5 ms, and a recycle delay of 8 s. Approximately 50 mg of the sample was packed into 5 mm Wilmad thin wall precision NMR sample tube 8" and loaded in to 7 mm CP-MAS rotors. The rotor spinning speeds were 4 kHz. All NMR measurements were carried out at 25 °C.

HR-TEM analysis was carried out on the same instrument mentioned above and in same fashion.

Synthesized f-BNNS was mounted on to a copper tape and placed on an Omicron XPS (Scienta Omicron GmbH, Taunusstein, Germany) for X-ray photoelectron spectroscopy. High resolution XPS spectra were carried out for N, S, C, and O atoms. In

addition, pure BNNS and pure thiosemicarbazide were also analyzed to confirm the functionalization. For further confirmation, Infrared and Raman spectroscopies were obtained via a Shimadzu IR Prestige ATR-FTIR (Shimadzu Scientific Instruments Inc., Columbia, MD) and a high spectral resolution analytical Raman microscope (LabRAM HR Evolution, HORIBA, Ltd., Edison, NJ), respectively by placing a small sample of dry f-BNNS powder under lens.

3.1.3 Fabrication of Thin Film Nanocomposite TIMs

Thin film nanocomposite TIMs were grown on aluminum sheets and silicon wafers. The aqueous electrolyte solutions were prepared by varying concentrations of $CuSO_4.5H_2O$, 1.8 M H_2SO_4, a trace amount of $CuCl_2$, and various concentrations of f-BNNS (0 wt% to 2.5 wt%). Each solution was sonicated for 10 minutes in a bath sonicator for homogenous dispersion of f-BNNS, and transferred to an electroplating cell. A pure copper sheet (>99%) and a substrate were connected to anode and cathode, respectively. The electrical power source was a Nuvant Powerstat05 Potentiostat (Nuvant Systems Inc., Crown Point, IN). The electrodeposition was carried out at a current density of 0 to 12 A/dm2 and AC frequency of 950 Hz with 30% off time. The main advantage of the pulse electrodeposition is the ability to change experimental parameters such as pulse peak current density and on-/off-time in pulse electrodeposition to obtain the film of required quality.

3.1.4 Characterization and Performance Evaluation of TIMs

Chemical Characterization of TIMs

f-BNNS content in the nanocomposite thin films was obtained by chemical-elemental analysis. The nanocomposite TIMs were cut into smaller pieces and immersed in an H_2SO_4/HNO_3 acid solution (3:1 in volume fraction) at 40 ^{O}C. The solution dissolved the copper content and settled down the f-BNNS. The precipitate was drained out, dried, and weighed. Then, it was put in the acid solution again to remove any possible residual copper. This step was repeated several times until no change in the weight of the f-BNNS was observed. Several samples for each experimental condition were prepared and measured for statistical reliability.

The Secondary ion mass spectrometer (SIMS) CAMECA 4F (Ametek Inc., France) has also been used to confirm the mass fraction of thin film nanocomposite samples. The analyzed surfaces were sputtered by the 5.5 keV O^{2+} beam with a current of 15 nA. The diameter of the beam was ~3 μm; the raster was 250x250 μm^2 for all samples. The measured secondary ions were positively charged.

Mechanical Characterization

Hardness and reduced elastic modulus values were measured via a Hysitron TI 950 Triboindenter (Hysitron Inc., Minneapolis, MN). A Berkovich tip with a well-defined geometry was used for indentation and forty measurements were taken from each sample for statistical analysis. For each measurement, a force of 5000 mN was applied over 10 seconds, and the tip was withdrawn from the surface for 10 seconds with a 5-second

holding time in between. The force versus depth curves were fitted to give the values of reduced modulus and hardness.

Elastic modulus and Poisson`s ratio of the samples were measured by tensile testing via an INSTRON 5944 universal testing instrument (INSTRON, Norwood, MA). For this purpose, the thin film nanocomposite samples were machined as dog-bone-shaped tensile test specimens, which were produced in accordance with a scaled-down ASTM D882 standard. A 40X zoom camera was used to measure the change in cross section at the necking region to calculate the Poisson's ratio.

Also, the reduced modulus values obtained from Nanoindentation tests can be converted to Young`s modulus via the Poisson`s ratio. Tensile test specimens were applied a pre-determined tensile strain in the elastic region, the corresponding lateral strain was calculated by using a micrometer, and the Poisson`s ratio was calculated by the following equation;

$$v = -\frac{d\varepsilon_y}{d\varepsilon_x} \tag{11}$$

The Poisson`s ratio of the nanocomposite samples was measured to be 0.337± 0.05, which is not significantly different from that of pure copper (0.34). Then, the Young's modulus (Es) of the samples were calculated via equation 12,

$$\frac{1}{E_r} = \frac{(1-v_i^2)}{E_i} + \frac{(1-v_s^2)}{E_s} \tag{12}$$

where subscript i denote indenter properties and Er is the reduced modulus.

Thermal Characterization

A Modulated Q20 DSC (TA Instruments, New Castle, DE) was used to measure specific heat capacity of the samples. For this purpose, TIMs were cut in to samples of 7-12 mg and loaded in TZero DSC cells and loaded on to the instrument. A modulation of 1 ^{O}C for every 120 seconds is applied for a 15-minute isothermal conditions at temperatures of 30 ^{O}C, 50 ^{O}C, 75 ^{O}C and 100 ^{O}C.

Thermal diffusivity measurements were performed via a DLF-1200 laser flash diffusivity system (TA Instruments, New Castle, DE). Samples were cut in to 1 inch circles and loaded in to the furnace to take diffusivity measurements at 30 ^{O}C, 50 ^{O}C, 75 ^{O}C and 100 ^{O}C.

The density of samples was determined gravimetrically using Archimedes principle. “Any object, wholly or partially immersed in a fluid, is buoyed up by a force equal to the weight of the fluid displaced by the object”. This means volume of fluid displaced by an immersed body is equal to the volume of the body. A hollow cylinder with volume markings of 0.01ml is taken and observed under zoom-in camera. A pre-determined weight of material is cut in to pieces and put in to the cylinder and the raise in the volume of water in the cylinder is observed from the 30X zoom-in camera. The measured volume and weight of the material is used to calculate the density.

Thermal conductivity of free-standing samples was calculated using the measured thermal diffusivity (α), specific heat capacity (cp), and density (ρ) values as follows:

$$\alpha = K.\rho^{-1}.c_p^{-1} \tag{13}$$

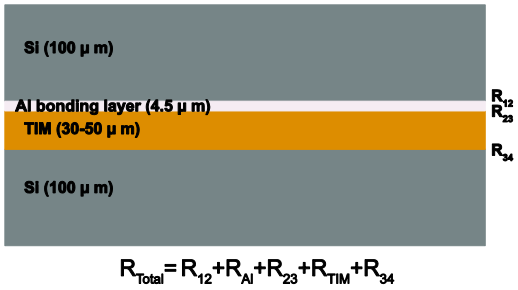

Figure 11 Sandwich configuration for the thermal resistance measurements used in the PSTTR technique.

Further, phase sensitive thermal transient reflectance (PSTTR) measurements were done at NREL, Colorado to determine thermal resistance of the samples. In general, thermal resistance of the TIMs are measured under pressure loading which do not need any bonding between surfaces but as we are interested in creating an adhesive loading which is more relevant in low pressure loadings and bonding electronic devices we created an Al bonding layer to act as a binder which will add minimal resistance to the overall sandwich. The Cu-BNNS nanocomposite was bonded between two the silicon wafers by depositing Cu-BNNS on one silicon wafer of 1-inch diameter and using Al bonding to stick to the other silicon wafer. Pure aluminum of 4.5 μm thickness is melted on top of a silicon wafer under argon atmosphere and transferred it on to the TIM surface to form a sandwich which is cooled at ambient temperature overnight to form the Al bond. The overall sandwich configuration is showed in Figure 11. Further details of this technique are discussed in appendix.

Thermal Cycling Behavior and Coefficient of Thermal Expansion (CTE)

Thermal cycling tests were performed with the DLF-1200 laser flash diffusivity system to test the reliability of the produced TIMs. The samples were subjected to thermal cycling between room temperature (RT) and 100 ^{O}C for twenty cycles.

CTE in the produced samples was measured using a thermal mechanical analyzer-TMA (TA Instruments, Newcastle, DE) with a built-in tensile test setup. Rectangular thin film samples were prepared, mounted between the grips in the TMA analyzer, and heated up to 140 ^{O}C. The result was compared with those obtained from pure copper and pure silicon.

3.2 Results and Discussion

3.2.1 BNNS and functionalization of BNNS

Filler geometry plays an important role in determining the mechanical and thermal properties of a composite materials. The AFM micrograph in Figure 12 shows that the BNNS are dispersed as mono- or few-layered structures. The bright features on the nanosheets are assumed to be NMP residues since it is a relatively non-volatile solvent. The size and thickness of the nanosheets were found to be 444±115 nm and 3.05±0.79 nm, respectively, (Fig. 12b and c) by measuring the dimensions of hundred individual nanosheets. Also, the effect of sonication on the particle size distribution was investigated by DLS measurements. Figure 12d indicates the decrease in the particle size with an exponential trend, which implies that the sonication of the h-BN powder can generate sufficient energy to break some of the covalent bonds between B and N atoms, and introduce defects at the edges.

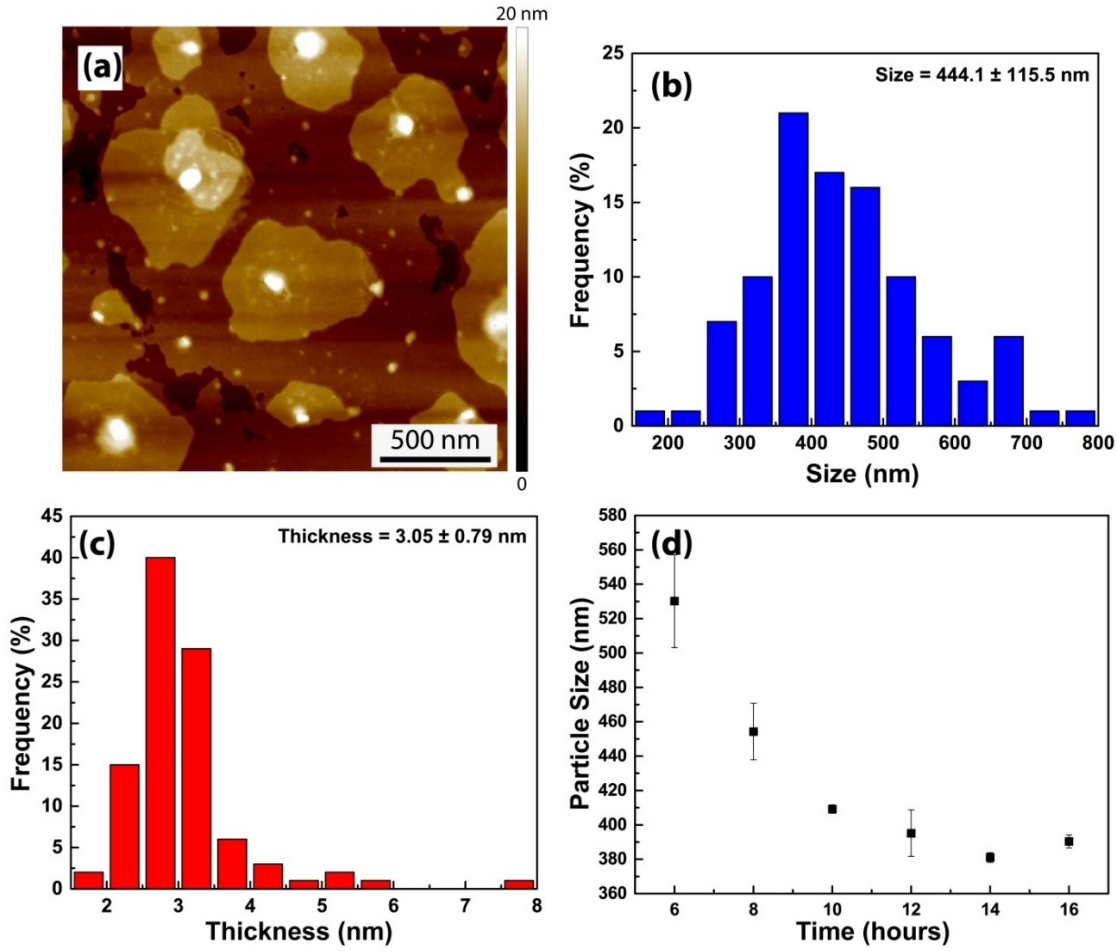

Figure 12 Characterization of BNNS. (a) a height sensor image taken from exfoliated BNNS. (b,c) frequency distribution of nanoparticle size and thickness of the BNNS, respectively, obtained from AFM images. (d) effect of exfoliation time on particle size distribution.

The first step in producing metal/organic/inorganic nanocomposite TIMs was the functionalization of the boron nitride nanosheets with a ligand that is capable of reducing their effective stiffness and covalently linking BNNS with the metal matrix. Towards this end, we relied on thiosemicarbazide (TSC), which contains an amino group that can react

with electron deficient boron groups of BNNS, and a carbonothioyl group (or its tautomer, thiol) that can react with copper.

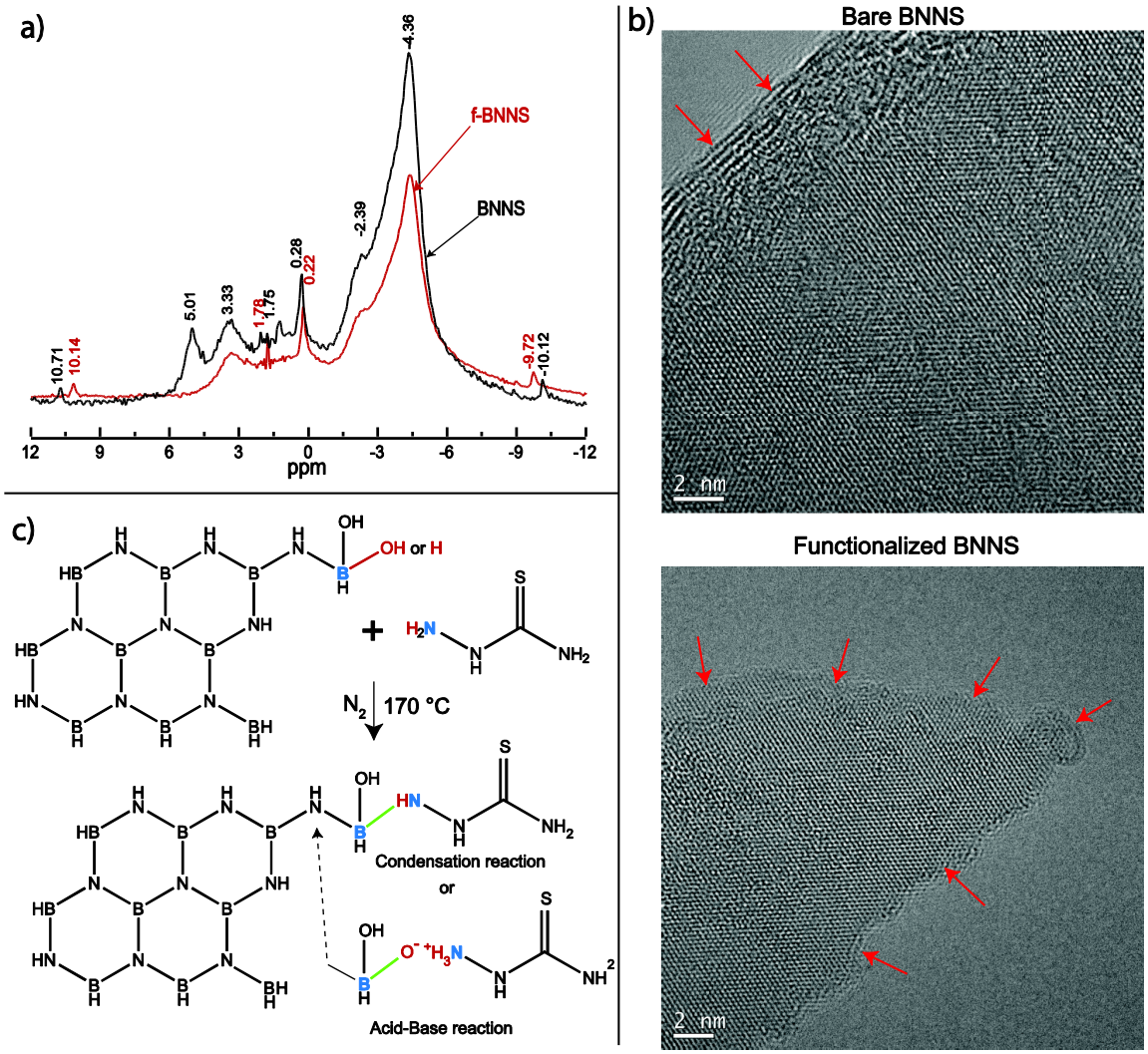

Figure 13 a) ^{1}H MAS NMR spectra of BNNS before and after the functionalization reaction with thiosemicarbazide. b) HR-TEM micrographs of BNNS before and after the functionalization reaction, and c) Proposed reaction schemes.

To gain insights into the reaction of TSC with BNNS, first, solid state ^{1}H MAS (Magic-Angle Spinning) NMR (Nuclear Magnetic Resonance) was used (Figure 13a). There are a total of 8 different H atoms present in BNNS. These correspond to different hydrogens bonded to edge B and N atoms (N_2BH, NBH_2, NBH_3^-, B_2NH, BNH_2, BNH_3^+) and others in $N_2B(OH)$ and $NB(OH)_2$ in no specific order. The major changes are observed as disappearance of peak at $\delta = 5.01$ and shift at $\delta = 10.71$ and -10.12 which correspond to hydrogens attached to edge B(OH), BNH_3^+ and NBH_3^- respectively. The major changes at the peak of $\delta = 5.01$ is hydrogen in the hydroxyl group on an edge B atom. This indicates reaction with TSC as a condensation reaction. This was also supported by ^{11}B MAS NMR spectrum for BNNS and f-BNNS shown in Figure 14. For neat BNNS, there were four major peaks: the largest signals (20.8 ppm and 11.8 ppm) correspond to tricoordinated boron atoms within B−N bonds of planar BN3 groups, the signal at $\delta = -25.7$ ppm indicates the presence of tetragonal boron atoms (i.e. R_4B^-), and the signal at $\delta = 66.8$ ppm suggests the existence of boron atoms with hydroxyl groups. The reaction of BNNS with TSC resulted in shifts only for tetra coordinated boron atoms (from −25.7 ppm to −17.2 ppm) but not for boron from planar BN, indicating that the functionalization reaction takes place from the reactive edges of BNNS.

The comparison of high-resolution TEM micrographs of BNNS before and after the functionalization step revealed that the functionalization occurs at the edges rather than on the basal plane (Figure 13b), which is preferred in 2-D materials to prevent the loss of intriguing properties.

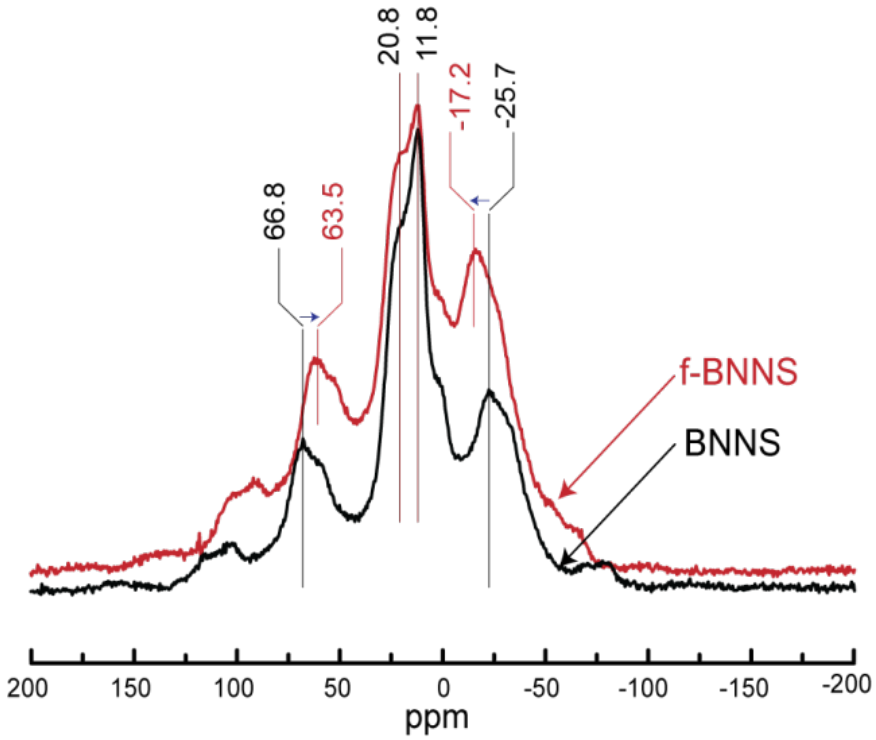

Figure 14 ^{11}B MAS NMR spectra of BNNS and f-BNNS

Further studies with Raman spectroscopy revealed the disappearance and major shifts at wavelengths 806 cm^{-1} (NH_2 wagging and CS stretching), 1008 cm^{-1} (NN stretching and CN stretching), 1172 cm^{-1} (NN stretching), 1526 cm^{-1} (NH bending), 1630 cm^{-1} (NH2 bending), and 3258 cm^{-1} (NH_2 stretching) from the TSC spectra upon the reaction with BNNS (Figure 15). These findings demonstrate that the most notable changes on TSC occur on the amino group.

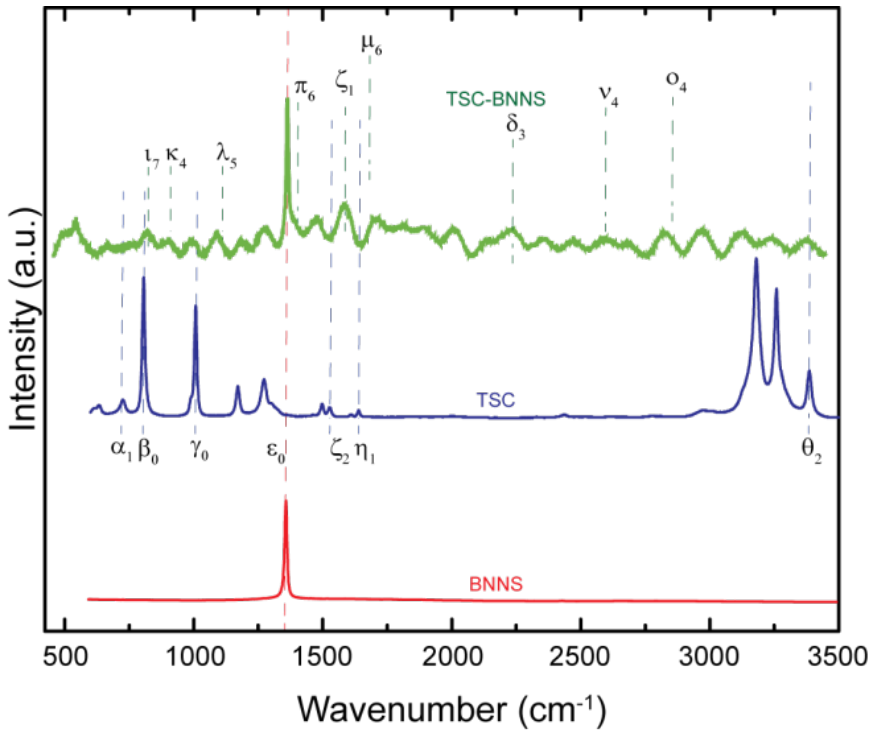

Figure 15 Raman Spectroscopic studies of BNNS, f-BNNS and pure Thiosemicarbazide

All the above observations were also confirmed with FTIR spectra given in Figure 16b. The disappearance of peak at 1614 cm^{-1} and the shift of the peak at 1639 cm^{-1} to 1675 cm^{-1} is attributed to the cleavage of amine groups in thiosemicarbazide and the reaction of the remaining amine group with boron atoms on the BNNS. Similarly, the disappearance of peaks at 3255 cm^{-1} and 3362 cm^{-1} can also support these conclusions. On the other hand, no significant change on the peaks associated with the primary amide was observed, proving that the functionalization reaction indeed takes place between the amino group of TSC and BNNS.

The complementary x-ray photoelectron spectroscopy (XPS) studies shown in Figure 16a gives the information on sulfur oxidation states. It is understood that sulfur bonding state is changed from double bond to single bond. The shift in XPS suggests the presence of S atom in the form of a thiol as shown in the NIST database. To accommodate all these observations, the S atom undergoes tautomer transformation to give thiol form.

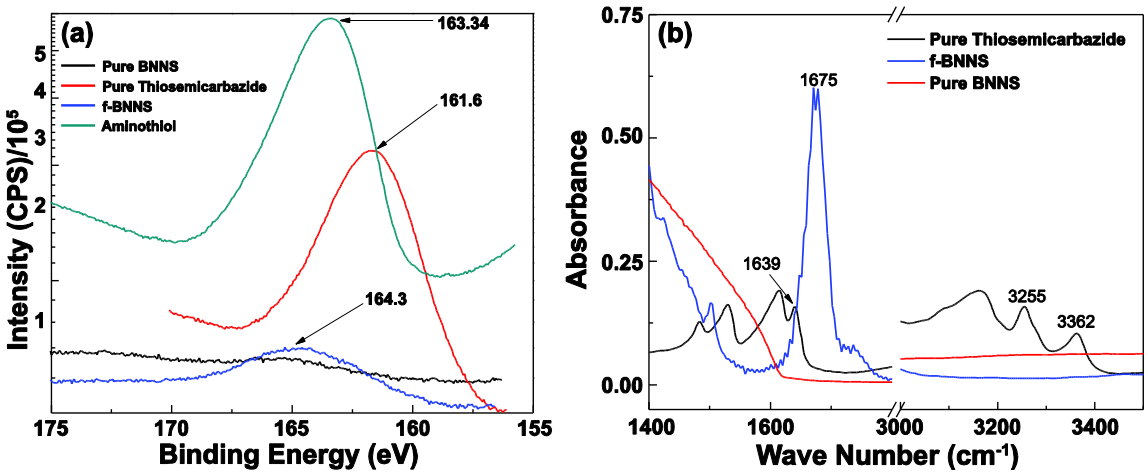

Figure 16 Characterization of functionalization via. (a) XPS and (b) Infrared (IR) Spectroscopy for pure BNNS, pure thiosemicarbazide and f-BNNS. XPS scan for a commercial amino thiol (3-Amino-1,2,4-triazole-5-thiol) was also performed for comparison.

When we put all of these pieces obtained from NMR, TEM, Raman, FTIR and XPS together, the picture emerges that the electron-rich amino group of TSC reacts with hydroxylated and tetra coordinated borons at the edges of BNNS either via condensation or Lewis acid-base reaction (Figure 13c). In this reaction scheme, the carbonothioyl (or its tautomer, thiol) group sticking out of the f-BNNS is available for coordination bonding

with copper. Also, most importantly the functionalization is only at the edges which helps in preserving the intriguing properties of the BNNS.

3.2.2 Metal nanocomposite TIMs

Traditional molten metal-based mixing and agitation approaches for metal/inorganic nanocomposites are not feasible for producing metal/inorganic/organic hybrid nanocomposite TIMs due to the presence of organic linker molecules and the high melting temperature of copper. To overcome this challenge, we developed a programmed electro-co-deposition approach by which the reduction of copper ions and the nucleation and growth of the resultant elemental copper on the cathode occurs, while f-BNNS experience Brownian motion and reaches the cathode through diffusion (Figure 17a).

Once the f-BNNS bearing carbonothioyl/thiol groups on the terminal edges come into the contact with copper crystals, the chemisorption reaction takes place as proved in Figure 17b. The coordination reaction between copper atom and sulfurous groups was confirmed through X-ray photoelectron spectroscopy (XPS) studies as evidenced by a shift in binding energy of some fraction of copper from 932.75 eV to 934.80 eV. The interplay among these three processes determines the nanostructure of the resultant metal/inorganic/organic hybrid nanocomposite. Using this approach, we were able to produce fairly homogenous films (Figure 17c). The fracture SEM studies revealed that the nanocomposite TIMs developed have a peculiar nanostructure in that f−BNNS are localized only at the grain boundaries of copper crystals (Figure 17d). It is also possible to manipulate the properties of the nanostructure by adjusting the composition and pH of electrolyte, current density, and time and these effects will be discussed in detail below.

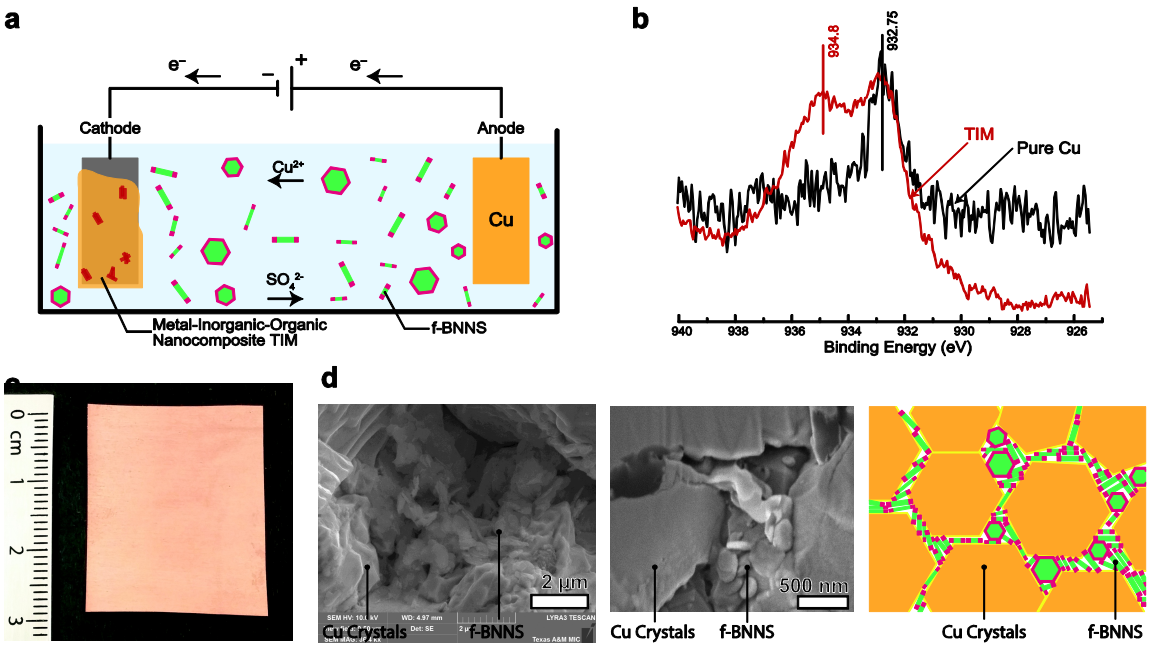

Figure 17 a) Illustration of the chemisorption coupled electrodeposition approach. b) XPS analysis of copper in pure copper and nanocomposite TIM. c) photograph of a typical metal/organic/inorganic nanocomposite TIM, and d) SEM micrographs and schematic illustration showing the distribution of f-BNNS across the copper matrix.

Effect of time

Electroplating experiments to produce copper-based metal-inorganic-organic nanocomposites were performed at various time periods to investigate the effect of time on thickness and morphology of thin film samples (Figure 18). It was observed that for current densities of 5-12 A/dm^2, when the electro deposition time was below 45 minutes, the thin films were unstable and sometimes even there was no film formation. Above 45 minutes, robust films were obtained. The thickness of the samples increased as the electroplating time increased. 50-100 micrometer thick TIMs could be obtained with an electro deposition time of 60 minutes at a current density of 12 A/dm^2.

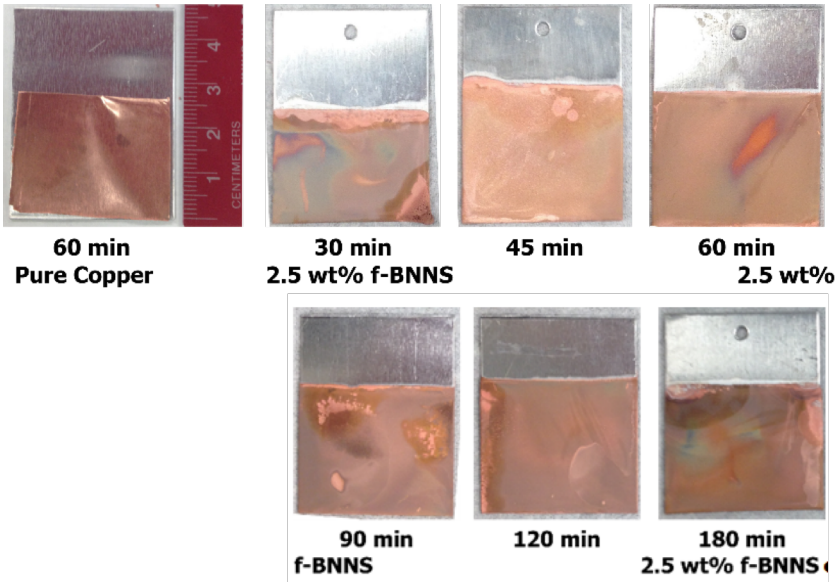

Figure 18 Effect of electroplating time on morphological properties of the developed TIMs

Figure 19 shows the time dependence of thickness of TIMs. Once the electroplating time required to produce desired film thickness was determined, the influence of various other parameters on surface morphology, mechanical and thermal properties of metal nanocomposites was examined. The first parameter of interest was the concentration of $CuSO_4$ in the electro deposition solution. Nanocomposites were produced at several $CuSO_4$ concentrations for a fixed f-BNNS concentration of 2.5 wt. % f-BNNS. As shown in Figure 20, the electro deposition did not work well at $CuSO_4$ concentrations below 1 M. At higher concentrations, mechanically promising thin films were produced. Then, SEM and EDX were employed to study the surface morphology and verify the homogenous dispersion of building blocks in the matrix as shown in Figure 21.

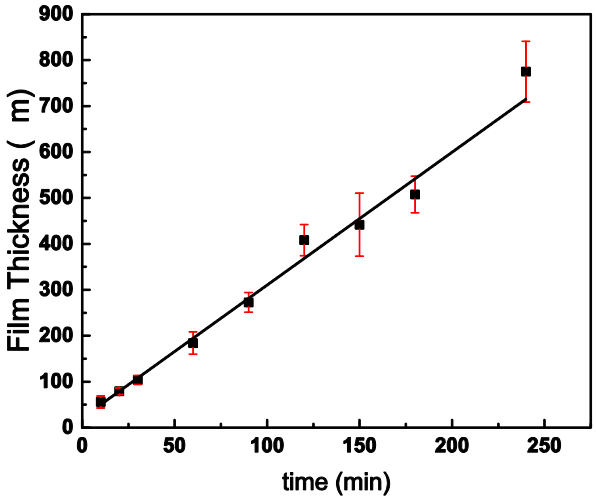

Figure 19 Effect of time on thickness of TIM film

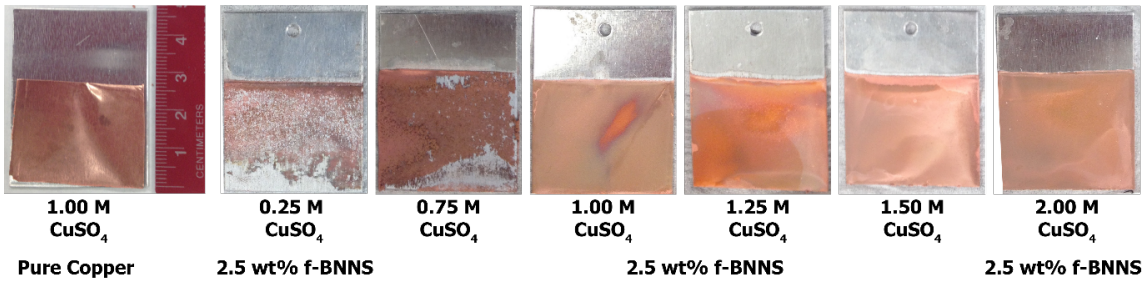

Figure 20 Effect of concentration of CuSO4 in the electrodeposition solution on morphology of the developed TIMs

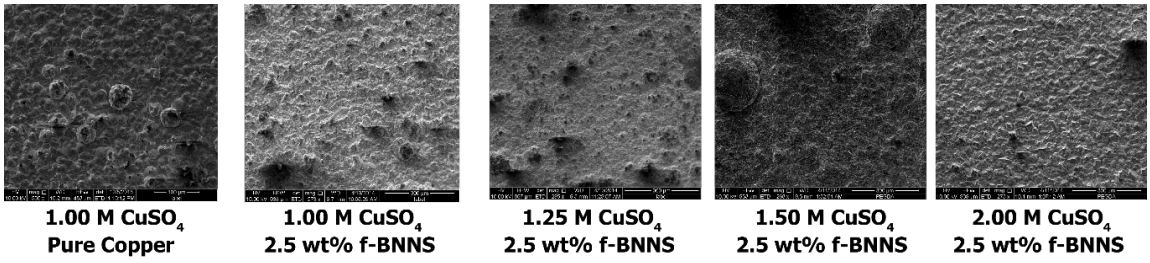

Figure 21 SEM micrographs of nanocomposites involving functionalized BN nanosheets prepared varying CuSO4 concentrations ranging from 1M to 2M.

Effect of Copper Sulfate ($CuSO_4$) Concentration

Figure 21 indicates the SEM micrographs of TIMs involving copper matrix and functionalized-BNNS prepared at varying $CuSO_4$ solution concentrations. Increasing the $CuSO_4$ amount in the solution leads to formation of rougher thin film surfaces. Table 2 summarizes the EDX results giving the average concentration of BN present in the produced nanocomposites. As expected from SEM micrographs, the average BN concentration generally decreases up on increase in the CuSO4 concentration. Even though the lowest BN concentration was obtained at 1.5M $CuSO_4$, overall there is a decreasing trend for BN concentration within the copper matrix. The effective densities of the metal nanocomposite thin films based on the concentrations were calculated to be between 3.4 and 5.8 g/cm^3. [Initially for the preliminary experiment purpose, most analysis were carried out just with EDX for BNNS content and density calculation and precise measurements via elemental analysis and SIMS are done only at the final parameter.]

Regarding the thermal properties, table 3 and table 4 summarizes the specific heat capacity and thermal diffusivity of TIMs obtained using different $CuSO_4$ concentrations respectively. As concentration of copper sulfate increases, specific heat value increases and thermal diffusivity decreases. This is a reasonable trend because higher CuSO4 solution concentration gives rise to nanocomposites with higher copper fraction in comparison to ligand and BNNS.

Table 2 Weight fractions of f-BNNS in nanocomposite matrix and calculated density values as a function of CuSO4 concentration

$CuSO_4$ Concentration (M)	Average BN Concentration on thin film (wt.%)	Density of Nanocomposite (g/cm^3)
1.00	30.8	3.42
1.25	25.2	3.85
1.50	10.6	5.75
2.00	20.2	4.35

Table 3 Effect of CuSO4 concentration on Specific Heat Capacity

$CuSO_4$ Conc. (M)	cp at T=30 ^oC (J/g.K)	cp at T=40 ^oC (J/g.K)	cp at T=50 ^oC (J/g.K)	Average cp (J/g.K)
1	0.343	0.309	0.307	0.319
1.25	0.344	0.322	0.321	0.329
1.5	0.384	0.391	0.399	0.392
2	0.343	0.349	0.345	0.349

Thermal diffusivity decreased by only 2-3% by changing temperature from 25°C to 100°C, indicating that the TIMs developed will not lose their performance by experiencing heating generated by the electronic devices. Table 5 summarizes the corresponding thermal conductivity values for these TIMS. It is important to underline thermal conductivity values as high as ~ 175 W/m.K were obtained.

Table 4 Thermal conductivity of metal nanocomposites as a function of CuSO4 Concentration near room temperature

$CuSO_4$ Concentration (M)	1	1.25	1.5	2
Thermal Conductivity (W/m.K)	110	98	174	113

Table 5 Effect of f-BNNS concentration on thermal diffusivity at temperature between 25 OC and 100 OC

$CuSO_4$ Conc. (M)	Thermal Diffusivity (cm^2/s)				
	T=25 ^oC	T=40°C	T=60°C	T=80°C	T=100°C
1.00	0.945	0.943	0.936	0.939	0.930
1.25	0.744	0.726	0.725	0.726	0.717
1.5	0.789	0.784	0.776	0.759	0.757
2.00	0.759	0.752	0.743	0.747	0.726

Regarding the mechanical properties, Figure 22 displays the mechanical properties of TIMs involving copper matrix and functionalized-BNNS prepared at varying $CuSO_4$ solution concentrations. The reduced Young`s modulus values, Er, ranged from 30 GPa to 50 GPa while hardness values, H, ranged from 0.2 to 0.3 GPa. Moreover, the elastic modulus (E_r) of the thin film corresponding to Er of 30 GPa was calculated to be 27.6

GPa. Though these values are still much lower than pure copper (100-120 GPa for E and 1.1-2.8 GPa for H), the nanocomposites inherit more copper character with increasing $CuSO_4$ concentration in solution.

In addition, we cannot have very low $CuSO_4$ concentrations in solution because, then, electro deposition does not produce robust films. Namely, there is an optimum range of $CuSO_4$ concentration at which electro deposition should be carried out. Our results suggest that the optimum is 1 to 1.5 M $CuSO_4$ in electrolyte solution.

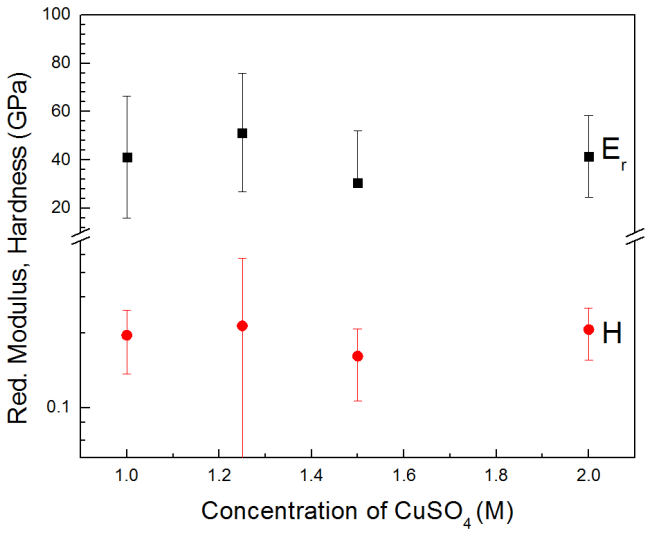

Figure 22 Reduced modulus and hardness values as a function of CuSO4 concentration in the electroplating solution

Effect of Current Density in Electroplating Solution

Next, we investigated the influence of current density on morphological, thermal, and mechanical properties of TIMs developed. Figure 23 shows pictures of the TIMs produced at different current densities. In general, lower current densities produced

smoother and more uniform films. This could be better observed under SEM at higher magnification (Figure 24). At very high current densities (i.e. >20 A/dm^2), the samples become very non-homogenous and brittle (not shown). This is due to the rapid growth of copper crystals at higher current density. In other words, at high deposition rates, the copper crystals do not have enough time to rearrange themselves to tightly pack on the cathode, and hence, leads to rougher films.

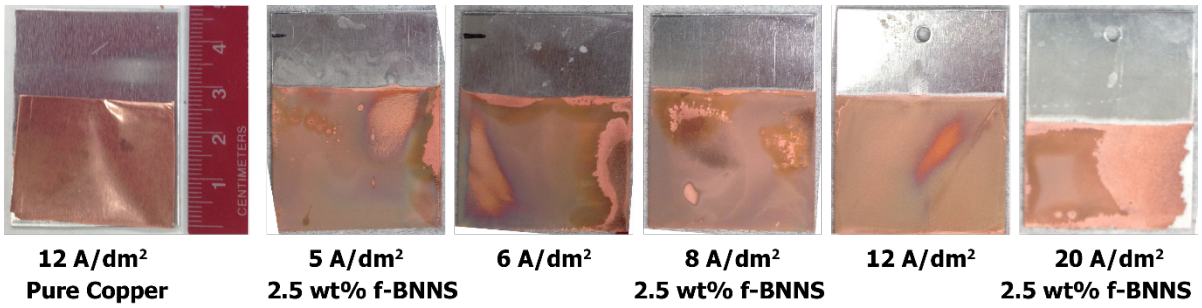

Figure 23 Effect of current density on morphology of the developed TIMs

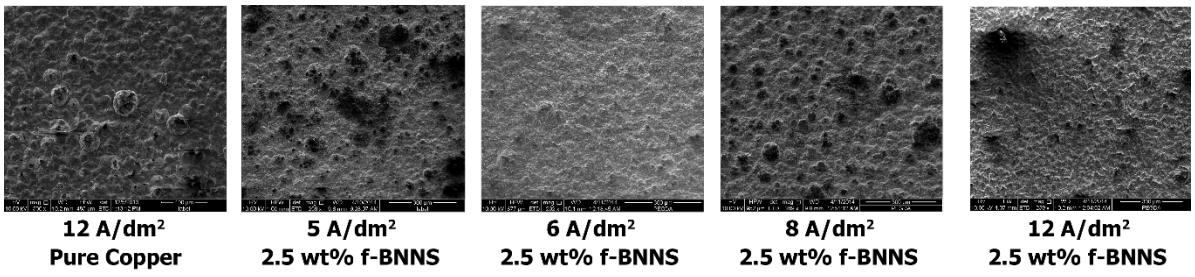

Figure 24 SEM micrographs of nanocomposites involving functionalized BN nanosheets and copper produced at current densities ranging from 5A/dm^2 to 12A/dm^2

As summarized in table 6, EDX analysis showed that average BN concentration in the nanocomposite was 20-30 wt. % for the conditions studied, leading to effective densities of 3.4-4.2 g/cm3.

Regarding thermal properties, once again, we see that specific heat capacity is being mostly constant (Table 7). Here, the values are fluctuated around 0.31-0.32 J/g.K. Though lesser current density makes films smoother, there was no significant change in composition of the material and hence no significant variation in the specific heat capacity values. Similar to the previous cases, thermal diffusivity decreased by only 2-3% by changing temperature from 25°C to 100°C, indicating that the TIMs develop will not lose their performance by experiencing heating generated by the electronic devices (Table 8). The corresponding thermal conductivity values are shown in Table 9. The change in the thermal conductivities was also not large.

Table 6 Weight fractions of f-BNNS in nanocomposites and calculated density values as a function of current density

Current Density (A/dm^2)	Average BN Concentration on thin film (wt.%)	Density of Nanocomposite (g/cm^3)
5	24.6	3.91
6	21.4	4.22
8	25.6	3.82
12	30.8	3.42

Table 7 Effect of current density on specific heat capacity of TIMs developed

Current Density (A/dm^2)	cp at T=30 ^oC (J/g.K)	cp at T=40 ^oC (J/g.K)	cp at T=50 ^oC (J/g.K)	Average Cp (J/g.K)
5	0.309	0.314	0.314	0.312
6	0.317	0.317	0.321	0.318
8	0.304	0.308	0.321	0.311
12	0.343	0.309	0.307	0.320

Table 8 Effect of f-BNNS concentration on thermal diffusivity at temperature between 25 OC and 100 OC

Current Density (A/dm^2)	Thermal Diffusivity (cm^2/s)				
	T=25°C	T=40°C	T=60°C	T=80°C	T=100°C
5	0.766	0.758	0.747	0.739	0.729
6	0.706	0.703	0.697	0.684	0.670
8	0.685	0.668	0.668	0.653	0.642
12	0.945	0.943	0.936	0.939	0.930

Regarding mechanical properties, nanoindentation data is shown in Figure 25. One can see that the reduced modulus and hardness were mostly constant (or very slightly increased) with increasing current density. While the reduced modulus ranged from 20-40 GPa, hardness ranged from 0.15 to 0.40 GPa. Overall, current densities in the range of 5-

12 A/dm^2 are found to be acceptable from mechanical and thermal standpoint. Current densities above 20 A/dm^2 gave rise to brittle films, and are not suitable to grow the films.

Table 9 Thermal conductivity of metal nanocomposites as a function of current density near room temperature

Current Density (A/dm^2)	5	6	8	12
Thermal Conductivity (W/m.K)	92.62	94.36	79.61	110.75

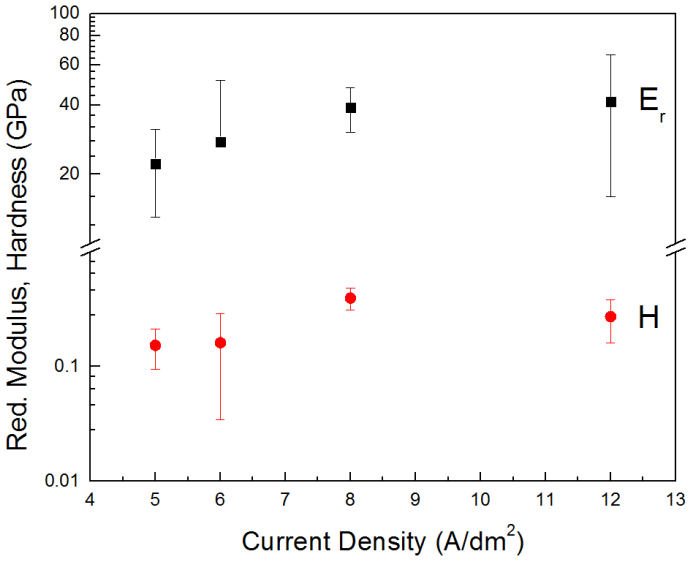

Figure 25 Reduced modulus and hardness values as a function of current density

Effect of f-BNNS Concentration

Later on, with optimized paramters of time, concentration of copper sulpate and optimized electric wave the effect of f-BNNS concentration is studied. Figure 26 shows the secondary ion micrographs obtained for the thin film nanocomposite samples, which were grown on to Al substrates at various electrolyte solutions (low, intermediate and high, respectively). These images, firstly prove the homogeneous dispersion of f-BNNS in the TIM matrix. High intensities of Boron ions were detected on the surface whereas the intensity gradually decreased at the depth of ~1 μm, and eventually stabilized.

As expected, the intensity of the B ions on the nanocomposite TIMs is increasing as the concentration of the solution increases. From the intensity vs. time profiles, it was determined that the intensity of f-BNNS in the nanocomposite samples is linearly increasing with the f-BNNS concentration in the electrolyte solution. The f-BNNS loading in the samples corresponding to the intensity of f-BNNS were determined via chemical elemental analysis. Figure 26d shows the f-BNNS content of the nanocomposite samples as a function of solution concentration.

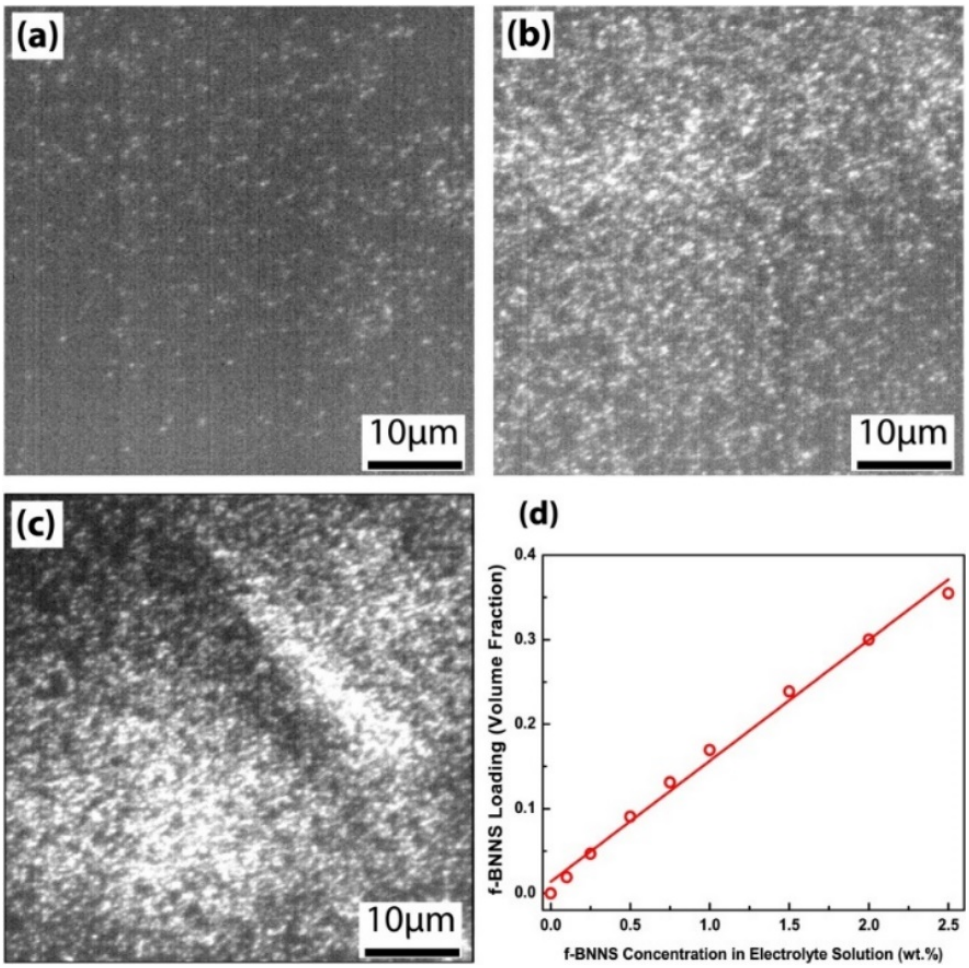

Figure 26 SIMS micrographs (lateral resolution ~3µm) obtained for nanocomposite TIMs at various f-BNNS concentrations in electrolyte solution. (a) low (0.1 wt.%), (b) intermediate (1.0 wt%) and (c) high (2.5 wt.%) concentrations. (White spots indicate B ions) (d) f-BNNS loading in nanocomposite TIMs in terms of volume fraction versus f-BNNS concentration in electrolyte solution.

The bulk thermal conductivity of the nanocomposite TIM, measured via the laser flash diffusion technique as well as the phase-sensitive transient thermo reflectance technique, was found to decrease with increasing amount of f-BNNS in the copper matrix, with diminishing returns (Figure 26a). The reductions due to the presence of organic linker molecules was relatively low (up to 40%, from 370 W/m.K to 211 W/m.K), which is

ascribed to the fact that TSC covalently attaches BNNS to copper matrix. This is consistent with the findings of Losego et al.[180] showing that the strength of a single bonding layer directly governs phonon heat transport across an interface. Strong covalent interactions lead to much higher interfacial thermal conductance in comparison to the weak van der Waals interactions due to ability to form an effective gradient for reducing the impedance mismatch. Furthermore, the localization of TSC at the edges of BN nanosheets can guide phonons through the in-plane direction along nanosheets rather than the out-of-plane direction, along which the thermal conductivity of 2-D materials is about two-orders of magnitude lower than that in the in-plane direction.

The details of complex thermal transport across the metal/inorganic/organic nanocomposite can be explained with a combination of phononic and electronic modes. In the absence of f-BNNS, the system is in a percolated regime with interconnected copper microcrystals where the thermal transport is mostly through electrons. As f-BNNS is introduced into the system, while the degree of percolation of copper microcrystals decreases, new phonon bandwidth emerges via f-BNNS linkers owing to an-harmonic phonon-phonon coupling and electron-phonon coupling at the metal-linker interface.[181] Overall, organic linkers, filtering some phonon modes as well as scattering moieties for electron transport, act as a bottleneck to thermal transport and result in a reduction of thermal conductivity of pure BNNS, and thus the overall composite. Bulk thermal conductivities of copper matrix and f-BNNS calculated according to fit explained by Phelan et al[182] were 370 and 100 W/(m.K), respectively, which are in agreement with recent studies.[183] Introduction of f-BNNS in copper grain boundaries replaces a part of

electronic thermal transport with phonon thermal transport. As f-BNNS loading is increased, more such sites reduce the thermal conductivity until no new sites are occupied by f-BNNS. We see this region is obtained around the 0.12 volume fraction (Figure 27a) and beyond this point, no more reduction in thermal conductivity is observed.

When a heat source and a heat sink are coupled through a TIM, the asperities of heat source/sink surface apply compressive stress in the perpendicular direction to the TIMs. Thus, a nanoindentation technique, involving a very similar geometry, is used as the main mechanical characterization technique in this study. As shown in Figure 27b, the Young's modulus of the hybrid nanocomposite gradually decreased with the increasing f-BNNS content in the hybrid nanocomposite, slowly plateauing around 20 GPa.

This trend can be attributed to the interplay among metallic bonds between copper atoms; van der Waals interactions between copper microcrystals, between copper microcrystals and BNNS, and between BNNS; the bond strengths of ligand-BNNS pair and ligand-copper microcrystal pair; and buckling or bending of BNNS. In the absence of f-BNNS, the mechanical properties of copper are determined by van der Waals forces and metallic bonds holding copper microcrystals together. When f-BNNS is introduced to the matrix, the van der Waals forces between copper microcrystals decrease due to the screening effects induced by the presence of less polarizable materials and the increased distance between microcrystals, which also causes the disappearance of the short ranged inter-crystalline metallic bonds.[184] However, new forces stemming from the linking of copper to BNNS through thiol/copper and amine/BNNS bonds also arise. Because f-BNNS is only functionalized from the edges, the latter effect cannot balance the former

effect, resulting in a reduction in the Young's modulus. As the f-BNNS loading increases, the formation of f-BNNS aggregates between grain boundaries occur. Considering that van der Waals interactions between metals are much higher than that between inorganics or organics, the presence of f-BNNS aggregates, in turn, introduce regions that are held together through weak van der Waals forces in the nanocomposite.

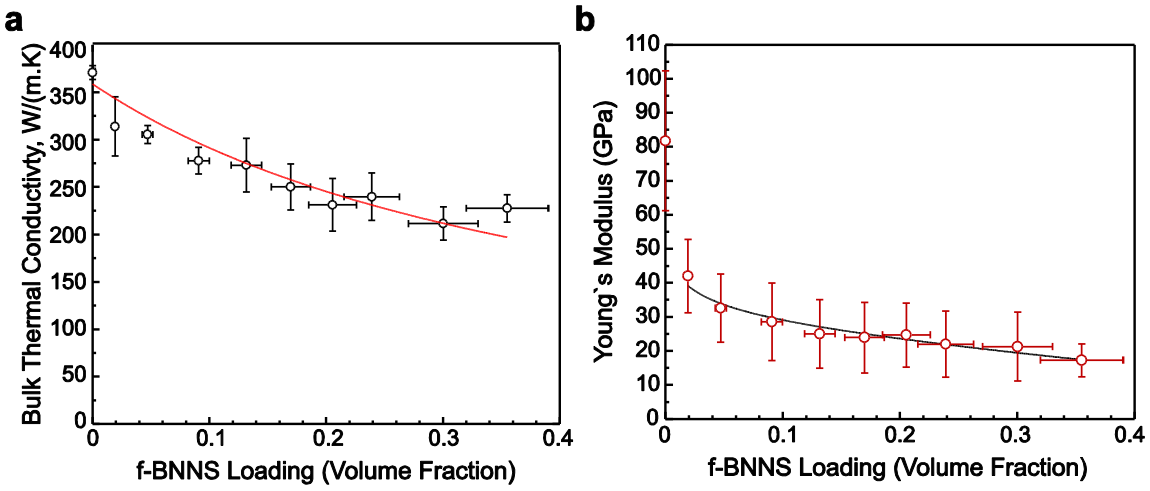

Figure 27 a) The variation in the bulk thermal conductivity of the hybrid nanocomposite TIM as a function of f-BNNS loading. The fit is based on the percolation theory. b) The influence of f-BNNS content on the Young's mod

The modulus values were also obtained from the modified Halpin-Tsai model by considering the f-BNNS as randomly oriented discontinuous fillers:[185,186]

$$E_c = \left[{}^{3}/_{8} \frac{1+2(l_f/d_f)\mu_L v_f}{1-\mu_L v_f} + {}^{5}/_{8} \frac{1+2\mu_T v_f}{1-\mu_T v_f} \right] E_M \qquad (14)$$

where $\mu_L = \frac{(E_f/E_M)-1}{(E_f/E_M)+2(l_f/d_f)}$, $\mu_T = \frac{(E_f/E_M)-1}{(E_f/E_M)+2}$, Ec, EM, Ef are the elastic moduli of the composite, matrix and filler, respectively, l_f, d_f and v_f are the filler thickness, diameter

and volume fraction, respectively. The calculations from the model yielded the elastic moduli of copper and the f-BNNS to be 48.2 GPa and 1.6 GPa, respectively (r^2=0.952). The resultant elastic modulus of pure copper was somewhat lower than the literature value, which is well-known to occur for electrodeposited materials due to the formation of nano- and micro-pores.[187,188] Most organic ligands have elastic moduli less than 1 GPa[189] and the reported out-of-plane bending and in-plane elastic modulus of BNNS are 20-30 GPa[190] and 0.8-1.2 TPa,[191] respectively. In addition, the organic ligands constitute a small fraction of f-BNNS volume (1.4% - 1.2%) due to the functionalization only on the edges. Hence, an effective modulus of 1.6 GPa for the filler implies that f-BNNS behaves closer to the Reuss Model (the lower-bound modulus) where the elastic modulus is averaged via the inverse rule of mixtures.

An electronic package contains various insulating and conducting materials which have different coefficients of thermal expansion (CTE). When an electronic device is powered up so that the package is subject to a temperature change, each material with different CTE deforms at a different rate. This non-uniform CTE distribution typically gives rise to thermally-induced mechanical stresses within the package assembly. Hence, having a CTE value close to semiconductors and heat sink materials are desirable for typical TIMs. TMA measurements revealed that the CTE of the nanocomposite TIM at 12 wt.% loading is 11 ppm/K compared to 17 ppm/K of pure copper as shown in Figure 28. This value of CTE is desirable since the most common chip material – silicon - has a CTE of 2.7 ppm/K and the CTE of our TIMs lie in between the CTE of silicon and common heat sink materials (aluminum (22 ppm/K) and copper (17 ppm/K)). Commonly used

indium or epoxy-based TIMs, which have a typical CTE of 20 ppm/K and 30 ppm/K, respectively, are associated with a higher risk of thermal stress due to a large CTE-mismatch between the heat source and heat sink junctions. As such, the nanocomposite TIMs can reduce mechanical stress due to CTE-mismatch and aid the long-term reliability.

In general, the total thermal resistivity of a TIM strongly depends on its bulk thermal conductivity and Young's modulus, design parameters such as thickness and applied load (or adhesion force), and contact resistance. Hence, to put the measured properties of the hybrid nanocomposites into perspective, we relied on a bulk thermal conductivity versus Young's modulus plot and compared our values with the current-state-of-art and common TIMs (Figure 29).

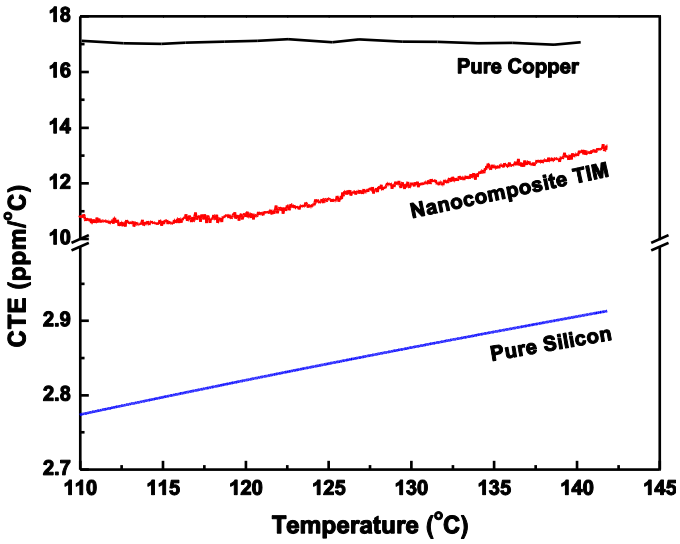

Figure 28 CTE values for the pure silicon, pure copper and nanocomposite TIM compared in the range of 110 ^{O}C -140 ^{O}C. It is very clear from the graph that the CTE of the TIM makes it a perfect bridging material between silicon and copper from the perspective of handling thermal stresses

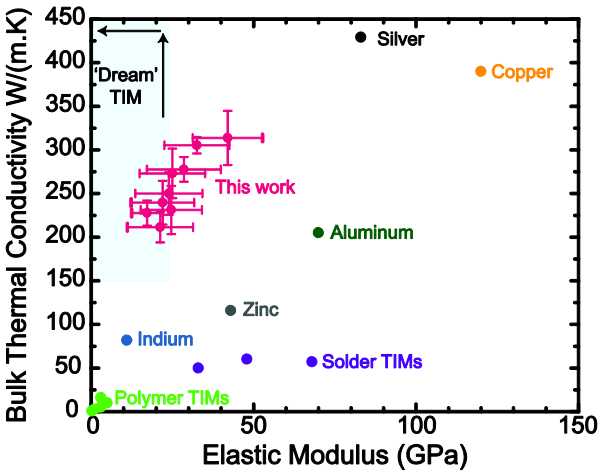

Figure 29 The comparison of bulk thermal conductivity versus elastic modulus values for various types of thermal interface materials and the developed chemically-integrated metal/organic/inorganic nanocomposite thermal interface materials

While the bulk thermal conductivity of the hybrid TIM was only 40% lower than that of pure copper (the base matrix), the compliance of the hybrid TIM was about 4 times larger than that of pure copper. In comparison to polymer TIMs, the hybrid nanocomposite TIMs lead to one-to-two orders of magnitude increase in the thermal conductivity with only a small loss in softness. The developed TIMs thermally outperforms solder TIMs about three- to five-fold while they have similar or a slightly better mechanical compliance than solder TIMs. The combination of these thermal and mechanical properties gave rise to a total thermal resistance of 0.38±0.10 mm^2.K/W for 30 μm bondline thickness and 0.56±0.10 mm^2.K/W for 50 μm bondline thickness under adhesive load. The thermal resistance values contain the contribution from several interfaces and solid layers, but are still very low compared with the traditional TIMs – at least a factor of 5 lower at comparable BLT.

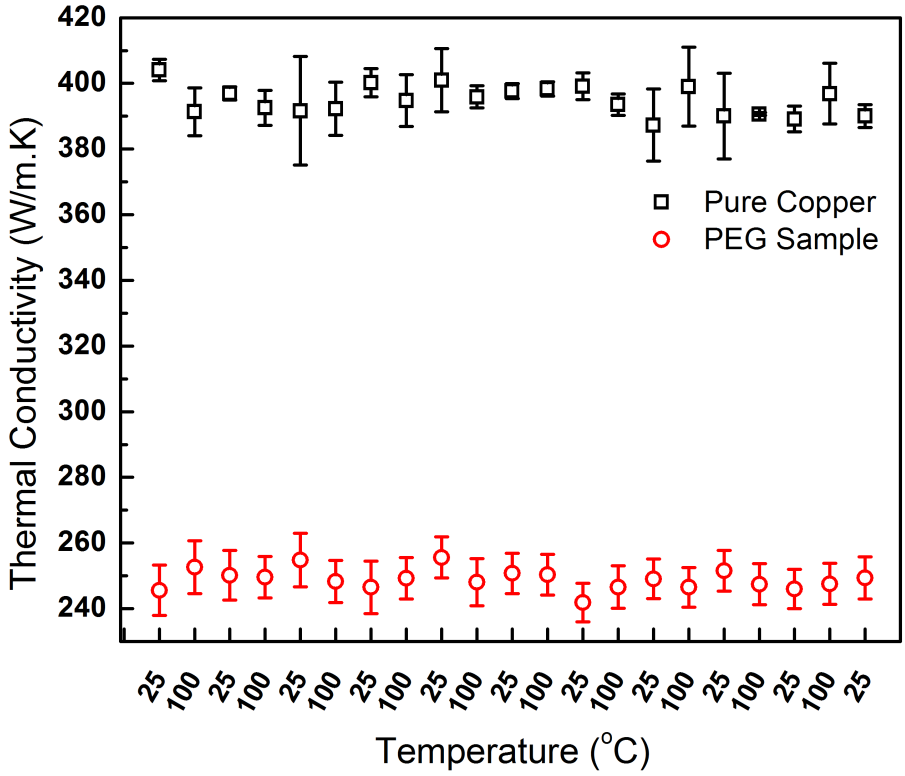

Figure 30 Thermal cycling for electrodeposited pure Cu and hybrid nanocomposite TIMs between 25 °C and 100 °C (each 25-100 in graph corresponds to 5 cycles)

It is crucial to understand the combined effect of time and temperature on the long-term reliability and aging behavior of the developed nanocomposites. Hence, we conducted some "stress tests" by exposing our material via heating-cooling cycles as well to determine if there is any hysteresis in thermal properties. We cycled the samples for 100 cycles varying the temperature from 25°C to 100°C, where most electronic devices are expected to operate. We notice no significant drop in thermal conductivity. The Thermal conductivity for a 4.5 wt% sample changed from 250 W/m.K to 220 W/m.K which corresponds to a change of thermal resistance from 0.38 mm^2K/W to 0.4 mm^2K/W

for a 30 μm sample. In future, we plan to test the TIM over 1000 cycles. This study was shown in the Figure 30.

3.3 Conclusion

Figure 31 gives perspective on the superiority of the produced TIMs in comparison to the currently available TIMs. The chemically-integrated metal/organic/inorganic hybrid nanocomposite provides a promising thermal management solution that can significantly reduce the thermal resistance in high thermal dissipation applications, and can help in achieving the broader goals of compact, high-power-density (electronic) components.

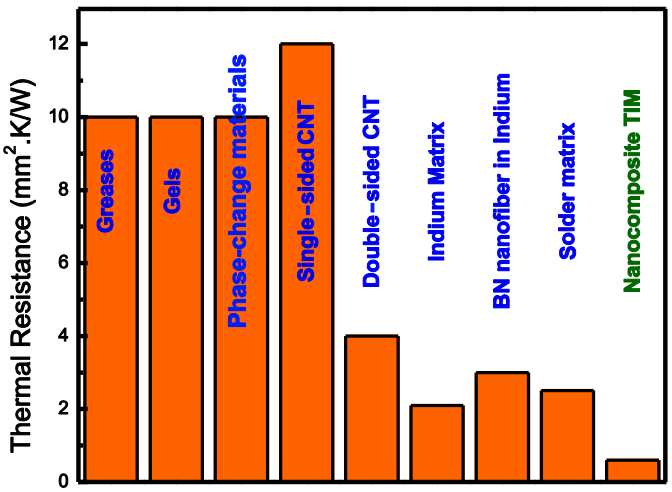

Figure 31 Comparison of resistances for different TIM classes as taken from Narumanchi et al.[192], Indium matrix[193], BN nanofiber in indium[91], solder matrix nanopolymer[89] and this work (Nanocomposite TIM).

4. EFFECT OF LIGAND ON COPPER BASED TIMS AND CORROSIONS RESISTANCE

4.1. Effect of Ligands on the Properties of Copper-based Nanocomposite TIMs

4.1.1. Background

Successful fabrication and characterization of Cu-based organic-inorganic nanocomposite TIMs involving thiosemicarbazide (TSC), as discussed in Chapter 3, motivated us to search for other ligands for functionalization of BNNS. Initially, polyethylene glycol dithiol (PEG-D), a free polymeric ligand was added to the process of fabricating the nanocomposite TIMs involving TSC based on the strong interaction potential of thiol functional groups of PEG-D with the metals.[194] Trace amounts of PEG-D (1 wt.%) reduced the elastic modulus and hardness of the nanocomposite TIMs involving TSC about 35% and 29%, respectively, without significantly affecting the thermal properties. The obtained enhanced mechanical and thermal results in presence of the free ligand indicate that PEG-D strongly bonded to the metal crystals and provided additional enhancement in mechanical compliance of the nanocomposite TIMs.

In the next step, TSC was replaced with various ligands containing different chemical structures and functional end groups. Based on well-established nitrene functionalization of BNNS[144], ligands with amino groups were selected. Additionally, those with chloride and carboxylic acid functional groups were also chosen for possible functionalization reactions. For the metal-ligand side, main functional group was kept as thiols as well as amine groups.[180,194] This initial step for replacing TSC with other ligands is defined to be PHASE I, the details of which will be given later.

In the first phase of the study, although certain literature and chemistry knowledge were employed, the ligand selection was a trial-error process. In PHASE II, a more detailed selection process was followed by interplay of the three functional groups of ligands, two end groups and the central structure, depending on the nature of the interaction that is the point of interest, i.e. while two of those groups were set to be the same the third one was being switched. Detailed chemical structures of the ligands and the corresponding thermal and chemical properties will be included in the next sections.

4.1.2. Materials and Methods

Hexagonal Boron Nitride, h-BN (98%, APS: 0.5 micron), was received from Lower Friction-M.K. IMPEX Corp, (Mississauga, Ontario, Canada). Sulphuric Acid (H_2SO_4, ACS reagent, 95.0-98.0%), Copper (II) Chloride ($CuCl_2$, 99%), Copper Sulfate pentahydrate ($CuSO_4.5H_2O$, ≥98%), Ethylenediamine Tetraacetic acid (EDTA, 99%), and Polyethylene Glycol Dithiol (PEG-D, M_n: 3,400) were obtained from Sigma Aldrich (St. Louis, MI). N-methlyl-2-pyrrolidone (C_5H_9NO, 99%) (NMP) was obtained from VWR (Radnor, PA). Copper sheets were obtained from McMaster Carr (Elmhurst, IL) and Aluminum substrate was obtained from Metals Depot (Winchester, KY). Silicon wafers (Silicon <100> P/Boron, >5000 ohm-cm, doubleside polish, <10 Angstrom R_a) were received from University Wafer (Boston, MA). Thiosemicarbazide (TSC, CH_5N_3S, >98%), Terepthalic Dihydrazide (TD, $C_8H_{10}N_4O_2$, >90.0%), 4-mercaptobenzoic Acid (4-MBA, >95.0%(GC)(T)), 4-cyanobenzoyl Chloride (4-CBC, C_8H_4ClNO, >98.0%), and 2-mercapto-5-benzimidazole carboxylic acid (2-MBC, $C_8H_6N_2O_2S$, >97%), 4-nitrobenzoyl chloride (4-NBC, $C_7H_4ClNO_3$, >98.0%), 4-bromobenzoyl chloride (4-BBC, C_7H_4BrClO,

>98.0%), p-toluoyl chloride (p-TC, C_8H_7ClO, >98.0%), 4-aminobenzenethiol (4-ABT, C_6H_7NS, 98.0%), 4-mercaptotoluene (4-MT, C_7H_8S, >97%), and 3-mercaptopropionic Acid (4-MPA, $C_3H_6O_2S$, >98%) were obtained from TCI America (Portland, OR).

Covalent functionalization of BNNS with thiosemicarbazide (TSC) and terepthalic dihydrazide (TD) was achieved by the same protocol: BNNS with ligand in NMP were mixed with the ratio of 1:10:100 in weight, and heated. The reaction took place at 170 ˚C for 30 hours under nitrogen flow. The obtained product was dialyzed in NMP for 10 hours to remove the unreacted ligands, followed by centrifugation at 3500 rpm for 15 minutes. Next, the supernatant was removed; the precipitate (functionalized BNNS, f-BNNS) was dried at 75 ^{o}C in a vacuum furnace for further removal of the remaining NMP from f-BNNS powder.

BNNS were functionalized with 2-Mercapto-5-benzimidazolecarboxylic acid (2-MBA) and 4-mercapto benzoic acid (4-MA) with the same method: The ligand the the BNNS were used at a ratio of 5:1 in weight. The ligand was fully dissolved in H_2O and a trace amount of EDTA was added to the aqueous solution. Then, the BNNS was added to the solution and stirred for 12 hours. The stirred solution was rinsed with 5 liters of H_2O, and to remove the excess ligands, the solution containing 2-MBA was filtered with a 400 nm size filter while that containing 4-MA was filtered with a 250 nm one. The residues were collected and dried at 60 ^{O}C for 24 hours.

The functionalization protocol with 4-cyanobenzoyl chloride (4-CBC), 4-nitrobenzoyl chloride (4-NBC), 4-bromobenzoyl chloride (4-BBC), p-toluoyl chloride (p-TC), 4-aminobenzenethiol (4-ABT), 4-mercaptotoluene (4-MT), and 3-

mercaptopropionic Acid (4-MPA) was the same: BNNS and the ligand were mixed in a flask at a ratio of 1:3 in weight, and kept at 125 ^{O}C for 96 hours under nitrogen flow. A condenser was connected to the flask to prevent the escape of the evaporated ligand. The product of the reaction was rinsed with ethanol for removal of excess ligand. Then, the residual product centrifuged at 4000 rpm for 15 minutes to remove the remaining ethanol. The final product was dried at 50 ˚C for 24 hours.

The functionalization reactions and possible chemical interactions were verified via ATR-FTIR method. The infrared spectra were measured using a Shimadzu IRPrestige-21 system.

The electrodeposition of Cu/f-BNNS thin film nanocomposite TIMs involving various ligands (TSC, TSC+PEG-D, TD, 2-MBC, 4-MBA, 4-CBC, 4-NBC, 4-BBC, p-TC, 4-ABT, 4-MT and 3-MPA) were achieved with the same electrolyte solution described in Section 3.1.3. The thin film samples were grown onto aluminum sheets and some of these samples were also grown onto the silicon wafers for contact resistance measurements. Microstructural analysis, and mechanical/thermal characterization of Cu-based nanocomposite TIMs were completed by the same techniques described in Sections 3.1.4.

4.1.3. Results and Discussion

Phase I

Figure 32 illustrates the five types of ligands used for functionalization in PHASE I. These functional groups were especially selected due to their bifunctional nature and the

presence of amino groups, which can react with defective sites of BNNS, and cyano, thiol and amino groups, all of which can form complexes with copper.

All functionalization reactions were characterized by FTIR analysis, and the selected FTIR spectra for 2-MBC acid are shown in Figure 33. The comparison of spectra for the pure ligand and ligand functionalized BNNS indicates that the peaks at 1525 cm^{-1}, 1608 cm^{-1}, 1740 cm^{-1}, and a broad peak at 3050 cm^{-1} disappeared upon functionalization reaction, suggesting that 2-Mercapto-5-benzimidazolecarboxylic acid indeed reacted with BNNS (Figure 33).

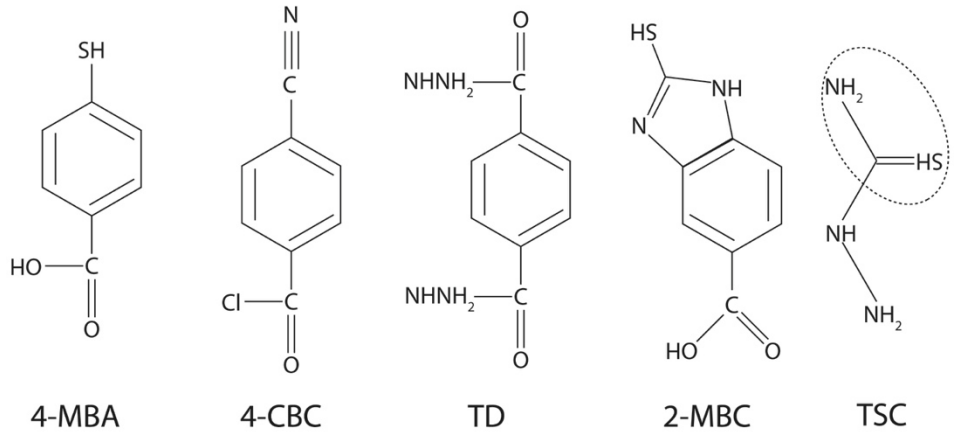

Figure 32. Ligands used in PHASE 1. 4-MBA (4-mercaptobenzoic acid), 4-CBC (4-cyanobenzoyl chloride), TD (terepthalic dihydrazide), 2-MBC (2-mercapto-5-benzimidazole carboxylic acid), and TSC (thiosemicarbazide)

Figure 34a&b depict the thermal conductivity measurements and nanoindentation test results of the Cu/f-BNNS nanocomposite TIMs, respectively; obtained from the cases of several ligands illustrated in Figure 32. The results from the initial case when PEG-D was added as a free ligand are also compared with the others.

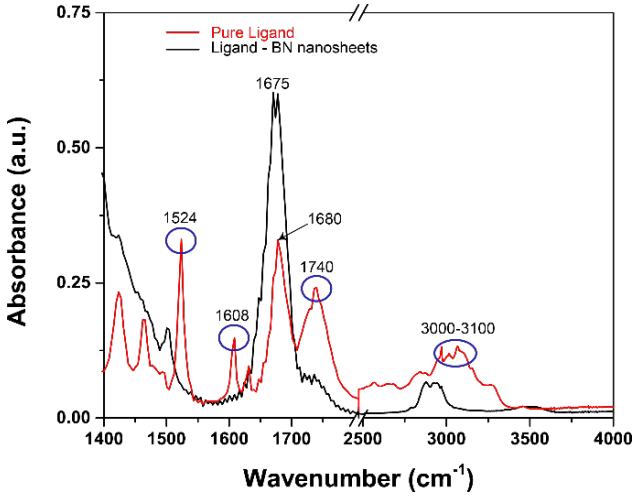

Figure 33. FTIR spectra of pure 2-MBC and f-BNNS with 2-MBC

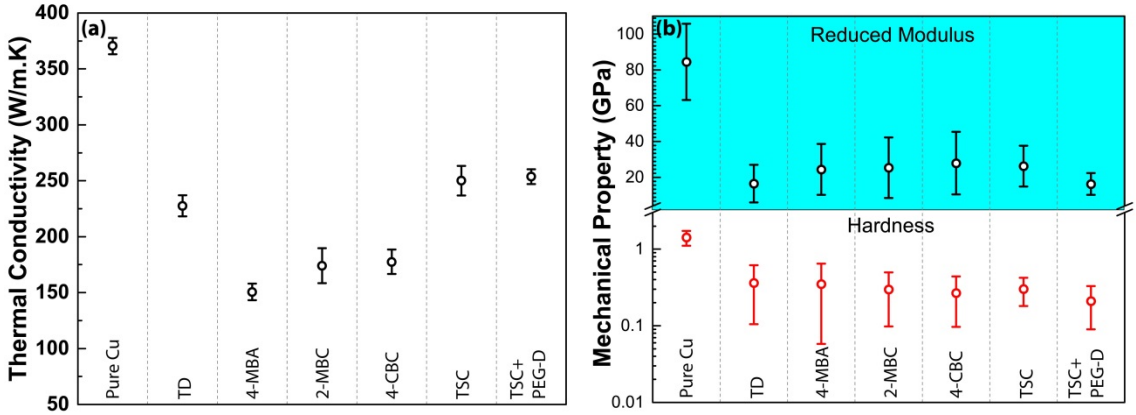

Figure 34. PHASE I effect of organic ligands on. a) thermal conductivity and b) mechanical properties of Cu/f-BNNS thin film nanocomposite TIMs (Abbreviations: TD-Terepthalic dihydrazide, 4-MBA: 4-Mercaptobenzoic acid, 2-MBC: 2-Mercapto-5-benzimidazolecarboxylic acid, 4-CBC: 4-Cyanobenzoyle chloride, TSC: Thiosemicarbazide, TSC+PEG-D: Thiosemicarbazide with PEG-dithiol)

It was observed from the Figures that the TSC (and TSC with PEG-Dithiol) had the best performance due to highest thermal conductivity, and lowest modulus and hardness value. However, it is important to note that the parametric investigation for each

ligand has not yet been performed, which is one of tasks to be completed.The phase-sensitive transient thermoreflectance (PSTTR) technique, the details were given in appendix A, was used as the second method to measure the thermal properties of the developed nanocomposite TIMs. For this purpose, the Cu/f- BNNS nanocomposite TIMs with thicknesses in the range of 30-60 μm were electrodeposited onto circular silicon wafers. To maintain the electrical conductivity of the cathode, the Si wafers were initially coated with a 300 nm Cu layer via e-beam evaporation.

Figure 35a shows the picture of the obtained Cu/f-BNNS nancomposite TIMs involving the TD and TSC. For an initial analysis, Cu/f-BNNS nanocomposite TIMs involving TSC, TSC+PEG-D and TD were measured. Three samples from each condition were measured for error analysis. Contact resistance and overall thermal resistance (sum of the contact resistance at the Si wafer-TIM interface and bulk thermal resistance of the TIM) of the samples are summarized in Table 11.

One sided configuration denotes that the thermal analysis of the samples was performed without sandwiching the TIMs between two Si wafers, as shown in Figure 35b. It is apparent from the results in Table 11 that the single-sided TIM produced with f-BNNS (involving TS functionalization) and 1 wt.% PEG-D gave the minimum overall thermal resistance. It has been shown that TSC has been the best ligand in terms of thermal and mechanical properties among all ligands, in both free standing thermal measurements with DLF and contact resistance measurements with PSTTR. Addition of PEG-D further enhanced the mechanical and thermal properties of the nanocomposite TIMs.

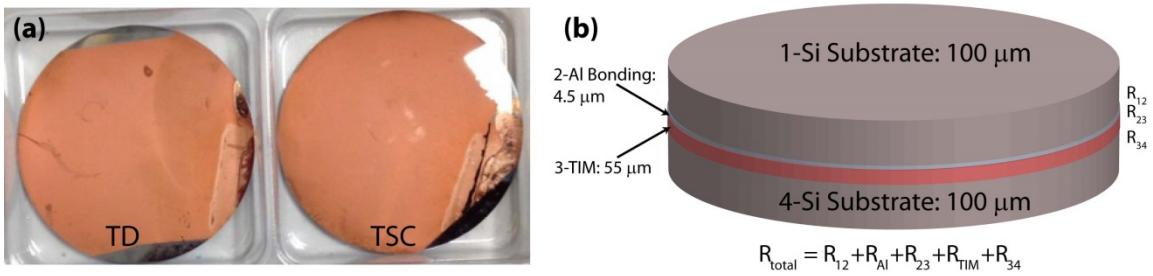

Figure 35. a) Single sided samples that were fabricated by growing Cu/f-BBNS nanocomposite TIMs onto silicon wafers. b) schematic indication of sandwich samples where the single sided samples were attached to a bare silicon wafer with a 4.5 mm aluminum diffusion layer.

Table 10 Contact and overall thermal resistance values of pure copper and Cu/f-BNNS thin films involving different ligands

Ligand	Pure Cu	TSC		TSC (5 wt%) + PEG-D		TD
filler (wt %)	-	f-BNNS (5)	f-BNNS (10)	PEG-D (1)	PEG-D (3)	f-BNNS (5)
Contact resistance	0.15±0.04	0.1±0.02	0.13±0.03	0.11±0.03	0.17±0.03	0.14±0.01
Overall resistance	0.3±0.06	0.34±0.03	0.32±0.04	0.26±0.04	0.31±0.06	0.45±0.04

Phase II

In this phase, a more systematic investigation on functionalization of BNNS with respect to ligand functional groups was performed. Since TSC was determined to be the

best ligand in the previous phase, the obtained results from new ligands (Figure 36) were compared to it.

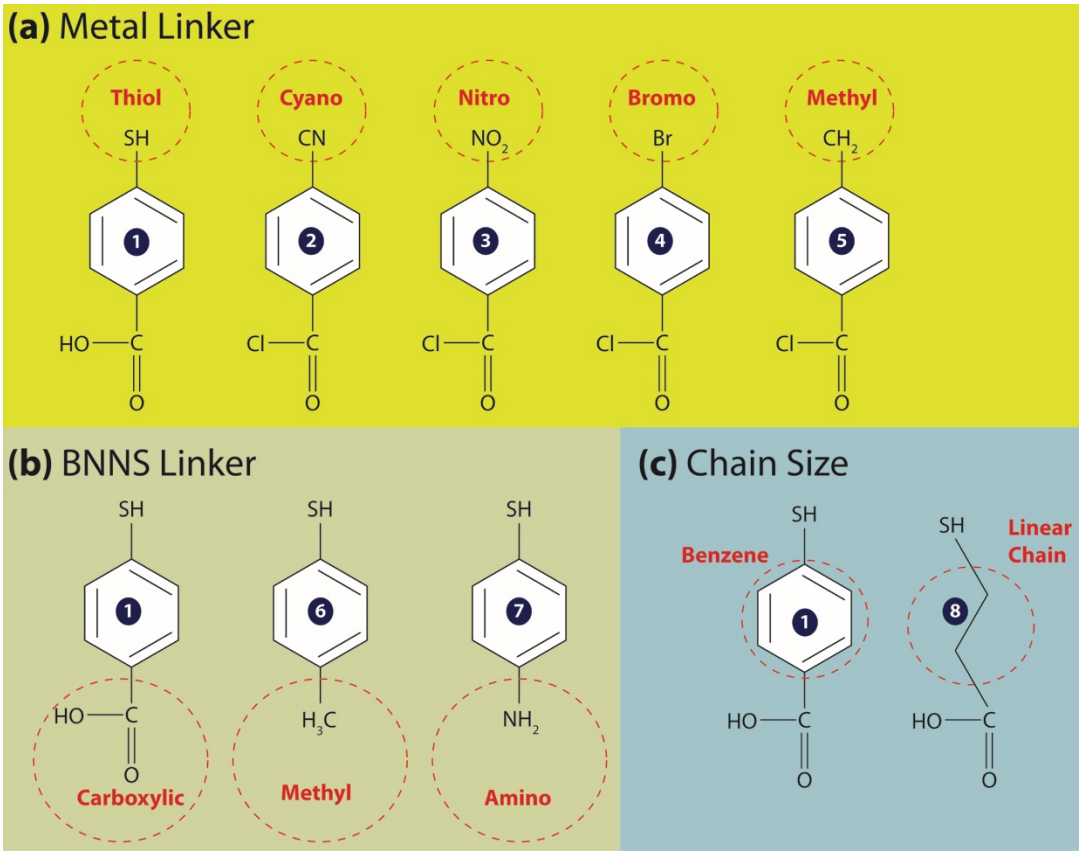

Figure 36. Types of ligands in PHASE II with respect to their functional groups. In Category a) five ligands with varying groups to link to the metal crystals, in Category b) three ligands that may be bonding with the filler, BNNS, and in Category c) ligands having different chain size or central functional group. Numbering: 1) 4-MBA (4-mercaptobenzoic acid), 2) 4-CBC (4-cyanobenzoyl chloride), 3) 4-NBC (4-nitrobenzoyl chloride), 4) 4-BBC (4-bromobenzoyl chloride), 5) p-TC (p-toluyl chloride), 6) 4-ABT (4-aminobenzenethiol), 7) 4-MT (4-mercaptotoluene), and 8) 4-MPA (3-mercaptopropionic Acid). Ligand 1 (4-MBA) is common in all categories.

Figure 36a categorizes the selected ligands for metal-ligand interactions into thiol, cyano, bromo, nitro and methyl groups, while the other end group is used in

functionalization reaction with BNNS. Moreover, in Figure 36b, setting the metal-ligand interaction group as the thiol, the functional groups that will be employed in functionalization reaction are classified as carboxylic, methyl and amino groups. Finally, the chain structure of the ligands is compared in Figure 36c. 4-MBA, ligand 1, is common for all categories.

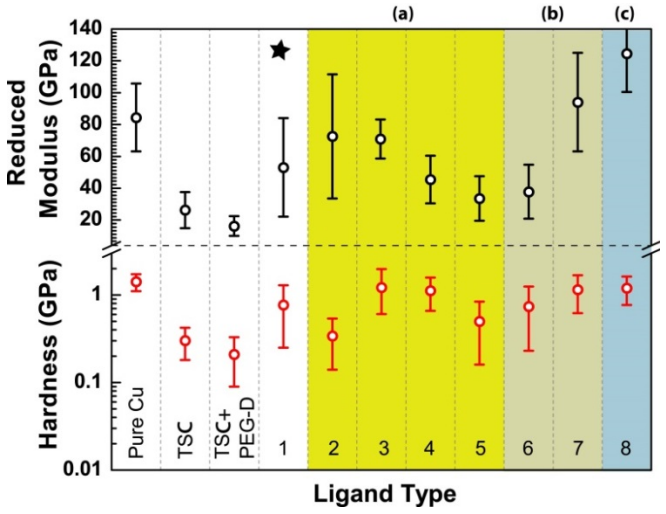

Figure 37. PHASE II effect of organic ligands on mechanical properties of Cu/f-BNNS thin film nanocomposite TIMs. Numbering: 1) 4-MBA (4-mercaptobenzoic acid), 2) 4-CBC (4-cyanobenzoyl chloride), 3) 4-NBC (4-nitrobenzoyl chloride), 4) 4-BBC (4-bromobenzoyl chloride), 5) p-TC (p-toluyl chloride), 6) 4-ABT (4-aminobenzenethiol), 7) 4-MT (4-mercaptotoluene), and 8) 4-MPA (3-mercaptopropionic Acid).

Reduced elastic modulus and hardness values of Cu/f-BNNS nanocomposite TIMS involving all abovementioned ligands were obtained and shown in Figure 37, and corresponding thermal conductivity values are depicted in Figure 38. Among all the ligands, mechanical analysis on the nanocomposite TIMs involving TSC and TSC+PEG-

D resulted in the lowest elastic modulus and hardness. Mechanical test results of the samples marked as 7 and 8 were close to those of pure Cu, which may be attributed to low affinity of the corresponding ligands (4-MT and 4-MPA) towards the copper matrix. Although these ligands had thiol functional groups, which are known to highly interact with metals, the affinity of the chemical plays a significant role on bonding of the structures.

It is seen from Figures 37 and 38 that the nanocomposite TIMs corresponding to ligands 5 (p-TC) and 6 (4-ABT) gave comparatively better values than their counterparts in terms of higher thermal conductivity and lower elastic modulus/hardness. Although it is difficult to draw conclusions from the chemical and thermomechanical characterization results, some intuitive results can be obtained from microstructural analysis of the nanocomposite TIMs. Figure 39 depicts the secondary electron micrographs of the selected nanocomposite TIMs involving the ligands 1, 5, 6 and 8. One ligand from each category (Fig. 36) was chosen and the dispersion behavior of f-BNNS in the metal matrix was investigated.

It is shown in Figure 39a that the f-BNNS involving ligand 1 is aggregated at grain boundaries with tiny clusters. In Figure 39b&c, for ligands 5 and 6, the filler is shown to have less aggregation and more uniform dispersion, which the more promising thermal and mechanical test results can be attributed.

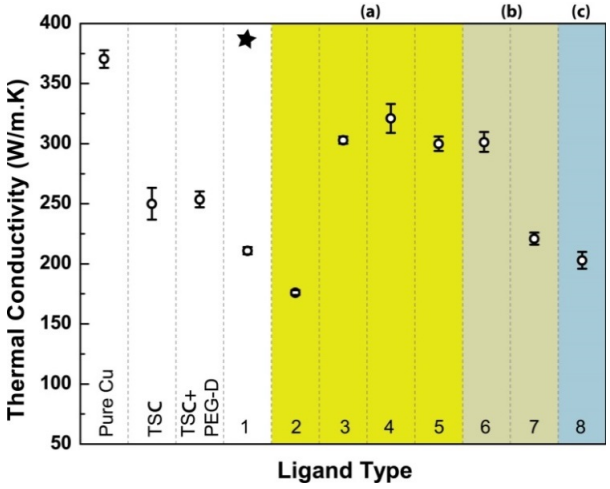

Figure 38. PHASE II effect of organic ligands on thermal conductivity of Cu/f-BNNS thin film nanocomposite TIMs. Numbering: 1) 4-MBA (4-mercaptobenzoic acid), 2) 4-CBC (4-cyanobenzoyl chloride), 3) 4-NBC (4-nitrobenzoyl chloride), 4) 4-BBC (4-bromobenzoyl chloride), 5) p-TC (p-toluyl chloride), 6) 4-ABT (4-aminobenzenethiol), 7) 4-MT (4-mercaptotoluene), and 8) 4-MPA (3-mercaptopropionic Acid).

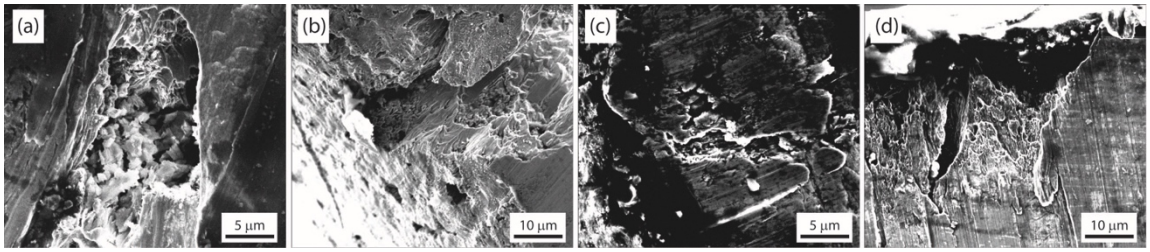

Figure 39. Secondary electron micrographs of the Cu/f-BNNS nanocomposite TIMS involving. a) 4-MBA (ligand 1), b) p-TC (ligand 5), c) 4-ABT (ligand 6), and d) 4-MPA (ligand 8)

In Figure 39d, the filler tends to aggregate at certain locations of the nanocomposite at low concentrations. Low level of attachment may be due to the low affinity of the ligand to the metal matrix, which may explain the sample`s mechanical properties similar to pure Cu. On the other hand, its low thermal conductivity may be

because of the aggregation and phonon scattering behavior of the ligands (see Chapter 3 for more detailed discussion on phononic thermal transport).

4.2. Effect of Ligands on Cooling Performance of Nanocomposite TIMs

The most important task of a thermal interface material is to efficiently cool down an electronic system. Hence, cooling performance of TIMs plays a crucial role in their commercial value. Cooling performance of the nanocomposite TIMs was measured using a simple setup where the TIM was placed between an old electronic component and a heat sink, which were disassembled from an old server. The electronic component was heated to 65 ^{O}C and its cooling process was observed with an infrared thermal camera (FLIR A655ss IR Camera). The time it takes to cool down the component to 45 ^{O}C was recorded for each TIM. The camera records of the thermal performance tests are in the link below:

https://www.youtube.com/watch?v=EJl_XJNhJgo

As an initial evaluation, three samples were compared: (i) first record was taken in absence of a TIM, (ii) a commercially available TIM was tested, and (iii) finally the response from the fabricated nanocomposite TIM (Cu/f-BNNS involving TSC) was recorded. The records indicate that this process took 14:28 seconds, 7:34 seconds and 4:63 seconds with bare heat sink, commercial TIM and our nanocomposite TIM, respectively. Hence, we obtained a 40% higher performance with the developed nanocomposite TIM than the commercial one.

Effect of ligands on cooling performance of the nanocomposite TIMs was also observed following the initial evaluation. The nanocomposite TIMs involving the ligands that were investigated in PHASE I (TSC, TSC+PEG-D, TD, 4-CBC, 2-MBC, 4-MBA)

were placed between two mating surfaces and cooling time of each TIM was recorded as shown in the video below;

https://www.youtube.com/watch?v=OpycWTRi-Pc

The shortest cooling time, 5.14 seconds, was obtained by the TIM involving TSC as it resulted in the most promising thermal and mechanical results. In was unexpected that the sample corresponding to TSC+PEG-D showed lower performance with a cooling time of 11.27 seconds, while that corresponding to 4-CBC cooled down the system in 6.09 seconds.

In summary, the nanocomposite TIMs produced in this project worked very well and gave rise to higher cooling performance than other commercial TIMs. It also needs to be claimed that the commercial TIM used in this experiment contains adhesives that help firmly stick to the heat sink surface and reduce thermal resistance. On the other hand, our nanocomposite TIM did not contain any adhesives, which introduced a higher thermal contact resistance than its commercial counterpart. As a further development of cooling performance, direct deposition of the nanocomposite TIMs on to heat sink/chip surfaces would eliminate the contact resistance. By this way, we expect to further enhance the cooling performance of the nanocomposite TIMs.

4.3. Corrosion Protection Behavior of Nanocomposite TIMs

4.3.1. Background

Corrosion is described as a chemical/electrochemical interaction of a material with the environment causing gradual destruction of the properties of this material, especially metals. It is a significant issue in numerous industries including automotive, energy,

aviation, shipping, infrastructure, and electronic industries,[195,196] and its annual cost to U.S. economy is hundreds of billions of dollars.[195,197] Extensive researches have been conducted to inhibit the corrosion in metal surfaces via protective layer coating. In the last few decades, chemically stable and corrosion resistant platinum group metals,[198] electro-active conducting polymers[199,200] and self-assembled monolayers[201] have been used as corrosion resistant coatings on metal surfaces despite their drawbacks such as limited availability, high temperature instability and alteration of the surface properties of metals.[202] Graphene has recently been introduced as an effective corrosion protection material[197,203–205] on various metals such as copper, gold and nickel, in the form of both individual ultra-thin coating and dispersant in protective polymers.[202,206] However, later investigations have indicated that graphene leads to acceleration of corrosion in long term due to possession of defective sites.[207,208] On the other hand, boron nitride nanosheets (BNNS), a structural analog of graphene, have emerged as an outstanding corrosion inhibitor due to its natural hydrophobicity and impermeability, thermal and chemical stability.[209–211] Corrosion protection of metals and polymers has been reported in presence of BNNS: Li et al. prevented the corrosion of copper surfaces by forming a thin layer of BNNS via chemical vapor deposition,[211] while Sun et al. achieved the same task by coating the copper surface with a polymer composite produced by dispersion of BNNS in polyvinyl butyral (PVB).[209] Also, Yi et al. have shown the oxygen-atom corrosion protection of polymers in presence of BNNS coating.[212]

In electronic systems, metallic components are vulnerable to corrosion due to humidity and temperature, which reduces the yield of these components and ultimately

cause electrical failures.[213] Thermal interface materials (TIMs) are major components of electronic systems that are designed to prevent overheating of the other components of the system and enhance their lifetime. Hence, TIMs require enhanced corrosion protection to maintain their performance and reliability, which in turn yields high performance of the whole system. Up on this purpose, corrosion performance of the fabricated metal-based nanocomposite TIMs was investigated. Instead of forming a protective layer on these TIMs as reported in the literature, BNNS were incorporated into copper matrix to form a copper-based nanocomposite. The BNNS were initially functionalized with a soft ligand, thiosemicarbazide (TSC), to prevent the aggregation of individual sheets and provide uniform dispersion in the matrix. Then, copper-based nanocomposite TIMs (Cu/f-BNNS) were fabricated via novel electrocodeposition method, in which the nanocomposite TIMs were grown onto aluminum substrates. The corrosion protection properties of Cu/f-BNNS nanocomposite samples were determined by Tafel polarization. Then, the corrosion activity of Cu-based nanocomposite TIMs was also analyzed by high-resolution scanning electron microscopy (HRSEM), and energy-dispersive X-ray spectroscopy (EDX).

4.3.2. Materials and Methods

Thin film nanocomposite TIMs were grown on aluminum sheets. The aqueous electrolyte solutions were prepared by 1 M $CuSO_4.5H_2O$, 1.8 M H_2SO_4, a trace amount of $CuCl_2$, and 1.25 wt.% f-BNNS. Each solution was transferred to the electroplating cell after sonication for homogenous dispersion of f-BNNS. A pure copper sheet (>99%) and a substrate were used as anode and cathode, respectively. The electrical power source was a Nuvant Powerstat05 Potentiostat (Nuvant Systems Inc., Crown Point, IN). The

electrodeposition was carried out at a current density of 10 A/dm^2 and AC frequency of 950 Hz with 30% off time.

All the electrochemical measurements were performed using the Gamry Instruments Potentiostat (Interface 1000 model), in a standard three electrode system at 298 K. An aerated solution of 3.5 wt.% NaCl was used as electrolyte throughout the study. The electrochemical cell consists of copper or copper metal matrix composite with an exposed area of 1 cm^2 served as the working electrode, a saturated Ag/AgCl electrode as the reference electrode, and a Pt/Nb mesh electrode of 2 cm diameter as the counter electrode. The working electrode was immersed in the testing solution for 1 hour to reach a quasi-stationary value of the open circuit potential prior to measurement. The potentiodynamic polarization measurements were carried out in the potential range from -300 mV to +300 mV vs open circuit potential with the scanning rate of 0.5 mV/s. All the experiments were repeated for at least 3 times to ensure good reproducibility of the results.

The corrosion current densities (i_{corr}) were determined by extrapolating the linear portion of the anodic polarization curves to E_{corr}. The corrosion rate (CR) was calculated from the corrosion current by using the following equation:

$$CR = 3.268\, x\, 10^3\, \frac{Jcorr}{\rho}\left(\frac{MW}{Z}\right) \quad (15)$$

where MW is molecular weight of copper in g, ρ is the density of Cu (8.92gcm^{-3}) and Z is the number of electrons transferred.

The microstructures of samples before and after polarization were examined using a high-resolution scanning electron microscopy (Tescan LYRA-3 Model GMH Focused Ion Beam Microscope) at an accelerating voltage of 20.0 kV. Additionally, elemental

mapping were also performed using energy-dispersive X-ray spectroscopy (Standard EDS Microanalysis System with X-MaxN 50) to determine the presence of each atom in both cases.

4.3.3. Results and Discussion

Figure 40 presents the potentiodynamic polarization curves of pure copper and Cu/f-BNNS nanocomposite TIMs obtained from electrochemical tests. Appearance of lower peak corresponding to Cu/f-BNNS nanocomposite TIM suggests the lower corrosion current passing through the sample, which can be attributed to better anticorrosion performance of Cu/f-BNNS sample than that of pure copper.

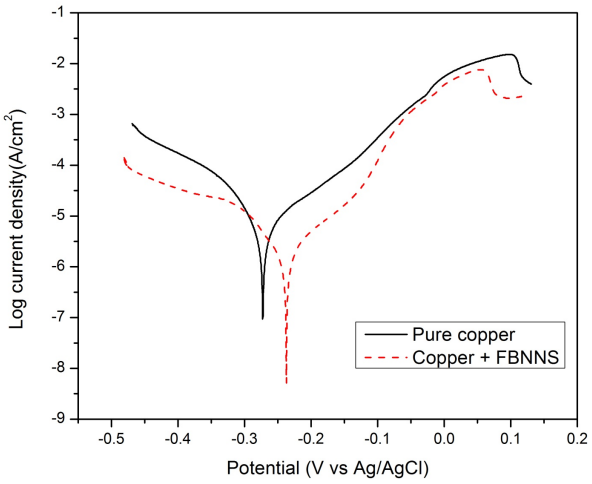

Figure 40. Potentiodynamic polarization curves for. a) pure cupper and b) Cu/f-BNNS nanocomposite TIMs

Corrosion rates that were calculated by using the obtained inputs from electrochemical tests are depicted in Table 11. The corrosion rate of Cu/f-BNNS samples

Table 11 Summary of experimental parameters and calculated corrosion rate: Ecorr represents the potential, Jcorr is the current density, and βc and βa are cathodic and anodic slopes, respectively.

Sample	Parameters				
	E_{corr} (mV)	J_{corr} (μAcm^{-2})	β_c ($mV.dec^{-1}$)	β_a ($mV.dec^{-1}$)	Corrosion rate (mmy^{-1})
Pure Cu	-271	6.33	-143	105	0.0737 ± 0.005
Cu/f-BNNS	-227	1.75	-177	65	0.0204 ± 0.005

(0.0204±0.005 mmy^{-1}) were found to be near 72% less than that of pure Cu samples (0.0737±0.005 mmy^{-1}), which indicates the superior corrosion performance of the nanocomposite TIMs in presence of f-BNNS. Figure 41 shows the high resolution secondary electron micrographs of the pure Cu and Cu/f-BNNS nanocomposite samples obtained before and after the electrochemical tests. The pure Cu sample has a rough surface and contains numerous pores and grain boundaries, while these vacancies were filled with the f-BNNS in the Cu/f-BNNS nanocomposite TIM. It is clear from the micrographs that the surfaces of both samples were deteriorated upon exposure to the NaCl during the electrochemical test. The degree of deterioration in the Cu/f-BNNS nanocomposite sample is shown to be less severe than that of pure Cu sample, which can be attributed to the enhanced corrosion performance of the nanocomposite sample.

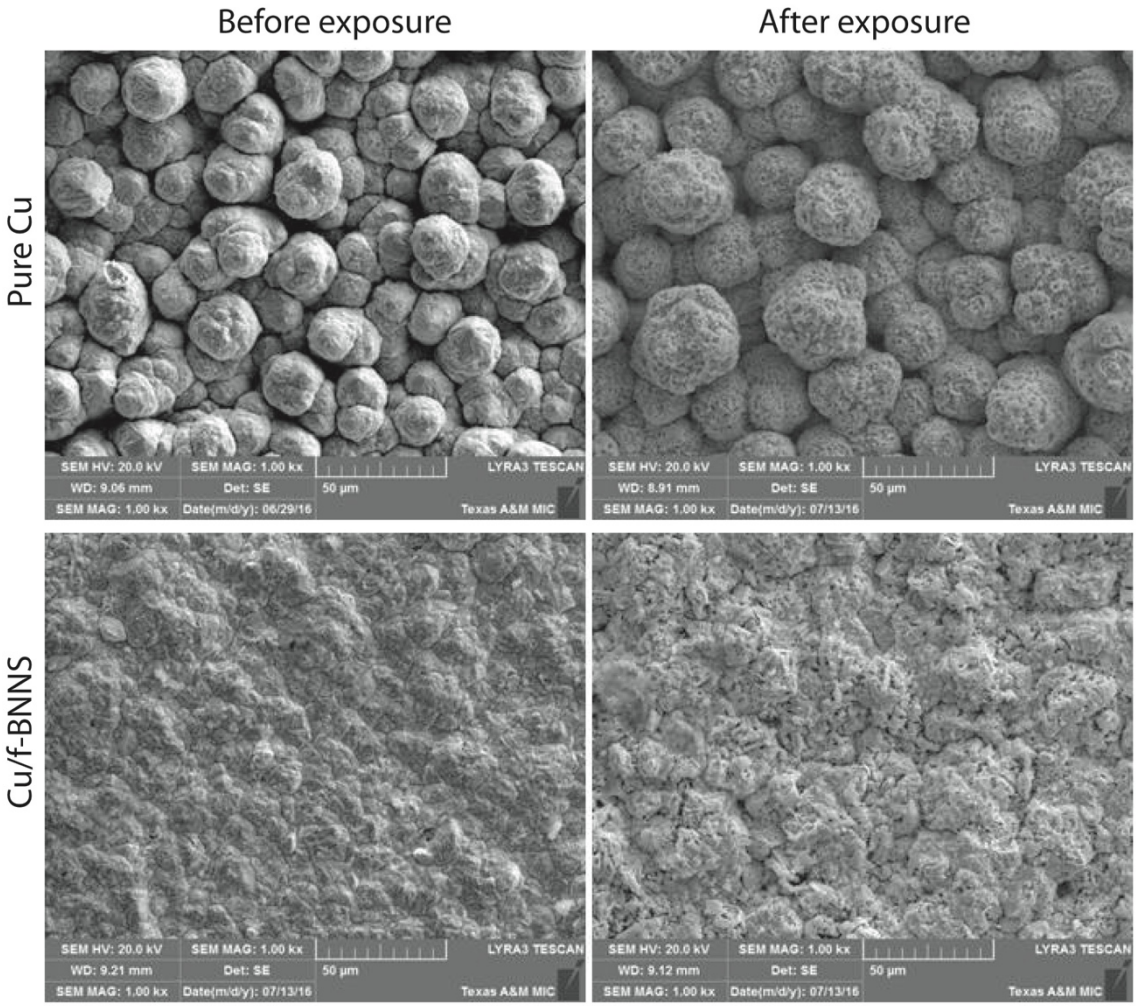

Figure 41. High resolution SEM images obtained from the Pure Cu and Cu/f-BNNS nanocomposite TIMs before and after electrochemical tests

Figure 42 presents the high resolution FIB images of the Cu/f-BNNS nanocomposite sample taken before polarization (two images on the left). The f-BNNS at the copper grain boundaries are obviously shown in the images. To verify the presence of the elemental mapping for each atom was performed via EDX method. In addition to B, N and Cu atoms, the C and O mapping was obtained to confirm the ligand TSC (middle and right). These maps show that all of the constituents of the nanocomposite, i.e. copper

crystals, the filler BNNS and the ligand TSC, are present in the nanocomposite structure. On the other hand, Figure 43 demonstrates the images obtained after polarization, where there is an apparent microstructural change due to application of aerated NaCl solution. The FIB images show higher number of pores after exposure than those before exposure that might be due to disappearance or reorientation of some constituents of the nanocomposite.

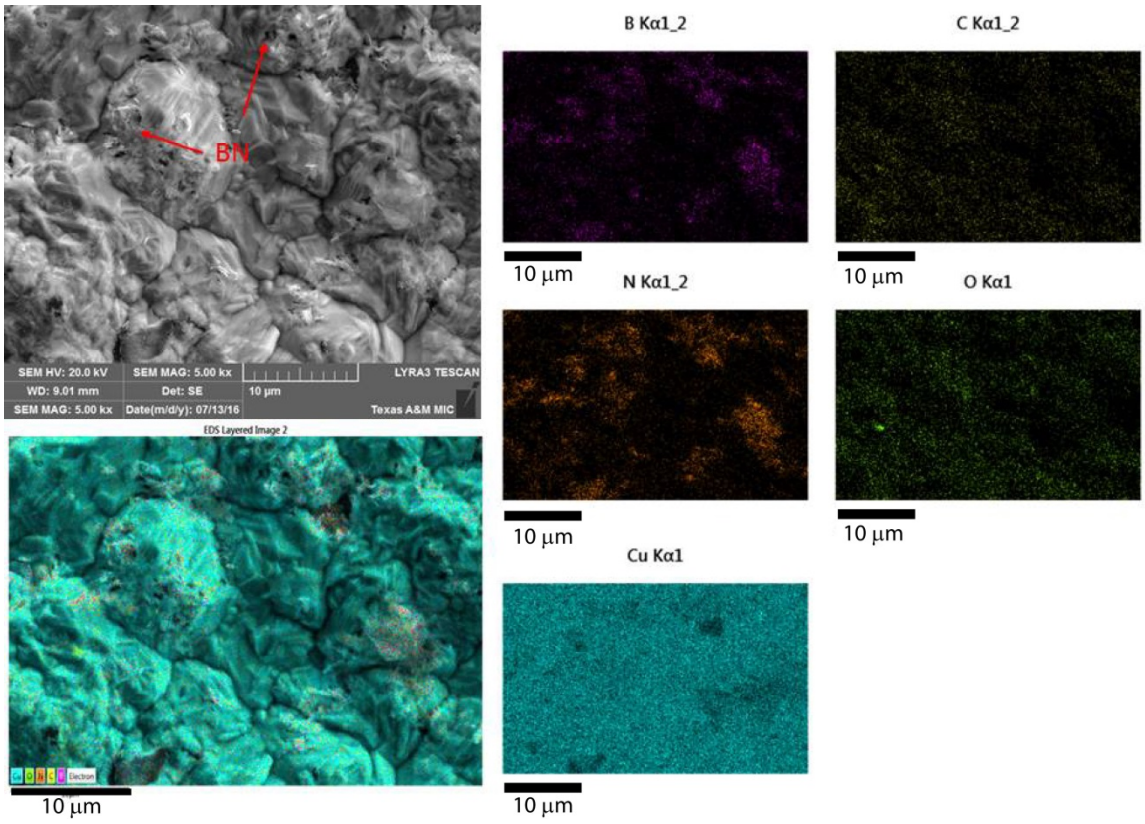

Figure 42. Microstructural analysis before polarization. High resolution FIB microscopy images of Cu/f-BNNS nanocomposite TIMs (left) and EDX mapping of each individual element on these samples (middle and right)

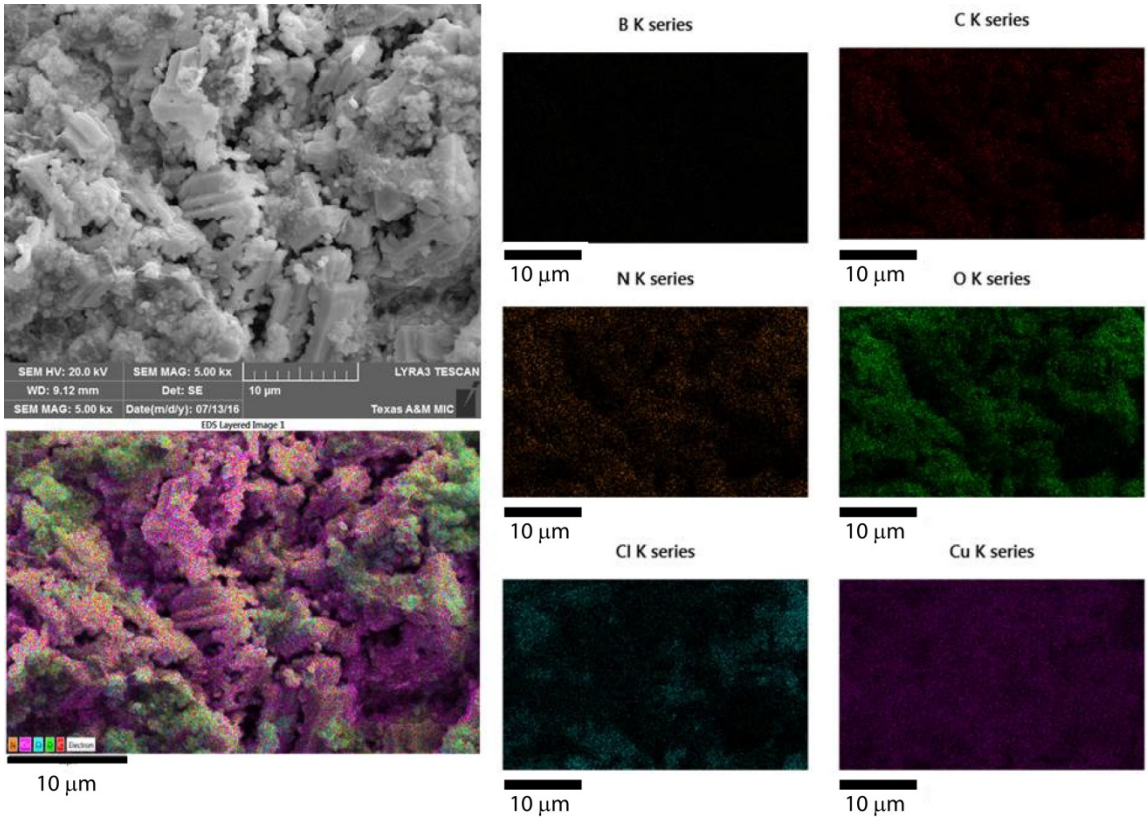

Figure 43. Microstructural analysis after polarization. High resolution FIB microscopy images of Cu/f-BNNS nanocomposite TIMs (left) and EDX mapping of each individual element on these samples (middle and right)

Detailed information on the microstructural changes was attained from the elemental mapping images. Cl atom was added to the elemental mapping to show the effect of NaCl on the sample surfaces. After the polarization the boron atoms could not be detected while other elements maintained their presence on the nanocomposite. The possible reason is that the active sites of TSC bind preferentially with copper complexes during the corrosion process, which later causes leaching of the BNNS into the electrolyte. Since the mapping was obtained within 1-2 µm depth from the surface of the nanocomposite, we can state that the BNNS still remain in the copper matrix at high

concentrations. However, contribution of TSC to the corrosion performance increased at the expense of BNNS.

4.3.4. Conclusions

Electrochemical analysis indicates that the dispersion of f-BNNS in the copper matrix enhanced the corrosion protection of the TIMs. Surface morphology of the pure Cu and nanocomposite samples was evaluated by high resolution microscopy to obtain a fundamental understanding on the behavior of the samples before and after the corrosion tests. It was concluded from the EDX analyses that the strength of the BNNS-TSC interaction was insufficient to hold the BNNS on the nanocomposite surface while a significant percentage of BNNS still remains dispersed in the metal matrix.

5. SILVER BASED TIMS AND THEIR PROPERTIES

The thermal contact resistance, R, is one of the major factors limiting the rate at which heat can be dissipated.[21,22] According to the theoretical models[27,28], the contact conductance, 1/R, can be expressed as:

$$1/R = 1.25k\, m/\sigma * (P/H)^{0.95} \quad (16)$$

where k is the harmonic mean thermal conductivity of the contacting surfaces, m is the effective absolute surface slope, σ is the effective rms roughness, P is the contact pressure, and H is the micro-hardness of the softer material. From a perspective of the material property design, to minimize the thermal contact resistance, as a first approximation, one needs to maximize the ratio of thermal conductivity to hardness. To this end, various strategies have been explored and implemented. For instance, there are numerous publications in the literature reporting the incorporation of fillers with high thermal conductivity such as silver particles, copper particles, graphene, carbon nanotubes, and silicon carbide and diamond powder into a soft, compliant polymer matrix or viscous oil to form thermal interface materials.[214–221] For these types of materials, the current-state-of-art in the ratio of thermal conductivity to hardness lies in the range of 2×10^{-9} to 10×10^{-9} m^2/Ks.

An alternative approach is to rely on a high thermal conductivity matrix such as copper or silver and to improve its compliance by forming porous sponge-like structures[92,222,223] or arrays of nano/micro-pillars,[224,225] which typically have the ratio of thermal conductivity to effective hardness values in range of 5×10^{-8} to 3×10^{-7} m^2/Ks. However, in these cases, the increased surface area tends to result in an increased rate of

oxidation and corrosion. In addition, the surface pores of metal sponge can contribute to the effective roughness, thereby adversely influencing the transport of heat.

In this study, we report a new class of thermal interface material involving metal nanocrystals coordinated with organic ligands grafted on 2D BN nanosheets in the form of mesoscale metal-organic framework. We compare the obtained TIMs properties with the ones obtained using copper as the matrix. Furthermore, this work is concerned with the investigation of how the organic ligand (linker) chemistry influences the thermal and mechanical properties of the resultant material.

Silver is a metal with the second highest k/H (after indium) ratio excluding group I metals, which are highly reactive. Silver also has much higher corrosion resistivity in comparison to indium and copper. Regarding the linker molecules other than TSC, prior studies have revealed that acyl chloride (COCl) groups and amino groups on BN nanomaterials react via nucleophilic addition/elimination with a high reaction yield.[226] In this reaction, after the lone pair on the amino groups of BN performs a nucleophilic attack on the carbonyl carbon, carbonyl group reforms by releasing a chloride ion and the charge neutrality is finally achieved by deprotonation with the aid of the chloride ion. Similar reactions of carbonyl groups are observed with carbon nanotubes[226] and boron nitride nanomaterials[227] as functionalization techniques. Hence, we selected to use three different ligands, 4-bromo-benzoyl chloride (BBC), 4-cyano-benzoyl chloride (CBC) and 2-mercapto-5-benzimidazole carboxylic acid (MBCA), as linker molecules. With this combination, we fixed the reactive group of the ligand that directly binds to the BN nanosheets (forming an amide) while varying the terminal end of the functionalized

nanosheets from bromo- to cyano- to mercapto-group. Mercapto-[228,229] and cyano-group[230] can chemically interact with silver and form coordination or semi-covalent bond while bromo-group is likely to physisorb on the metal surface.

5.1 Materials and Methods

5.2.1 Materials

4-bromo-benzoyl chloride (BBC), 4-cyano-benzoyl chloride (CBC) and 2-mercapto-5-benzimidazole carboxylic acid (MBCA) were obtained from TCI Chemicals (Philadelphia, PA, USA). Ethanol was obtained from VWR (Houston, TX, USA). BNNS was purchased from M.K. Impex Corp (Mississauga, Ontario, Canada). Silver cyanide, AgCN; potassium cyanide, KCN; and potassium dicyanoargenate, $AgK(CN)_2$, which were used in the electrodeposition solution, were obtained from Sigma Aldrich (St. Louis, MO, USA). Other materials were already discussed in earlier chapters.

5.2.2 Functionalization of BNNS

Functionalization of BNNS for all of the ligands was carried out in a similar fashion as described in work done by Zhi et al[227]. Briefly, 1:4 weight ratios of BNNS to ligand were kept in a flask equipped with a condenser. Under a nitrogen environment, reaction contents were constantly stirred using a magnetic stirrer at 120 ^{O}C for 120 hours. After the reaction was completed, the contents were let to cool down to room temperature before washing in excess ethanol to get rid of the unreacted ligand. The washed product was centrifuged at 4000 rpm for 5 minutes and the precipitate was collected under dry nitrogen at 60 ^{O}C overnight.

5.2.3 Characterization of Functionalized Nanosheets

Dried samples were taken directly and measured for FTIR on a Shimadzu IR Prestige ATR-FTIR (Shimadzu Scientific Instruments Inc., Columbia, MD). Data were acquired in the transmission mode with a resolution of 1 cm^{-1} wavenumber and are an average of 12 measurements for each ligand.

5.2.4 Preparation of Thermal Interface Materials

To form mesoscale metal-organic-frameworks, we developed an approach coupling of a coordination-driven assembly and electrodeposition. The key concept is that as silver nanoclusters form and deposit on the cathode through a reduction process, the organic ligands on nanosheet spacers reaches to the vicinity of nanoclusters through diffusion and coordinate their assembly. Electrodeposition bath was made by mixing 5 g of KCN, 3 g of AgCN, and 1 g of $AgK(CN)_2$ in 100 ml Milli-Q water. For the coordination, one of the three struts were used: 4-bromo-benzoyl chloride, 4-cyano-benzoyl chloride, or 2-mercapto-5-benzimidazole carboxylic acid, all of which were grafted on BN nanosheets to provide sufficient space to link relatively large nanoclusters compared to the size of ligands. Depending on the ligand, to achieve a net nanosheet loading of 10±1 wt% in the thermal interface material, 0.5 wt%-1.5 wt% BNNS grafted with ligands were added and sonicated for 30 minutes. A pure silver (>99%) and an aluminum substrate were connected to anode and cathode, respectively. The material was deposited on the aluminum substrate via pulsating electrodeposition using Powerstat05 Potentiostat (Nuvant Systems Inc., Crown Point, IN). The electrodeposition was carried out at a current density of 0 to 12 A/dm^2 and AC frequency of 950 Hz with 30% off time. The resultant TIMs were detached

from the Al substrate, rinsed with water, dried and stored under nitrogen for further characterization.

5.2.5 Chemical characterization of nanocomposite TIMs

The obtained TIMs were cut into small pieces and chemically analyzed using an Omicron XPS/UPS system with an Argus detector relying on dual Mg/Al X-ray source (Scienta Omicron GmbH, Taunusstein, Germany). All spectra were corrected to the reference binding energy of ambient carbon at 283.5 eV.

5.2.6 Thermal characterization of nanocomposite TIMs

A modulated Q20 DSC (TA Instruments, New Castle, DE) was used to measure specific heat capacity of the samples[43]. Thermal diffusivity measurements were performed via a DLF-1200 Laser Flash Diffusivity System (TA Instruments, New Castle, DE)[44]. DLF 1200 uses a laser source with a pulse width of 300 s to 400 s to shoot laser on to a 1 inch circular samples and the measurements were carried at the laser power of 15J - 17J. The density of samples was determined via Archimedes principle. The loading weight and volume fractions were determined gravimetrically.

Thermal interface resistance was measured using phase-sensitive transient thermoreflectance (PSTTR). The nanocomposite was directly electro-co-deposited on to a silicon substrate (25.4 mm in diameter) and sandwiched with another aluminum (Al) bonding layer as adhesive in the middle. Pure aluminum of 4.5 μm thickness was melted on top of a silicon substrate under an argon atmosphere and rapidly transferred on to the TIM surface which was coated on another silicon substrate. The whole configuration was cooled in room temperature to obtain permanently diffusive-bonded samples.

5.2.7 Mechanical characterization of nanocomposite TIMs

Hardness and reduced elastic modulus values were measured via a Hysitron TI 950 Triboindenter (Hysitron Inc., Minneapolis, MN). A Berkovich tip with a well-defined geometry was used for indentation and forty measurements were taken from each sample for statistical analysis. For each measurement, a force of 5000 mN was applied over 10 seconds, and the tip was withdrawn from the surface for 10 seconds with a 5-second holding time in between. The force versus depth curves were fitted to give the values of reduced modulus and hardness.

5.2 Result and Discussion

Table 12 Property comparison for silver based and copper based TIMs involving TSC as ligand at 10 wt% loading

Material	Thermal Conductivity (W/m/K)	Hardness (GPa)	Elastic Modulus (GPa)	Contact resistance (mm^2.K/W)	Overall Resistance at BLT 30 μm
Pure copper	375 ± 10	1.62 ± 0.3	70 ± 10	0.15 ± 0.03	0.38 ± 0.05
Copper TIM	220 ± 12	0.41 ± 0.1	25 ± 4	0.10 ± 0.02	0.38 ± 0.06
Pure Silver	390 ± 5	1.24 ± 0.2	80 ± 4	0.12 ± 0.3	0.31 ± 0.04
Silver TIM	290 ± 15	0.23 ± 0.06	30 ± 5	0.07 ± 0.3	0.24 ± 0.03

First, the properties of the silver TIMs are compared against copper TIMs which are prepared involving TSC as the organic linker and are given in Table 12. It is understood that even though the silver TIMs showed higher thermal properties, clearly they were not able to mimic the mechanical properties of the copper TIMs. But due to the synergistic effect of the high thermal conductivity and reasonable mechanical properties silver TIMs show lower thermal resistances. These comparison of values are given in the table 13.

Via nucleophilic substitution reaction, boron nitride nanosheets were functionalized with either of three different bifunctional ligands (linkers), which involves a carboxylic terminal-end reactive toward BNNS, a benzene ring (an organic spacer section), and another terminal-end with varying affinity towards silver surfaces (Figure 44).

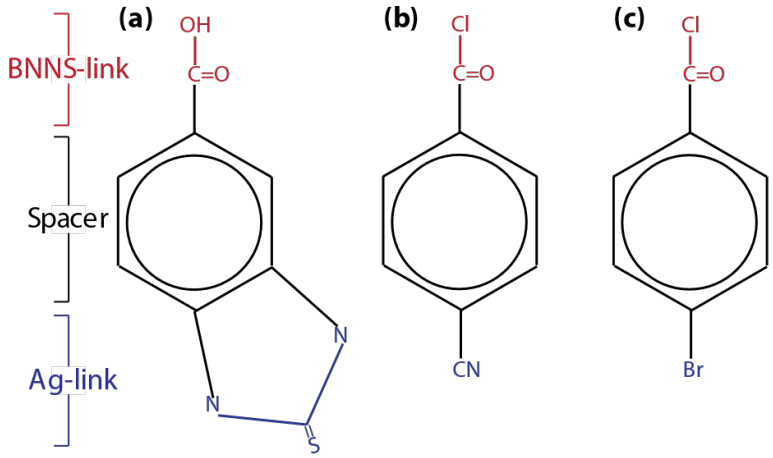

Figure 44 Generic structure of a selected ligand. Structures of the specific ligands are a) 2-mercapto-5-benzimidazole carboxylic acid (MBCA), b) 4-cyano- benzoyl chloride (CBC), and c) 4-bromo-benzoyl chloride (BBC).

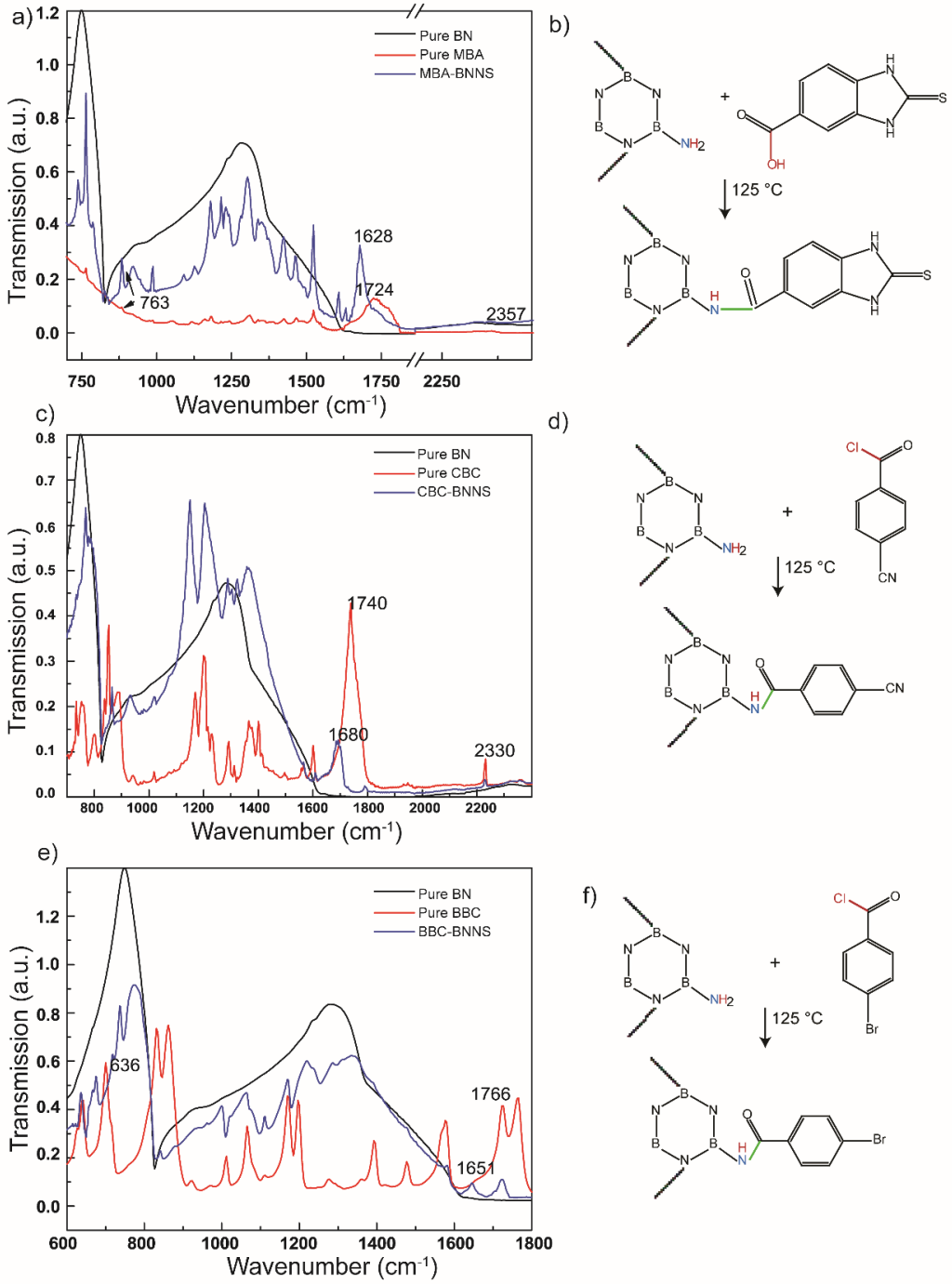

Figure 45 a) FTIR spectra for pure BNNS, pure MBA and MBA-BNNS b) reaction scheme for reaction of MBA and BNNS to form MBCA-BNNS c) FTIR spectra for pure BNNS, pure CBC and CBC-BNNS d) reaction scheme for reaction of CBC and BNNS to form CBC-BNNS e) FTIR spectra for pure BNNS, pure BBC and CBC-BNNS f) reaction scheme for reaction of BBC and BNNS to form BBC-BNNS

The functionalization reactions were characterized with FTIR spectroscopy. Figure 45a shows the FTIR spectra of pure BNNS, pure MBCA, and MBCA-BNNS where the most notable change was the shift of the peak from 1724 cm^{-1} to 1628 cm^{-1}. This shift indicates a different level of coupling between the carbonyl group and the molecular group next to it: a change from carboxylic acid to amide. In addition, no shift in peaks at 763 cm^{-1} and 2357 cm^{-1} indicates that C=S (thio urea) and SH (thiolate form) terminal-edges did not react with BNNS and faced away from BNNS surfaces. Based on these observations, a condensation reaction is proposed as illustrated in Figure 45b. Figure 45c displays the FTIR spectrum for pure CBC and CBC-functionalized BNNS in which the shift of peak from 1740 cm^{-1} to 1680 cm^{-1} in comparison of pure CBC to CBC-BNNS suggests that the reaction occurred at carbonyl group changing carbonyl chloride into amide. In addition, the peak corresponding to cyano group is unchanged at 2330 cm^{-1} suggesting reaction with BNNS from cyano terminal-edge (Figure 45d). Similarly, for BBC, the peak at 1766 cm^{-1} shifts to 1651 cm^{-1} indicating the conversion of carbonyl chloride in pure BBC to amide of BBC-BNNS (Figure 45e). Likewise, the unchanged peak at 636 cm^{-1} corresponding to C-Br suggests no vibrational coupling between Br and BNNS. Overall, all the linker molecules formed an amide upon reacting with BNNS but possessed mercapto, cyano, and bromo groups facing away from BNNS surfaces, which can interact with metal surfaces at varying binding strengths.

Four different nanocomposites were prepared: silver matrix with bare BNNS, with BBC-BNNS, with CBC-BNNS, and with MBCA-BNNS. The resultant TIMs were analyzed using XPS spectroscopy (Figure 46), which revealed that MBA- and CBC-

modified BNNS interact chemically with silver, whereas no chemical interaction is observed with bare BNNS or BBC-BNNS as evidenced by positive 0.3 eV shifts in silver $3d_{5/2}$ peak for silver-CBC-BNNS and silver-MBCA-BNNS nanocomposites.

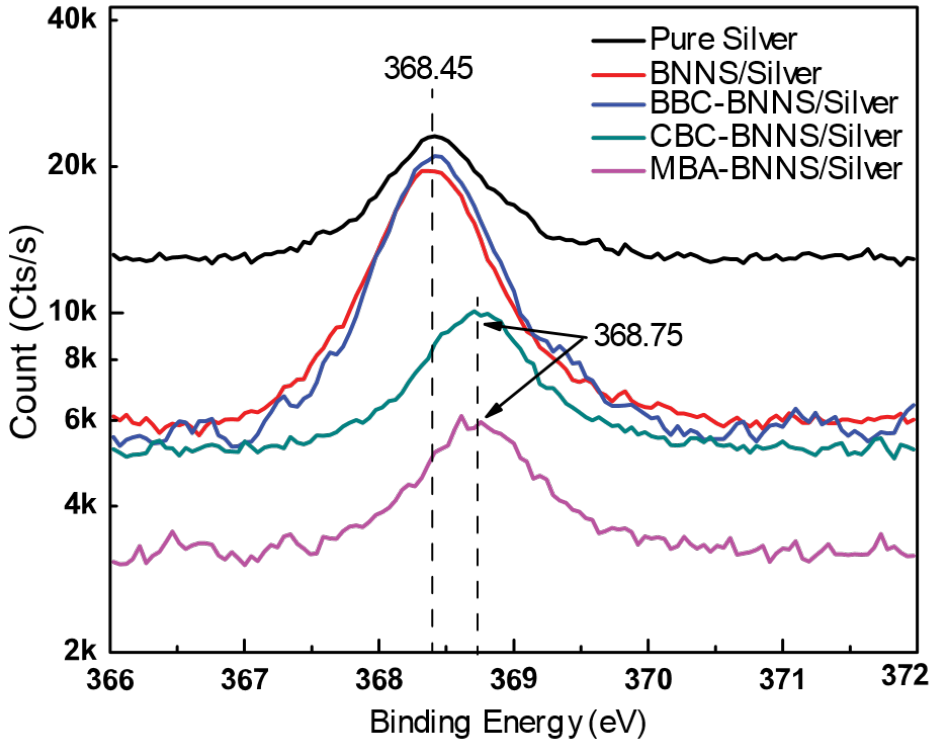

Figure 46 High resolution silver (Ag) X-ray Photo Spectrometry Spectra of different nano-composites. Nanocomposites involving pure BNNS and BBC-BNNS do not show any change in silvers oxidation state but the nanocomposites involving CBC-BNNS and MBA-BNNS show an oxidative shift of 0.3 eV suggesting the chemical integration of filler system in to the metal matrix.

These shifts can presumably be ascribed to the coordination bond between cyano and thiol groups causing silver to assume a slight positive charge due to electron donation, whereas the groups themselves take on a slight negative charge.

Upon confirming the chemical reactions, morphological (nanostructure), thermal and mechanical properties were investigated. Fracture SEM studies revealed that the filler surface chemistry has a pronounced effect on the internal nanostructure of the resultant nanocomposite TIM (Figure 47). Bare BNNS and BBC-functionalized BNNS were trapped in the grain boundaries of silver crystals in aggregated chunks indicating no favorable chemical integration of the fillers into the silver matrix (Figure 47 b&c).

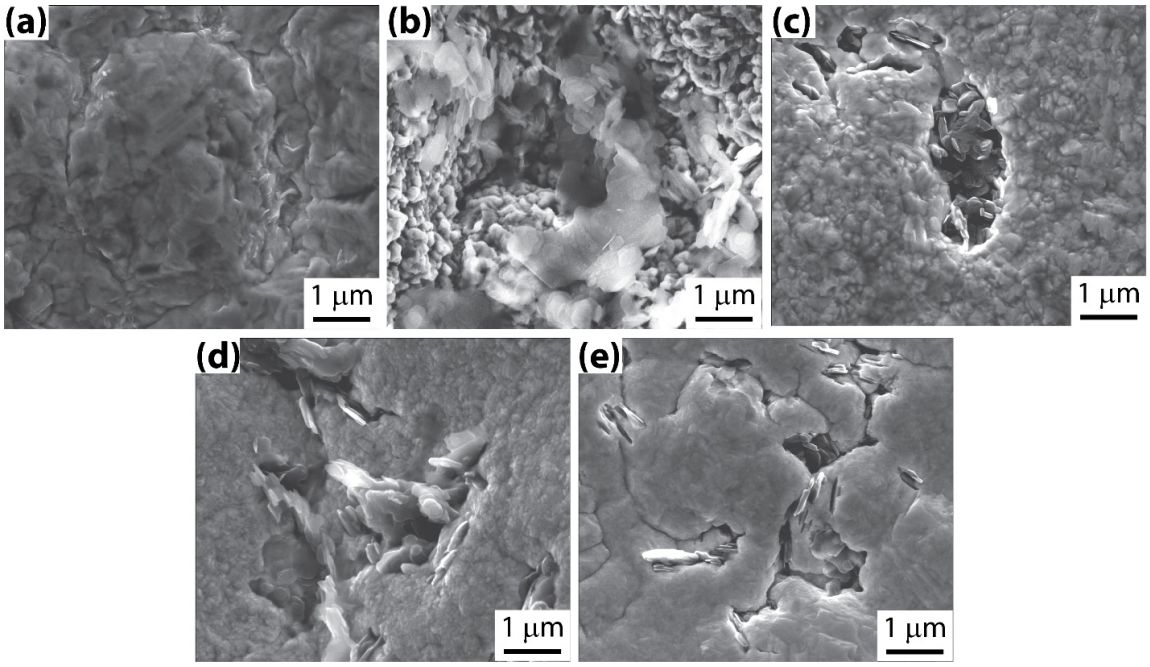

Figure 47 Secondary electron micrographs of. (a) pure silver and nanocomposites involving (b) pure BNNS, (c) BBC-BNNS, (d) CBC-BNNS, and (e) MBA- BNNS. Here, (b) and (c) clearly show the physical entrapment of the fillers due to the lack of chemical interaction ability but (d) and (e) show the integration of f-BNNS which can chemically interact in to the metal matrix.

On the other hand, CBC-functionalized BNNS and MBCA-functionalized BNNS gave rise to more intricate bonding between fillers and silver grains with significantly reduced aggregation (Figure 47 d&e). These observations are consistent with the abovementioned chemical interactions studies using XPS. The presence and nature of organic linker influenced the thermal conductivity of nanocomposite TIMs (Figure 48a). For a fixed filler volume fraction of 10±1 wt%, the effective thermal conductivity of nanocomposites involving fillers functionalized with linkers having high affinity towards silver (i.e. CBC-BNNS and MBCA-BNNS) was about 25-40% higher than that with the BBC-BNNS having low affinity towards silver (BBC-BNNS). The presence of BNNS with or without functionalization resulted in about 15% reduction in the effective thermal conductivity compared to pure silver, which can be attributed to the relatively low thermal conductivity of organic linkers or the out-of-plane thermal conductivity of BNNS being lower than that of pure silver. The difference in thermal conductivity of nanocomposites with physisorbed and chemisorbed linkers between BNNS and silver may be ascribed to following: For the case of chemisorption, because the chemical functionalization occurs at the edges of BNNS[231], the phonons transferred from metal will be forced to travel in the in-plane direction of BNNS, which is the direction with ultrahigh thermal conductivity. For the case of physisorption, the linker molecules randomly adsorb on BNNS surfaces. As such, the phonons coming from metal side and travelling through linkers will pass through BNNS in random orientations, thereby increasing the effective contribution of out-plane thermal conductivity of BNNS, which is much smaller than in-plane thermal conductivity of BNNS. Furthermore, upon the introduction of f-BNNS, some of electronic

contribution of thermal transport is replaced by phononic contribution. Since the binding strength determines the anharmonic electron-phonon coupling,[180,181,232,233] physical bonds will result in a larger bottleneck for thermal transport across a metal-organic-inorganic interface.

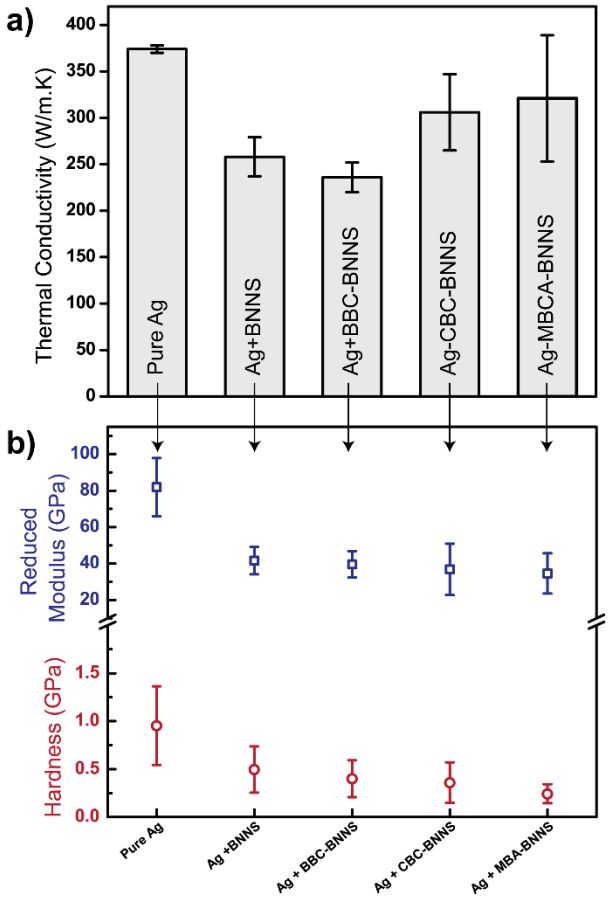

Figure 48 a) Thermal conductivity of the fabricated nanocomposites. b) Reduced modulus and hardness values of the fabricated nanocomposites. Both properties are also compared against pure silver, pure copper and previously fabricated copper nanocomposites. Overall, , composite involving MBA-BNNS show 75% reduction in hardness but retain 85% of thermal properties which makes it a very promising TIM.

Figure 48b presents the reduced modulus and hardness of these nanocomposites obtained using nanoindentation. Silver-based nanocomposites were found to be softer and more compliant than pure silver. This trend is presumably because the presence of BNNS disrupts metallic bonds between silver crystals within the film and in addition, will reduce the van der Waals interactions between silver crystals considering that the dielectric constant of metals is much higher than that of inorganic and organic materials. In addition, the occupation of the f-BNNS at grain boundaries increases the fraction of atoms each grain interacts with and results in a larger atomic plane sliding which softens the nanocomposite[234].

Furthermore, the ligand molecules act as cushions due to their inherent softness. The hardness and modulus values were lower for chemically integrated nanocomposites in comparison to physically integrated nanocomposites, which is counter-intuitive considering only the types and strengths of the bonds involved. However, physically integrated nanocomposites experience the aggregation of fillers as shown in Figure 4. Hence, for a given nominal filler loading, the effective filler concentration is reduced at an aggregated state considering the aggregates of filler as a new filler with much larger size. Assuming the mechanical properties of fillers do not change significantly with aggregation, the effective medium theory[185,186] can explain the observed trends.

Based on the measured thermomechanical properties, the k/H ratio for these silver-based nanocomposites is calculated to be 1.3×10^{-6} m^2/Ks for the case of MBCA-BNNS fillers and 8.5×10^{-7} m^2/Ks for the case of CBC-BNNS fillers. Considering pure silver samples prepared had a k/H ratio of 3.9×10^{-7} m^2/Ks, these values signify noticeable

improvements in thermomechanical properties of chemically-integrated nanocomposites. On the other hand, the physically-integrated nanocomposites lead to lower k/H ratios, in the range of 5.2×10^{-7}-5.9×10^{-7} m^2/Ks, compared to the chemically integrated ones. Using PSTTR technique, a thermal interface resistance of 0.05±0.02 mm^2.K/W and 0.06±0.02 mm^2.K/W was measured at Si-TIM interface under adhesive loading for nanocomposites with chemisorbed and physisorbed fillers, respectively in comparison to 0.12±0.03 mm^2.K/W for the case of pure silver.

5.3 Conclusion

Overall, this work has three key conclusions, important in the context of materials science and thermal management. First, using coordination chemistry in conjunction with electrodeposition, it is possible to fabricate mesoscale metal-organic frameworks involving a silver matrix, 2-D BN nanosheets, and organic linkers. Second, nanostructure, thermal and mechanical properties of these hybrid nanocomposites strongly depend on the chemistry of linker molecules physically or chemically binding nanosheets to the silver matrix. BN nanosheets with cyano- and thio- terminal group incorporate into the grains of silver and show higher thermal transport than physically adsorbed composites, in addition to having softer matrices. Third, silver-based chemically-integrated nanocomposites advance the current-state-art in the thermal interface materials owing to their very high thermal conductivity-to-hardness ratio, in the order of $1.3\text{x}10^{-6}$ to $8.5\text{x}10^{-7}$ m^2/Ks. With such intriguing thermal and mechanical properties and scalable methodology of production, these materials can be applied in various thermal management systems to relieve the thermal stresses in next generation devices and applications.

6. NANOCOMPOSITE OF POLYSTANNANE AND GRAPHENE AS TIM

6.1 Materials and Methods

6.1.1 Materials

Dibutyltin dichloride (DBDC) (Bu_2SnCl_2, >97% (T)), tetra butyl ammonium perchlorate (TBAP) ($C_{16}H_{36}ClNO_4$, >97% (T)), 1,2-dimethoxy ethane (DME) ($C_4H_{10}O_2$, >99.0% (GC)), Toluene (C_7H_8, >99.5% (GC)), Methanol (CH_4O, >99.8% (GC)), ethyl acetate ($C_4H_8O_2$, >99.5% (GC)), tetrahedrofuran anhydrous (C_4H_8O, >99.5% (GC)) and Pentane (C_5H_{12}, >99.0% (GC)) were obtained from TCI America (Portland, OR). Silver wire of 24 gauge was obtained from fdj tool company (Winter park, FL) and the 304 stainless steel wire of 20 gauge was obtained from McMaster Carr (Elmhurst, IL). Graphene nano powder of 3-7 layers was obtained from graphene supermarket (Calverton, NY).

6.1.2 Polystannane synthesis

The reaction was achieved via electro polymerization as reported by previously[170] with few changes. The biggest change is the electrode material, stainless steel was used as a cathode and silver as anode. Reaction was performed in nitrogen atmosphere and extreme caution was employed to avoid contact with air. Briefly, 2 gm of TBAP was precipitated in pentane and ethyl acetate (50-50) solution and kept under reduced pressure for 6 hours before introducing into a three necked flask (electrochemical cell) with 30 ml of DME and nitrogen environment. 0.6 grams of DBDC was dissolved in pentane and recovered at -80 ^{O}C. The purified DBDC is left under reduced pressure overnight and then transferred into the electrochemical cell. The three necks of the cell are closed with rubber

corks through which electrodes (silver and steel) run out to connect to Nuvant Powerstat05 Potentiostat (Nuvant Systems Inc., Crown Point, IN). The length of the silver electrode (cathode) is kept 2 times of the steel electrode (anode). A constant 9 V current is applied until 95% of the predetermined stoichiometric electron charge is transferred in to the cell. All time through the reaction, the cell is covered to make sure no light can interact with the produced polymer. Also, the contents of the cell are constantly stirred using a magnetic stirrer. All of the cell is now kept under reduced pressure until all solvent is evaporated and the precipitate is dissolved in 50 ml of methanol where the polymer precipitated while the TBAP dissolved. The precipitated polymer was dissolved in toluene before dissolving in 50 ml of methanol again to get rid of all possible TBAP. This process is repeated 3 times and the final precipitate is stored under dry nitrogen environment.

6.1.3 Nanocomposite synthesis

Predetermined graphene is dissolved in 20 ml toluene and sonicated using a SYCLON ultrasonic cell crusher (Syclon Electr. Instr. Comp., Zhejiang, China) for 60 minutes at 40% power. Now the polymer is introduced in to the solution and shaken vigorously on a vortex for 5 minutes. Toluene is evaporated under reduced pressure and the obtained nanocomposite is stored under dry nitrogen.

6.1.4 Characterization

DSC

Polymer sample of 3-6 mg is put in to a TZero aluminum pans and then loaded on to a modulated auto Q20 DSC (TA Instruments, New Castle, DE) with a liquid nitrogen cooling cell. The sample is cooled to -70 ^{O}C at 10 ^{O}C/min rate and kept isothermal for 5

minutes without recording any data. The sample is now ramped up to 70 ^{O}C at the rate of 5 ^{O}C/min and back to -70 ^{O}C while recording all the data.

UV-Vis

A baseline is made with pentane in both quartz cuvettes on a UV-1800 spectrophotometer (Shimadzu, Columbia, MD). The polymer sample was dissolved in pentane and loaded to measure the peaks from 500 nm to 250 nm with a 1 nm resolution and average of 8 times.

6.1.5 Thermal characterization

The DSC experiments were used to calculate the specific heat capacity and then the sample is drop casted on to a ½ inch diameter copper plate which is 100 microns thick until the thickness of the sample is 0.5 mm. This sample is loaded in to the furnace of DLF-1200 laser flash diffusivity system (TA Instruments, New Castle, DE) and thermal diffusivity is measured at room temperature with an average of 3 shots. Also, the density of the samples is measured gravimetrically which was discussed in chapter 3. Also, thermal conductivity was calculated as explained in chapter 3 by using the above 3 measured values.

6.1.6 Stability experiments

UV-Vis spectrophotometer was used to establish a concentration vs absorbance curve for polystannate in pentane and on quartz glass. These graphs are later used to determine the unknown concentration of the polymer in the samples from the measured absorbance values.

Light stability

A light source of 100 W is used to expose the samples for specific time before the concentration of the polymer is measured in UV-Vis spectrophotometer.

Humidity stability

A humidity box is created by placing a bath of sodium chloride in a closed dark acrylic box. The concentration of NaCl solution is maintained to obtain 75% relative humidity and the bath is left in the box for an hour to reach the steady state. Now, samples are exposed to moisture in this box for required amount of time before measuring the concentration using UV-Vis spectrophotometer.

6.2 Results and Discussion

Polystannane under consideration in this paper is synthesized using dibutylstannane as the monomer. The reaction was achieved via electro polymerization as reported by previously [170] with few changes. The biggest change is the electrode material, stainless steel was used as a cathode and silver as anode. Reaction was performed in nitrogen atmosphere and extreme caution was employed to avoid contact with air. Figure 49a shows the scheme of polymerization reaction, where electrons passing through the electrolyte solution convert the monomers in to polymers. Figure 49b shows the physical sample of the polymer which is light yellowish in color.

The UV-Vis analysis as showed in Figure 49c, displayed a maximum peak at 378 nm confirming the presence of polystannane[168,171]. In addition, no peak in the 320-360 region suggests that the polymer is free of oligomers which have peaks in this region[235].

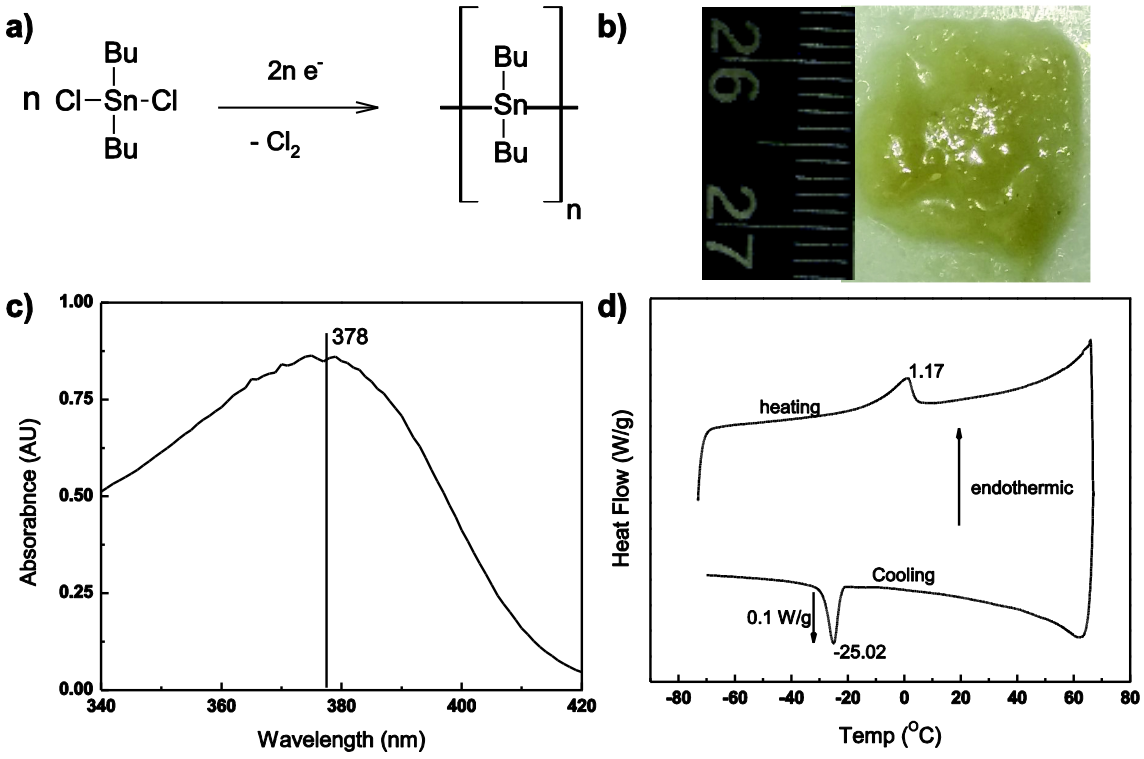

Figure 49 a) Schematic for the polymerization reaction from the monomer. b) Photographic image of the polymer obtained against a scale denoted in centimeters. The polymer is light yellow color and can be drop casted to form specific shapes needed. c) Uv-Vis spectrograph of the polymer in pentane showing a peak at 378 nm, which indicates the presence of the polystannate polymer. d) DSC heating and cooling cycles of the polymer showing a endothermic phase transition at 1.17 ^{o}C and an exothermic transition at -25.02^{O}C.

Figure 49d shows that the polymer has given a endothermic phase shift at 1.17 ^{o}C and an exothermic phase shift at -25.3 ^{o}C during heating and cooling cycles in DSC respectively. These peaks suggest the sub-ambient phase shift observed in the Polystannane. From the previous studies, it is concluded that the polymer exists at a liquid crystalline like mesophase where the chains are hexagonally packed with a disordered backbone[168,172,236]. Further analysis of the PolySn with GPC suggested that the synthesized

polystannate had an approximate molecular weight of 25-30 kg/mol. This comprises of 90-130 monomer units forming a long Sn-Sn chain link.

This long chain Sn-Sn link can participate in σ-σ coupling of electrons and present a new dimension of electron transport in the polymer. These orbitals overlap and split in to valence and conduction band. The band gap here is expected to be narrower than the silane and germane polymers and is in the range of 2.7-3.2 eV as reported[235,237–239]. At elevated temperatures this bandgap can reduce giving rise to more transport of electrons and thus conduct more heat as well. But, the phase change can affect several properties; especially the transport properties due to change in orientations and organization of molecules in each phase. Since, we are interested in application of these materials in daily life; we further discuss only the properties in mesophase (liquid –crystalline) which is observed above 0 ^{o}C.

GNPs are reported widely to improve transport properties of the bulk materials and here we prepare composites of PolySn with GNP. The GNP we used were 3-10 layers thick and up to 2 microns in lateral dimensions as reported by the manufacturer. To prepare the composites, keeping graphene percolation point in view for several materials, which is in range of 0.1-1 wt%. We varied the GNP concentration from 0.1 – 10 wt%. These nanocomposites are further dried in dark conditions after drop casting on to a plate resulting in free standing nanocomposite films. Figure 4b shows the images of the film at 10 wt% GNP loading. Several properties of nanocomposites were tested and the results are as follows.

Mechanical properties are very important for a polymer to evaluate if it is visco elastic or elastic. As reported earlier these are visco-elastic materials which can be confirmed via rheometer as shown in Figure 50. With the increase in concentration of GNP the visco-elastic behavior doesn't show any change. Also, no apparent change in mechanical strength is observed with addition of GNP. It's evident that PolySn is stronger than similar molecular weight organic polymers which exhibit visco-elastic nature.

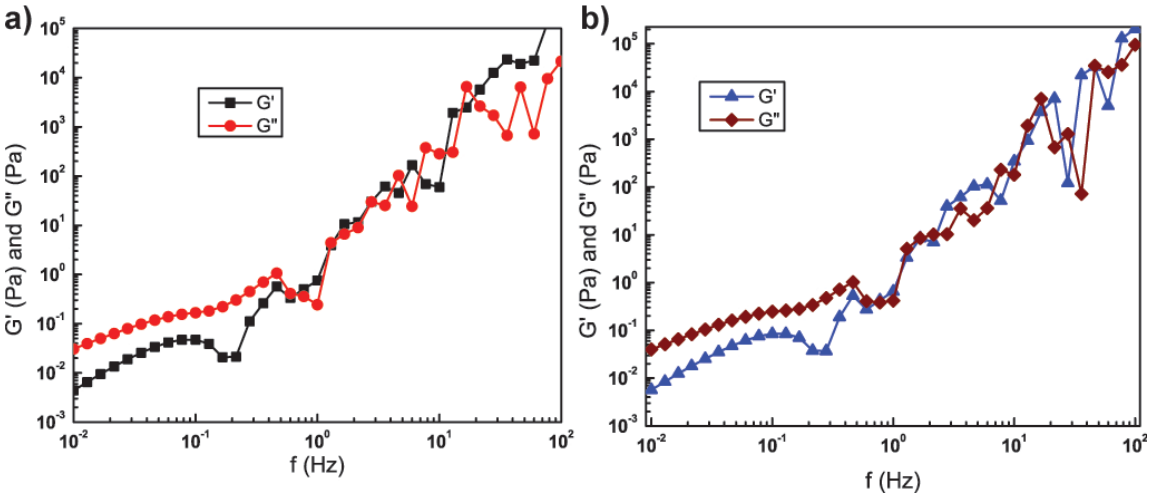

Figure 50 a) Rheometric data for the polymer showing viscoelastic behavior. b) Rheometric data for the 10 wt% GNP loaded polymer showing almost the same behavior in terms of viscoelasticity.

This is expected due to stronger interactions of molecules due to delocalization of σ electrons via Sn-Sn backbone. In the initial stages of GNP addition, the π electron clouds of the GNP can interact with delocalized σ electrons of the Sn back bone resulting in more intricate mechanical structure. Now, the different components of the nanocomposite are interacting via stronger than Vander Walls forces. This interaction increases the overall

mechanical strength. But, it also hinders the polymer-polymer interactions which might reduce the cohesive strength of the material. With these two competing effects, a balance is struck with in the examined range of GNP concentrations and hence no apparent mechanical change is observed.

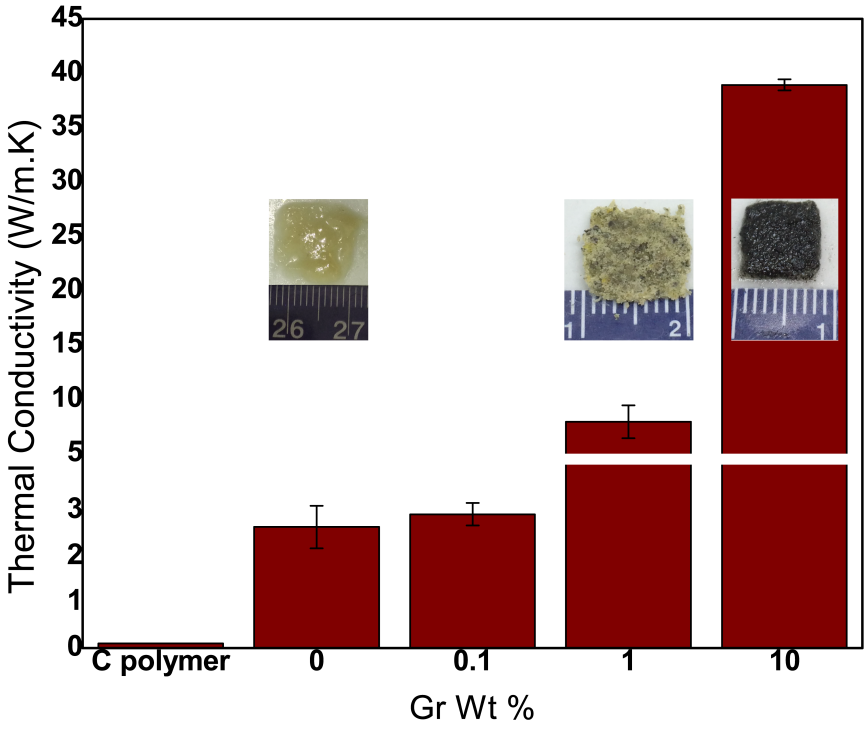

Figure 51 Graph showing the thermal conductivity as measured by the DLF and DSC for the pure polymer and the other polymeric nanocomposites. The thermal conductivity of the nanocomposites is compared against a carbon polymer of similar molecular weight. It is clear that the nanocomposites are highly thermally conductive and thermal conductivity increases with addition of GNP. Also, on top of each bar, the image of the nanocomposite is shown against a scale in centimeters.

The films are used to measure thermal conductivity using DLF system. Data obtained from DSC measurements is used to calculate the specific heat. Ploys has a thermal conductivity of 2.5 W/m.K which is way higher than any other polymeric material which typically have a thermal conductivity less than 0.1 W/m.K[240]. To our knowledge, this is the first report of the thermal properties of PolySn.

Figure 51 shows the thermal conductivity of all nanocomposites. It is observed that the thermal conductivity increases with concentration. GNP-PolySn interactions result in π-σ electron interaction as mentioned earlier. In PolySn; the delocalization results in mixing of σ orbitals and split in to highest occupied valence band (HOVB) and lowest unoccupied conduction band (LUCB). HOVB is formed by ppσ of Sn-$5P_y$ atomic orbitals (AO) and LUCB is comprised of ppσ* Sn-$5P_y$ AOs. Since there is a definite band gap for these hybrid orbitals, finite transport is observed. With introduction of GNPs, these hybrid orbitals interact with π electron stacks of GNPs. This interaction increases the strength of ppπ* and ppπ of Sn-$5P_y$ AOs resulting in destabilization of HOVB and stabilization of LUCB respectively[237,238,241]. The above interaction eventually leads to lower the band gap between HOVB and LUCB of the material. The introduction of more GNPs results in lowering of the band gap and thus increasing the transport. The electrons in valence bond now move to conduction band more easily. This facilitates the electronic heat transport across the material. This is because higher transport GNPs are mixing with lower transport polymer molecules and hence the band gap of the composite will be observed at lower energy level than the polymer itself. But as we know GNPs are excellent conductors of heat via phonons[94,242] and thus introduce extra phononic bandwidth for heat conduction.

Once, GNPs cross certain concentration, more of GNP-GNP interactions also occur which will conduct better than PolySn-GNP interface.

The thermal transport is not only due to electron transport but also due to phononic vibrations. GNPs have high intrinsic thermal conductivity due to high phonon mobility. This property of GNPs paves super shortcuts for phonons in the matrix at several junctions. It improves the phononic transport and hence improves the heat transfer. Introduction of GNPs also result in electron-phonon coupling at the GNP-GNP and GNP-PolySn interfaces resulting in boosting the thermal properties. The coupling facilitates phononic and electronic progression by reducing the interface scattering across polymeric molecules.

We also tested the stability of the nanocomposites against moisture and light since the polymer is unstable with these two entities. Moisture and light cause to destabilize the PolySn and degrade. Preparing nanocomposites of GNP and PolySn will improve the stability of the material. GNPs being hydrophobic inherently can repel water vapor from some regions, forcing the water vapor to take different route than direct transport to molecules within the matrix. This will change the transport behavior of the water vapor with in the matrix which will make the availability of water vapor a critical factor and hence making the polymer more stable. The Pure polymer and 10wt% Gr nanocomposite were exposed to 75% RH created by NaCl in a closed dark box. UV-Vis analysis is performed on these samples and the intensity of the peak at 379 nm is noted. We see diminishing peak for the pure polymer. In fact, the degradation followed a near first order kinetics. The rate constant was 0.0014 s^{-1} with half-life of 495 sec. But with the

introduction of GNP, the composite was much stable than the pure polymer as shown in Figure 52b where the rate constant changed to 0.0005 s^{-1} and half life of 1386 seconds. After exposing for even 1 hour, a small quantity of the polymer was left without degradation owing to the 3 time improvement in the stability.

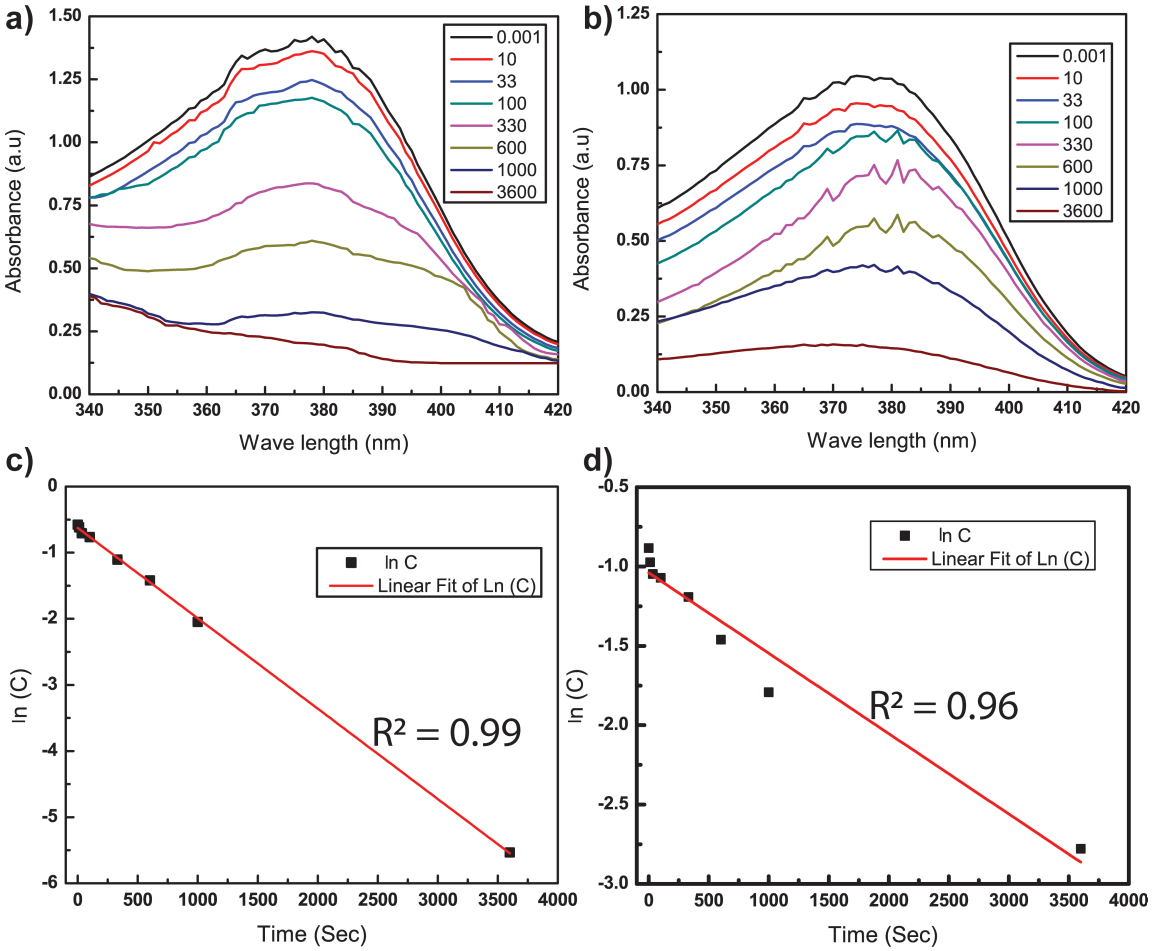

Figure 52 Stability of the polymer is studied against water vapor by exposing to saturated NaCl solution in a closed environment. UV-Vis data is provided at different time points of the exposed polymer and nanocomposite a) UV-Vis data for the pure polymer b) UV-Vis data for the 10 wt% GNP loaded nanocomposite c) First order kinetics fit for the degradation of the pure polymer d) first order kinetics fit for the degradation of the nanocomposite

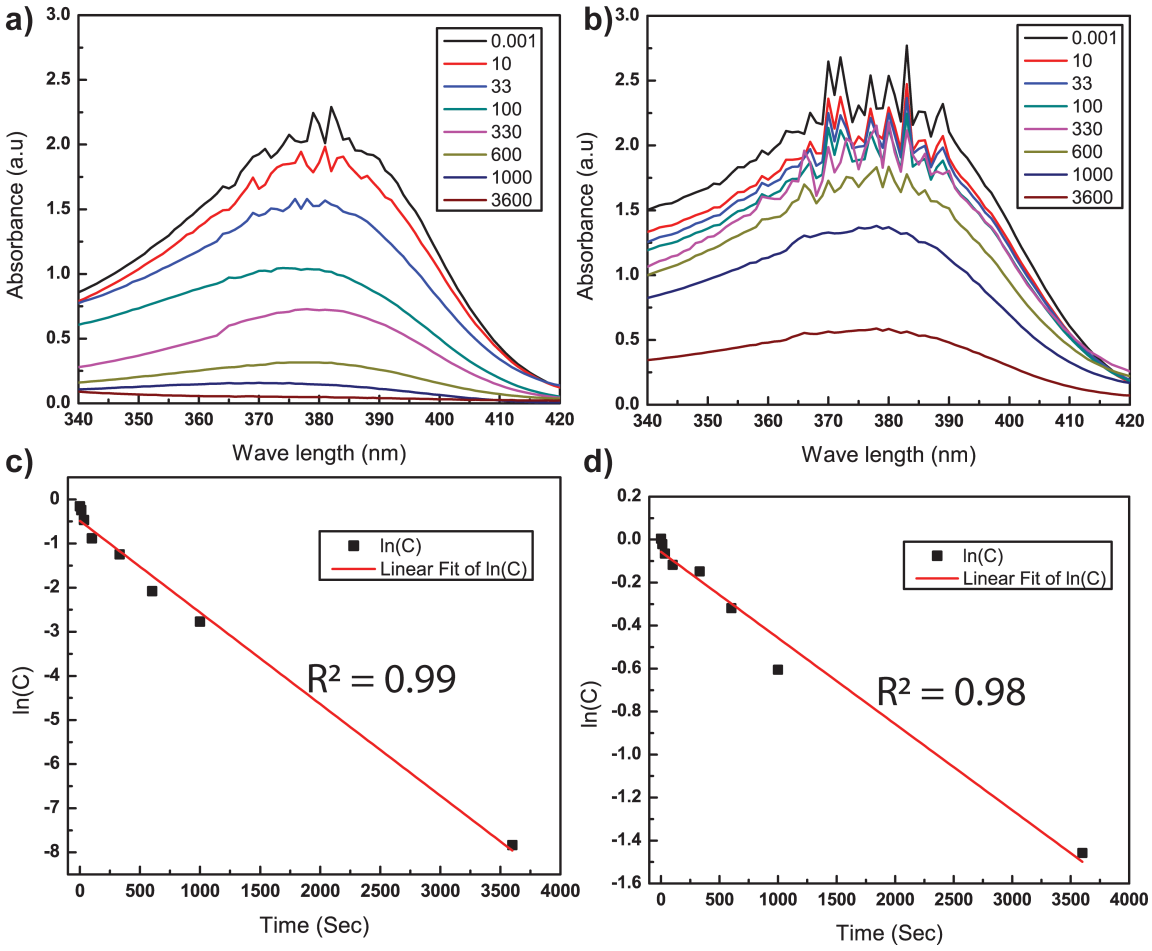

Figure 53 Stability of the polymer is studied against light by exposing to controlled light in a closed environment. UV-Vis data is provided at different time points of the exposed polymer and nanocomposite a) UV-Vis data for the pure polymer b) UV-Vis data for the 10 wt% GNP loaded nanocomposite c) First order kinetics fit for the degradation of the pure polymer d) First order kinetics fit for the degradation of the nanocomposite

More importantly, the kinetics still followed the first order reaction. This is in coherence with the expectation that GNP will change the transport profile within the matrix. In pure polymer, there was no hindrance for the water vapor to go through compared to nanocomposite and hence making it abundantly available makes the polymer a limiting reagent and thus the rate depends up on the polymer itself.

But, within the nanocomposite, the GNPs make the water vapor a non-abundant quantity. This results in the reaction slowing down with water vapor. With these results, we could say that preparing higher GNP loading nanocomposites might further boost the stability of the PolySn towards humidity.

We expect the GNP to improve the light stability of the polymer as well. This is because GNP can absorb most of the light and block the light from interacting with polymeric chains. Exposing pure polymer and 10 wt% GNP loaded polymer to light at 400-700 nm wavelength and 100 watts and measuring the UV-Vis of these samples periodically can give the stability profile. As shown in Figure 53a, the polymer degraded much faster with light than humidity and followed a similar first order kinetics with a rate constant of 0.0021 s^{-1} (Figure 53c), which is almost double the degradation speed compared to humidity at RH 75%. This trend of decomposition also agrees fairly with the literature[168,178,179]. As expected the resistance to light has improved as shown in Figure 54b. Analyzing these results as shown in Figure 53d, the improvement was drastic. Though the kinetics still followed first order, the rate constant was 5 times lower at 0.0004 s^{-1}. This corresponds to a change of half life from 330 seconds to 1730 seconds. This is a very good achievement in terms of boosting the stability of the PolySn. This opens up the possibilities of using the novel properties of the polymer in daily life.

Developing PolySn with different starting monomer units which have conjugation can have much higher thermal transport values than the reported value and they are worth exploring. It is important to note that all these properties are for mesophase (liquid-crystalline). In different phases, the electronic interactions might change due to the

changes in molecular interactions, orientation and arrangement of molecules. Thus, different phases may have different properties since the properties are dependent on molecular and electronic interactions. Also, it's worth noticing that these properties are for a drop casted material and several groups proved that the PolySn can be oriented polymer under certain casting methods and the oriented polymer matrices might show different properties[241,243].

6.3 Conclusion

Overall, we have successfully synthesized PolySn by following previous methods and also were able to prepare homogenous nanocomposites of the polymer with GNP. We also report the thermal conductivity of the polymer as 2.4 W/m.K, a first report and further showed that the thermal conductivity can be boosted up to 40 W/m.K by preparing GNP nanocomposites. The nanocomposites were promising not only in the terms of thermal transport but also showed improved stability towards light and humidity. This study opens up a path for applications wanting to make use of the novel properties of the polymer in daily life which was difficult till now due to the degradation of the polymer caused by humidity and light exposure.

7. SUMMARY AND FUTURE SCOPE

7.1 Summary

Chapter 1, the specific objectives of the work were discussed along with the motivation. Definition of the Thermal interface materials was given along with the need and the importance of TIMs. Also, the importance of developing next generation TIMs was discussed.

Chapter 2, literature review of different TIMs was given where the conclusion was most current TIMs do not match up to the industry requirements for next decade to come. Later on, approach to create new TIMs which can further the current technology was discussed. Further, required basics about BNNS, graphene, electrodeposition and polystannane were discussed which would help better understand of the chapters 3-7.

Chapter 3, synthesis of the new copper based TIMs was discussed in detail which covered all experimental methods including the preparation of BNNS, functionalization of BNNS, characterization of BNNS, fabrication of TIMs and characterization of the TIMs. A detailed discussion was presented on the new scheme of functionalization of BNNS with TSC. Also, optimization of several parameters like electrolyte concentrations, loading of BNNS in the TIMs and current densities in the preparation of TIMs to obtain the required properties were discussed. In the end, thermal, mechanical properties of the copper based TIMs and theory behind this exceptional performance was discussed.

Chapter 4, Effect of different organic linkers on the properties of the copper based TIMs was discussed. Here, the improvement of the properties due to that addition of external ligands like PEG-dithiol into the electrodeposition was discussed. Here, it is

understood that this behavior is because of the replacement of any air gaps with the ligand but the key was to achieve loadings that do not disturb the nanostructure. Later on, effect of different linker molecules was presented where the conclusion was, the organic linkers changed the nano structure and bond strength with BNNS and copper and all played part in properties. Also, corrosion behavior of the TIMs was discussed.

Chapter 5, Synthesis of silver based TIMs was discussed in detail. All the methods to prepare the TIMs was presented and comparison of the properties of the silver TIMs with copper TIMs was shown. Silver TIMs clearly outperformed copper TIMs in thermal properties but were not as soft as the copper TIMs. Nevertheless, silver TIMs were measured to have lower thermal resistance than the copper TIMs. Later on, the effect of metal-linker bond on the properties of the bulk TIMs was discussed. Here, it was concluded that the thermal properties and mechanical strongly depended on the linker-silver bond strength.

Chapter 6, A new TIM in which polymeric tin (polystannane) was used as the matrix for a composite with graphene nanoparticles was presented. The synthesis of PolySn was discussed and then followed by synthesis of nanocomposite. Thermal conductivity of the samples was presented which showed the nanocomposites had substantially higher value than the polymer. Also, most importantly the improvement of the stability of the polymer in ambient conditions by addition of graphene is shown.

7.2 Future Scope

This work holds a lot of future scope, especially in determining even better components for the different nanocomposites synthesized.

1. Copper TIMs could be produced by changing the filler nanoparticles. The fillers can be graphene or graphene oxide and it is also worth exploring if the TIMs can still perform at the same level with just copper and organic molecules without any filler particles.
2. It was clearly understood that the inclusion of PEG-dithiol as a free standing ligand to occupy the air pores improved the properties. So, there could be more improvements if cyano based ligands are used due to the stronger bonding of the cyano groups compared to thiol groups to copper.
3. The copper and silver based TIMs showcased field disruptive thermal resistances. Also, these resistances were proved to not change over 100 thermal cycles. In general, a TIM is expected to work for at least 1000 cycles reliably and in this light, long term reliability tests are very important.
4. Polymeric tin nanocomposites showed very good thermal properties improved stability due to the presence of graphene. Developing PolySn with different starting monomer units which have conjugation can have much higher thermal transport values than the current composite due to possible synergistic effects.
5. Graphene in the graphene-polymer composites blocks the polymer from light by absorbing most of the light and improves the stability of the composite but using BNNS, the light can be mostly reflected and this can perhaps improve the stability even further. It is also worth noting that the BNNS is more hydrophobic than graphene.

REFERENCES

1. Geer, D. Industry trends: Chip makers turn to multicore processors. *Computer* (Long. Beach. Calif). **38,** 11–13 (2005).
2. Sim, L. C., Ramanan, S. R., Ismail, H., Seetharamu, K. N. & Goh, T. J. Thermal characterization of Al_2O_3 and ZnO reinforced silicone rubber as thermal pads for heat dissipation purposes. *Thermochim. Acta* **430,** 155–165 (2005).
3. Michael, A. Next Gen Smart Grid Equipment Challenges Power Supply Designers. *Electronic Design* (2010).
4. Ghosh1, S., Calizo1, I., Teweldebrhan1, D., Pokatilov1, E. P., Nika, D. L. *et al.* Extremely high thermal conductivity of graphene: Prospects for thermal management applications in nanoelectronic circuits. *Appl. Phys. Lett.* **92,** (2008).
5. Zhang, Y., Dembla, A. & Bakir, M. S. Silicon micropin-fin heat sink with integrated TSVs for 3-D ICs: tradeoff analysis and experimental testing. *IEEE Trans. Components, Packag. Manuf. Technol.* **3,** 1842–1850 (2013).
6. Madhusudana, C. V. *Thermal Contact Conductance*. (Springer New York, 1996). doi:10.1007/978-1-4612-3978-9
7. Schaller, R. R. Moore's law: past, present and future. *Spectrum, IEEE* **34,** 52–59 (1997).
8. Wgsimon. Transistor Count and Moore's Law - 2011 - User:Wgsimon - Wikimedia Commons. (2011). <https://commons.wikimedia.org/wiki/User:Wgsimon#/media/File:Transistor_Count_and_Moore%27s_Law_-_2011.svg>
9. Mason, J. A., Oktawiec, J., Taylor, M. K., Hudson, M. R., Rodriguez, J. *et al.* Methane storage in flexible metal–organic frameworks with intrinsic thermal management. *Nature* **527,** 5–7 (2015).
10. Huang, H., Liu, C., Wu, Y. & Fan, S. Aligned carbon nanotube composite films for thermal management. *Adv. Mater.* **17,** 1652–1656 (2005).
11. Yan, Z., Liu, G., Khan, J. M. & Balandin, A. a. Graphene quilts for thermal management of high-power GaN transistors. *Nat. Commun.* **3,** 827 (2012).
12. Chen, J., Huang, X., Zhu, Y. & Jiang, P. Cellulose Nanofiber Supported 3D Interconnected BN Nanosheets for Epoxy Nanocomposites with Ultrahigh Thermal Management Capability. *Adv. Funct. Mater.* **27,** 1–9 (2017).
13. Balčytis, A. *et al.* Nano-rescaling of gold films on polystyrene: thermal management for SERS. *Nanoscale* **9,** 690–695 (2016).
14. Song, N. *et al.* Highly Anisotropic Thermal Conductivity of Layer-by-Layer Assembled Nanofibrillated Cellulose/Graphene Nanosheets Hybrid Films for Thermal Management. *ACS Appl. Mater. Interfaces* **9,** 2924–2932 (2017).
15. Kwon, S., Zheng, J., Wingert, M. C., Cui, S. & Chen, R. Unusually High and Anisotropic Thermal Conductivity in Amorphous Silicon Nanostructures. *ACS Nano* **11,** 2470–2476 (2017).
16. Alam, F. E. *et al.* In situ formation of a cellular graphene framework in thermoplastic composites leading to superior thermal conductivity. *J. Mater. Chem.*

A **5,** 6164–6169 (2017).
17. Hu, J., Huang, Y., Yao, Y., Pan, G., Sun, J., Zeng, X. *et al.* Polymer Composite with Improved Thermal Conductivity by Constructing a Hierarchically Ordered Three-Dimensional Interconnected Network of BN. *ACS Appl. Mater. Interfaces* **9,** 13544–13553 (2017).
18. van Wyk, J. D. & Lee, F. C. On a Future for Power Electronics. *Emerg. Sel. Top. Power Electron. IEEE J.* **1,** 59–72 (2013).
19. Hamut, H. S., Dincer, I. & Naterer, G. F. Exergy analysis of a TMS (thermal management system) for range-extended EVs (electric vehicles). *Energy* **46,** 117–125 (2012).
20. Chung, D. D. L. Thermal Interface Materials. *J. Mater. Eng. Perform.* **10,** 56–59 (2001).
21. Wolff, E. G. & Schneider, D. A. Prediction of thermal contact resistance between polished surfaces. *Int. J. Heat Mass Transf.* **41,** 3469–3482 (1998).
22. Satre, V. & Lallemand, M. Enhancement of thermal contact conductance for electronic systems. *Appl. Therm. Eng.* **21,** 221–235 (2001).
23. Prasher, R. Thermal Interface Materials: Historical Perspective, Status, and Future Directions. *Proc. IEEE* **94,** 1571–1586 (2006).
24. Bar-Cohen, A., Matin, K. & Narumanchi, S. Nanothermal Interface Materials: Technology Review and Recent Results. *J. Electron. Packag.* **137,** 40803–40817 (2015).
25. Goyal, V. & Balandin, A. A. Thermal properties of the hybrid graphene-metal nano-micro-composites: Applications in thermal interface materials. *Appl. Phys. Lett.* **100,** (2012).
26. Yu, A., Ramesh, P., Sun, X., Bekyarova, E., Itkis, M. E. *et al.* Enhanced Thermal Conductivity in a Hybrid Graphite Nanoplatelet - Carbon Nanotube Filler for Epoxy Composites. *Adv. Mater.* **20,** 4740–4744 (2008).
27. Yovanovich, M. M. Four decades of research on thermal contact, gap, and joint resistance in microelectronics. *IEEE Trans. components Packag. Technol.* **28,** 182–206 (2005).
28. Jackson, R. L., Bhavnani, S. H. & Ferguson, T. P. A multiscale model of thermal contact resistance between rough surfaces. *J. Heat Transfer* **130,** 81301 (2008).
29. Dutta, I., Raj, R., Kumar, P., Chen, T., Nagaraj, C. M. *et al.* Liquid phase sintered solders with indium as minority phase for next generation thermal interface material applications. *J. Electron. Mater.* **38,** 2735–2745 (2009).
30. Plumbridge, W. J. Review Solders in electronics. *J. Mater. Sci.* **31,** 2501–2514 (1996).
31. Kariya, Y. & Otsuka, M. Mechanical fatigue characteristics of Sn-3.5Ag-X (X = Bi, Cu, Zn and In) solder alloys. *J. Electron. Mater.* **27,** 1229–1235 (1998).
32. Suraski, D. & Seelig, K. The Current Status of Lead-Free Solder Alloys. *IEEE Trans. Electron. Packag. Manuf.* **24,** 244–248 (2001).
33. Harrison, M. R., Vincent, J. H. & Steen, H. A. H. Lead-free reflow soldering for electronics assembly. *Solder. Surf. Mt. Technol.* **13,** 21–38 (2001).
34. Felton, L. E., Raeder, C. H. & Knorr, D. B. The properties of tin-bismuth alloy

solders. *Jom* **45,** 28–32 (1993).
35. Zweben, C. Thermal materials solve power electronics challenges. *Power Electron. Technol.* **32,** 40–47 (2006).
36. Grivas, D., Frear, D., Quan, L. & Morris, J. W. J. The Formation of Cu3Sn Intermetallic on the Reaction of Cu with 95Pb-5Sn Solder. *J. Electron. Mater.* **15,** 355–359 (1986).
37. Sarvar, F., Whalley, D. & Conway, P. Thermal Interface Materials - A Review of the State of the Art. *2006 1st Electron. Syst. Technol. Conf.* **2,** 1292–1302 (2006).
38. Ishizuka, M. Application of the thermal network method to the transient thermal analysis of multichip modules. *Heat Transf. - Asian Res.* **26,** 541–553 (1997).
39. Lu, X., Xu, G., Hofstra, P. G. & Bajcar, R. C. Moisture – Absorption , Dielectric Relaxation , and Thermal Conductivity Studies of Polymer Composites. *Polymer (Guildf).* 2259–2265 (1997). doi:10.1002/(SICI)1099-0488(19980930)36:13<2259::AID-POLB2>3.0.CO;2-O
40. Fabris, D., Rosshirt, M., Cardenas, C., Wilhite, P., Yamada, T. *et al.* Application of Carbon Nanotubes to Thermal Interface Materials. *J. Electron. Packag.* **133,** 20902 (2011).
41. Kiran, C. S. & Nanda, K. K. Enhancement of commercially-available thermal grease by multiwalled carbon nanotubes for electronic device applications. *Adv Mater Lett* **4,** 22–25 (2013).
42. Xu, Y., Leong, C. K. & Chung, D. D. L. Carbon nanotube thermal pastes for improving thermal contacts. *J. Electron. Mater.* **36,** 1181–1187 (2007).
43. Formula 7 - antec. at <http://store.antec.com/thermal-paste/formula-7.html>
44. ArcticSilver. Arctic Silver 5. (2015). at <http://www.arcticsilver.com/as5.htm>
45. Booth, R. B., Grube, G. W., Gruber, P. A., Khandros, I. Y. & Zingher, R. Liquid metal matrix thermal paste. 1–9 (1993).
46. Dolbear, T. P., MacKay, C. A. & Nelsom, R. D. LIQUID METAL PASTE FOR THERMAL AND ELECTRICAL CONNECTIONS. (1992).
47. Kang, S. K., Purushothaman, S. & Simonyi, E. E. THERMALLY CONDUCTING MATERIALS AND APPLICATIONS FOR MICROELECTRONIC PACKAGING. (2000). doi:10.1145/634067.634234.
48. Harmon, J., Heffner, K., Fleischman, S. & Dalzell, W. Thermally conductive composite and uses for microelectronic packaging. (2005).
49. Nguyen, M. N. & Grundy, J. D. Compliant and crosslinkable thermal interface materials. (1999).
50. Shinozaki, K., Anzai, K., Takano, T. & Tsuge, A. Aluminum nitride-based sintered body of high thermal conductivity. (1988).
51. Wang, W., Yang, X., Fang, Y., Ding, J. & Yan, J. Enhanced thermal conductivity and thermal performance of form-stable composite phase change materials by using β-Aluminum nitride. *Appl. Energy* **86,** 1196–1200 (2009).
52. Iruvanti, S., Kemink, R. G., Kumar, R., Ostrander, S. P. & Singh, P. Low compressive force, non-silicone, high thermal conducting formulation for thermal interface material and package. (2010).
53. Iruvanti, S. & Yankowski Jr, E. L. Thermal paste for low temperature applications.

(2003).
54. Lin, C. & Chung, D. D. L. Nanostructured fumed metal oxides for thermal interface pastes. *J. Mater. Sci.* **42,** 9245–9255 (2007).
55. Becker, G., Lee, C. & Lin, Z. Thermal conductivity in advanced chips: Emerging generation of thermal greases offers advantages. *Adv. Packag.* **14,** 14 (2005).
56. Gwinn, J. P. & Webb, R. L. Performance and testing of thermal interface materials. *Microelectronics J.* **34,** 215–222 (2003).
57. Viswanath, R., Wakharkar, V., Watwe, Ab. & Lebonheur, V. Thermal Performance Challenges from Silicon to Systems. *Intel Technol. J. Q3,* 1–16 (2000).
58. Khatri, P. & Ziemski, J. 'Dry-To-The-Touch' Thermal Grease Prakash. *2001 Int. Symp. Adv. Packag. Mater.* 236–239 (2001).
59. Macris, C., Sanderson, T., Ebel, R. & Leyerle, C. Performance, Reliability and Approaches Using a Low Melt Alloy as a Thermal Interface Material. *37th Int. Symp. Microelectron.* (2004). at <http://enerdynesolutions.com/downloads/imaps_2004_man.pdf>
60. Webb, R. L., & Gwinn, J. P., Low Melting Point Thermal Interface Material. *ITHERM 2002, 8th Intersoc. Conf. Therm. Thermomechanical Phenom. Electron. Syst.* 671–676 (2002).
61. Chen, G.-L. Thermal interface material and method for manufacturing same. (2004).
62. Fullem, T. Z., Rae, D. F., Sharma, a., Wolcott, J. a. & Cotts, E. J. Thermal characterization of thermal interface material bondlines. *2008 11th Intersoc. Conf. Therm. Thermomechanical Phenom. Electron. Syst.* 174–179 (2008). doi:10.1109/ITHERM.2008.4544268
63. Xu, Y., Chung, D. D. L. & Mroz, C. Thermally conducting aluminum nitride polymer-matrix composites. *Compos. - Part A* **32,** 1749–1757 (2001).
64. Yu, H., Li, L., Kido, T., Xi, G., Xu, G. *et al.* Thermal and Insulating Properties of Epoxy/Aluminum Nitride Composites Used for Thermal Interface Material *J. Appl. Polym. Sci.* **124,** 669–677 (2012).
65. Davison, P. & Koning, P. Component packaging apparatus, systems, and methods. (2003).
66. Huang, H., Wu, Y., Liu, C.-H. & Fan, S.-S. Method for making a thermal interface material. (2008).
67. Matayabas Jr, J. C. & Koning, P. A. Phase change thermal interface materials including polyester resin. (2008).
68. Jayaraman, S., Koning, P. A. & Dani, A. Polymer matrices for polymer solder hybrid materials. (2007).
69. Bergin, J. M. Thermal interface material having a zone-coated release linear. (2003).
70. Yu, A., Ramesh, P., Itkis, M. E., Bekyarova, E. & Haddon, R. C. Graphite Nanoplatelet - Epoxy Composite Thermal Interface Materials. *J. Phys. Chem. C* **111,** 7565–7569 (2007).
71. Shahil, K. M. F. & Balandin, A. a. 【SM】Graphene-multilayer graphene nanocomposites as highly efficient thermal interface materials. *Nano Lett.* **12,** 861–

867 (2012).
72. Chen, S., Wu, Q., Mishra, C., Kang, J., Zhang, H. *et al.* Thermal conductivity of isotopically modified graphene. *Nat Mater* **11,** 203–207 (2012).
73. Bryning, M. B., Milkie, D. E., Islam, M. F., Kikkawa, J. M. & Yodh, A. G. Thermal conductivity and interfacial resistance in single-wall carbon nanotube epoxy composites. *Appl. Phys. Lett.* **87,** 1–3 (2005).
74. Marconnet, A. M., Yamamoto, N., Panzer, M. a., Wardle, B. L. & Goodson, K. E. Thermal Conduction in Aligned Carbon Nanotube- Polymer Nanocomposites with High Packing Density. *ACS Nano* **5,** 4818–4825 (2011).
75. Gojny, F. H., Wichmann, M. H., Fiedler, B., Kinloch, I. A., Bauhofer, W. *et al.* Evaluation and identification of electrical and thermal conduction mechanisms in carbon nanotube/epoxy composites. *Polymer (Guildf).* **47,** 2036–2045 (2006).
76. Xu, J. & Fisher, T. S. Enhancement of thermal interface materials with carbon nanotube arrays. *Int. J. Heat Mass Transf.* **49,** 1658–1666 (2006).
77. Ngo, Q., Cruden, B. A., Cassell, A. M., Sims, G., Meyyappan, M. *et al.* Thermal Interface Properties of Cu-filled Vertically Aligned Carbon Nanofiber Arrays. *Nano Lett.* **4,** 2403–2407 (2004).
78. Cruden, B. A., Cassell, A. M., Ye, Q. & Meyyappan, M. Reactor design considerations in the hot filament/direct current plasma synthesis of carbon nanofibers. *J. Appl. Phys.* **94,** 4070–4078 (2003).
79. Hu, X. J., Panzer, M. A. & Goodson, K. E. Infrared microscopy thermal characterization of opposing carbon nanotube arrays. *J. Heat Transf. Asme* **129,** 91–93 (2007).
80. Tong, T., Zhao, Y., Delzeit, L., Kashani, A., Meyyappan, M. *et al.* Dense vertically aligned multiwalled carbon nanotube arrays as thermal interface materials. *IEEE Trans. Components Packag. Technol.* **30,** 92–100 (2007).
81. Xu, J. & Fisher, T. S. Enhanced thermal contact conductance using carbon nanotube arrays. *ITherm 2004 - Ninth Intersoc. Conf. Therm. Thermomechanical Phenom. Electron. Syst.* **2,** 549–555 (2004).
82. Cola, B. A., Xu, J., Cheng, C., Xu, X., Fisher, T. S. *et al.* Photoacoustic characterization of carbon nanotube array thermal interfaces. *J. Appl. Phys.* **101,** (2007).
83. Kim, P., Shi, L., Majumdar, a & McEuen, P. L. Thermal transport measurements of individual multiwalled nanotubes. *Phys. Rev. Lett.* **87,** 215502 (2001).
84. Wang, X., Zhong, Z. & Xu, J. Non-Contact Thermal Characterization of Individual Multi-wall Carbon Nanotubes. *37th AIAA Thermophys. Conf.* 1–6 (2004). doi:doi:10.2514/6.2004-2465
85. Zhang, Q., Chen, G., Yoon, S. F., Ahn, J., Wang, S. G. *et al.* Thermal conductivity of multiwalled carbon nanotubes. *Phys. Rev. B* **66,** 6 (2002).
86. Pettes, M. T. & Shi, L. Thermal and structural characterizations of individual single-, double-, and multi-walled carbon nanotubes. *Adv. Funct. Mater.* **19,** 3918–3925 (2009).
87. Taphouse, J. H., Smith, O. L., Marder, S. R. & Cola, B. A. A pyrenylpropyl phosphonic acid surface modifier for mitigating the thermal resistance of carbon

nanotube contacts. *Adv. Funct. Mater.* **24,** 465–471 (2014).
88. Carlberg, B., Ye, L. L. & Liu, J. Polymer-metal nanofibrous composite for thermal management of microsystems. *Mater. Lett.* **75,** 229–232 (2012).
89. Zandén, C., Luo, X., Ye, L. & Liu, J. A new solder matrix nano polymer composite for thermal management applications. *Compos. Sci. Technol.* **94,** 54–61 (2014).
90. Sun, S., Chen, S., Luo, X., Fu, Y., Ye, L. *et al.* Mechanical and thermal characterization of a novel nanocomposite thermal interface material for electronic packaging. *Microelectron. Reliab.* **56,** 129–135 (2016).
91. Luo, X., Zhang, Y., Zandén, C., Murugesan, M., Cao, Y. *et al.* Novel thermal interface materials: boron nitride nanofiber and indium composites for electronics heat dissipation applications. *J. Mater. Sci. Mater. Electron.* **25,** 2333–2338 (2014).
92. Wunderle, B., Klein, M., Dietrich, L., Ras, M. A., Mrossko, R. *et al.* Advances in thermal interface technology: Mono-metal interconnect formation, processing and characterisation. *2010 12th IEEE Intersoc. Conf. Therm. Thermomechanical Phenom. Electron. Syst. ITherm 2010* (2010). doi:10.1109/ITHERM.2010.5501343
93. Voorhees, P. W. The Theory of Ostwald Ripening. *J. Stat. Phys.* **38,** 231–252 (1985).
94. Balandin, A. a. Thermal properties of graphene and nanostructured carbon materials. *Nat. Mater.* **10,** 569–581 (2011).
95. Leong, C. K., Aoyagi, Y. & Chung, D. D. L. Carbon black pastes as coatings for improving thermal gap-filling materials. *Carbon N. Y.* **44,** 435–440 (2006).
96. Donnay, M., Tzavalas, S. & Logakis, E. Boron nitride filled epoxy with improved thermal conductivity and dielectric breakdown strength. *Compos. Sci. Technol.* (2015). doi:10.1016/j.compscitech.2015.02.006
97. Draman, S. F. S., Daik, R., El-Sheikh, S. M. & Latif, F. A. Thermally Conductive Adhesive from Chemically Modified Cellulose and Nanoparticle of Surfactant-Doped Polypyrrole. *Macromol. Symp.* **353,** 24–30 (2015).
98. Hou, J., Li, G., Yang, N., Qin, L., Grami, M. E. *et al.* Preparation and characterization of surface modified boron nitride epoxy composites with enhanced thermal conductivity. *RSC Adv.* **4,** 44282–44290 (2014).
99. Song, W. L., Wang, P., Cao, L., Anderson, A., Meziani, M. J. *et al.* Polymer/boron nitride nanocomposite materials for superior thermal transport performance. *Angew. Chem. Int. Ed. Engl.* **51,** 6498–501 (2012).
100. Tang, B., Hu, G., Gao, H. & Hai, L. Application of graphene as filler to improve thermal transport property of epoxy resin for thermal interface materials. *Int. J. Heat Mass Transf.* **85,** 420–429 (2015).
101. Uetani, K., Ata, S., Tomonoh, S., Yamada, T., Yumura, M. *et al.* Elastomeric thermal interface materials with high through-plane thermal conductivity from carbon fiber fillers vertically aligned by electrostatic flocking. *Adv. Mater.* 5857–5862 (2014). doi:10.1002/adma.201401736
102. Xu, H., Zhou, H., Chen, X. & Liu, Y. High thermal conductive composites based on flake graphite filled in a partial compatible polyamide 6/polypropylene. *Polym. Sci. Ser. A* (2015). doi:10.1134/S0965545X1505017X
103. Yang, S. Y., Ma, C. C. M., Teng, C. C., Huang, Y. W., Liao, S. H. *et al.* Effect of

functionalized carbon nanotubes on the thermal conductivity of epoxy composites. *Carbon N. Y.* **48,** 592–603 (2010).
104. Yu, J., Mo, H. & Jiang, P. Polymer/boron nitride nanosheet composite with high thermal conductivity and sufficient dielectric strength. *Polym. Adv. Technol.* (2015). doi:10.1002/pat.3481
105. Yu, W., Xie, H., Yin, L., Zhao, J., Xia, L. *et al.* Exceptionally high thermal conductivity of thermal grease: Synergistic effects of graphene and alumina. *Int. J. Therm. Sci.* **91,** 76–82 (2015).
106. Yuen, S. M., Ma, C. C. M., Chiang, C. L., Chang, J. A., Huang, S. W. *et al.* Silane-modified MWCNT/PMMA composites - Preparation, electrical resistivity, thermal conductivity and thermal stability. **38,** 2527–2535 (2010).
107. Zhu, X. W., Sakka, Y., Zhou, Y., Hirao, K. & Itatani, K. A strategy for fabricating textured silicon nitride with enhanced thermal conductivity. *J. Eur. Ceram. Soc.* (2014). doi:10.1016/j.jeurceramsoc.2014.01.025
108. Zhi, C., Bando, Y., Tang, C. & Golberg, D. Boron nitride nanotubes. *Mater. Sci. Eng. R Reports* **70,** 92–111 (2010).
109. Lin, Y. & Connell, J. W. Advances in 2D boron nitride nanostructures: nanosheets, nanoribbons, nanomeshes, and hybrids with graphene. *Nanoscale* **4,** 6908 (2012).
110. Lindsay, L. & Broido, D. a. Enhanced thermal conductivity and isotope effect in single-layer hexagonal boron nitride. *Phys. Rev. B* **84,** 1–6 (2011).
111. Pham, T., Goldstein, A. P., Lewicki, J. P., Kucheyev, S. O., Wang, C. *et al.* Nanoscale structure and superhydrophobicity of sp2-bonded boron nitride aerogels. *Nanoscale* **7,** 10449–10458 (2015).
112. Balmain, W. H. Observations on the formation of compounds of boron and silicon with nitrogen and certain metals. *Philos. Mag. Ser. 3* **21,** 270–277 (1842).
113. Pakdel, A., Bando, Y. & Golberg, D. Nano boron nitride flatland. *Chem. Soc. Rev.* **43,** 934–959 (2014).
114. Chopra, N. G., Luyken, R. J., Cherrey, K., & Crespi, V. H. Boron Nitride Nanotubes. *Science* **269,** 966–967 (1995).
115. Novoselov, K. S., Jiang, D., Schedin, F., Booth, T. J., Khotkevich, V. V. *et al.* Two-dimensional atomic crystals. *Proc. Natl. Acad. Sci. U. S. A.* **102,** 10451–10453 (2005).
116. Pakdel, A., Zhi, C., Bando, Y. & Golberg, D. Low-dimensional boron nitride nanomaterials. *Mater. Today* **15,** 256–265 (2012).
117. Golberg, D., Bando, Y., Eremets, M., Takemura, K., Kurashima, K. *et al.* Nanotubes in boron nitride laser heated at high pressure. *Appl. Phys. Lett.* **69,** 2045 (1996).
118. Han, W., Bando, Y., Kurashima, K. & Sato, T. Synthesis of boron nitride nanotubes from carbon nanotubes by a substitution reaction. *Appl. Phys. Lett.* **73,** 3085–3087 (1998).
119. Lourie, O. R., Jones, C. R., Bartlett, B. M., Gibbons, P. C., Ruoff, R. S. *et al.* CVD Growth of Boron Nitride Nanotubes. *Chem. Mater.* **12,** 1808–1810 (2000).
120. Pacilé, D., Meyer, J. C., Girit, C. O. & Zettl, a. The two-dimensional phase of boron nitride: Few-atomic-layer sheets and suspended membranes. *Appl. Phys.*

Lett. **92,** 133107 (2008).
121. Li, L. H., Chen, Y., Behan, G., Zhang, H., Petravic, M. *et al.* Large-scale mechanical peeling of boron nitride nanosheets by low-energy ball milling. *J. Mater. Chem.* **21,** 11862 (2011).
122. Corso, M., Auwa, W., Muntwiler, M. & Tamai, A. Boron nitride nanomesh. *Science* **303,** 217–20 (2004).
123. Auwärter, W., Kreutz, T. J., Greber, T. & Osterwalder, J. XPD and STM investigation of hexagonal boron nitride on Ni(111). *Surf. Sci.* **429,** 229–236 (1999).
124. Kawanowa, H., Yamamoto, K., Otani, S., Kobayashi, K., Gotoh, Y. *et al.* ARUPS study of graphitic boron terminated WB2(0001) surface. *Surf. Sci.* **463,** 191–198 (2000).
125. Han, W. Q., Wu, L., Zhu, Y., Watanabe, K. & Taniguchi, T. Structure of chemically derived mono- and few-atomic-layer boron nitride sheets. *Appl. Phys. Lett.* **93,** 91–94 (2008).
126. Coleman, J. N., Lotya, M., O'Neill, A., Bergin, S. D., King, P. J. *et al.* Two-Dimensional Nanosheets Produced by Liquid Exfoliation of Layered Materials. *Science (80-.).* **331,** 568–571 (2011).
127. Zhi, C., Bando, Y., Tang, C., Kuwahara, H., & Golberg, D. *et al.* Large-Scale Fabrication of Boron Nitride Nanosheets and Their Utilization in Polymeric Composites with Improved Thermal and Mechanical Properties. *Adv. Mater.* **21,** 2889–2893 (2009).
128. Gao, R., Yin, L., Wang, C., Qi, Y., Lun, N. *et al.* High-yield synthesis of boron nitride nanosheets with strong ultraviolet. *J. Phys. Chem. C* **113,** 15160–15165 (2009).
129. Song, L., Ci, L., Lu, H., Sorokin, P. B., Jin, C. *et al.* Large scale growth and characterization of atomic hexagonal boron nitride layers. *Nano Lett.* **10,** 3209–15 (2010).
130. Shi, Y., Hamsen, C., Jia, X., Kim, K. K., Reina, A. *et al.* Synthesis of few-layer hexagonal boron nitride thin film by chemical vapor deposition. *Nano Lett.* **10,** 4134–4139 (2010).
131. Kim, K. K., Hsu, A., Jia, X., Kim, S. M., Shi, Y. *et al.* Synthesis of monolayer hexagonal boron nitride on Cu foil using chemical vapor deposition. *Nano Lett.* **12,** 161–6 (2012).
132. Marom, N., Bernstein, J., Garel, J., Tkatchenko, A., Joselevich, E. *et al.* Stacking and registry effects in layered materials: The case of hexagonal boron nitride. *Phys. Rev. Lett.* **105,** 1–4 (2010).
133. Pauling, L. The Structure and Properties of Graphite and Boron Nitride. *Proc. Natl. Acad. Sci.* **56,** 1646–1652 (1966).
134. Zhou, K. G., Mao, N. N., Wang, H. X., Peng, Y. & Zhang, H. L. A mixed-solvent strategy for efficient exfoliation of inorganic graphene analogues. *Angew. Chemie - Int. Ed.* **50,** 10839–10842 (2011).
135. Smith, R. J., King, P. J., Lotya, M., Wirtz, C., Khan, U. *et al.* Large-scale exfoliation of inorganic layered compounds in aqueous surfactant solutions. *Adv. Mater.* **23,**

3944–3948 (2011).
136. May, P., Khan, U., Hughes, J. M. & Coleman, J. N. Role of solubility parameters in understanding the steric stabilization of exfoliated two-dimensional nanosheets by adsorbed polymers. *J. Phys. Chem. C* **116,** 11393–11400 (2012).
137. Lin, Y., Williams, T. V, Cao, W., Elsayed-Ali, H. E. & Connell, J. W. Defect Functionalization of Hexagonal Boron Nitride Nanosheets. *J. Phys. Chem. C* **114,** 17434–17439 (2010).
138. Ikuno, T., Sainsbury, T., Okawa, D., Fréchet, J. M. J. & Zettl, a. Amine-functionalized boron nitride nanotubes. *Solid State Commun.* **142,** 643–646 (2007).
139. Maguer, A., Leroy, E., Bresson, L., Doris, E., Loiseau, A. *et al.* A versatile strategy for the functionalization of boron nitride nanotubes. *J. Mater. Chem.* **19,** 1271–1275 (2009).
140. Nag, A., Raidongia, K., Hembram, K. P., Datta, R., Waghmare, U. V. *et al.* Graphene analogues of BN: Novel synthesis and properties. *ACS Nano* **4,** 1539–1544 (2010).
141. Pal, S., Vivekchand, S. R. C., Govindaraj, A. & Rao, C. N. R. Functionalization and solubilization of BN nanotubes by interaction with Lewis bases. *J. Mater. Chem.* **1,** 450–452 (2006).
142. Wu, X., An, W. & Zeng, X. C. Chemical functionalization of boron-nitride nanotubes with NH3 and amino functional groups. *J. Am. Chem. Soc.* **128,** 12001–6 (2006).
143. Xie, S. Y., Wang, W., Fernando, K. S., Wang, X., Lin, Y. *et al.* Solubilization of boron nitride nanotubes. *Chem. Commun. (Camb).* 3670–3672 (2005). doi:10.1039/b505330g
144. Sainsbury, T., Satti, A., May, P., O'Neill, A., Nicolosi, V. *et al.* Covalently functionalized hexagonal boron nitride nanosheets by nitrene addition. *Chemistry* **18,** 10808–12 (2012).
145. Sainsbury, T., Satti, A., May, P., Wang, Z., McGovern, I. *et al.* Oxygen radical functionalization of boron nitride nanosheets. *J. Am. Chem. Soc.* **134,** 18758–71 (2012).
146. Nazarov, A. S., Demin, V. N., Grayfer, E. D., Bulavchenko, A. I., Arymbaeva, A. T. *et al.* Functionalization and dispersion of hexagonal boron nitride (h-BN) nanosheets treated with inorganic reagents. *Chem. - An Asian J.* **7,** 554–560 (2012).
147. Zhi, C. Y., Bando, Y., Tang, C. C., Huang, Q. & Golberg, D. Boron nitride nanotubes: functionalization and composites. *J. Mater. Chem.* **18,** 3900 (2008).
148. Cui, Z., Oyer, A. J., Glover, A. J., Schniepp, H. C. & Adamson, D. H. Large scale thermal exfoliation and functionalization of boron nitride. *Small* **10,** 2352–2355 (2014).
149. Han, W. Q. & Zettl, A. Functionalized boron nitride nanotubes with a stannic oxide coating: A novel chemical route to full coverage. *J. Am. Chem. Soc.* **125,** 2062–2063 (2003).
150. Lin, Y., Williams, T. V., Xu, T. B., Cao, W., Elsayed-Ali, H. E. *et al.* Aqueous Dispersions of Few-Layered and Monolayered Hexagonal Boron Nitride Nanosheets from Sonication-Assisted Hydrolysis: Critical Role of Water. *J. Phys.*

Chem. C **115,** 2679–2685 (2011).
151. Singhal, S. K., Kumar, V., Stalin, K., Choudhary, A., Teotia, S. *et al.* Gold-nanoparticle-decorated boron nitride nanosheets: Structure and optical properties. *Part. Part. Syst. Charact.* **30,** 445–452 (2013).
152. Wang, L., Sun, C., Xu, L. & Qian, Y. Convenient synthesis and applications of gram scale boron nitride nanosheets. *Catal. Sci. Technol.* **1,** 1119 (2011).
153. Novoselov, K. S., Geim, A. K., Morozov, S. V., Jiang, D., Zhang, Y. *et al.* Electric field effect in atomically thin carbon films. *Science (80-.).* **306,** 666–669 (2004).
154. Allen, M. J., Tung, V. C. & Kaner, R. B. Honeycomb carbon -- A study of graphene. *Chem. Rev.* **110,** 132–145 (2010).
155. Zhu, Y., Murali, S., Cai, W., Li, X., Suk, J. W. *et al.* Graphene and graphene oxide: Synthesis, properties, and applications. *Adv. Mater.* **22,** 3906–3924 (2010).
156. Segal, M. Selling graphene by the ton. *Nat. Nanotechnol.* **4,** 612–614 (2009).
157. Schniepp, H. C., Li, J. L., McAllister, M. J., Sai, H., Herrera-Alonso, M. *et al.* Functionalized Single Graphene Sheets Derived from Splitting Graphite Oxide. *J. Phys. Chem. B* **110,** 8535–8539 (2006).
158. Li, J. L., Kudin, K. N., McAllister, M. J., Prud'homme, R. K., Aksay, I. A. *et al.* Oxygen-driven unzipping of graphitic materials. *Phys. Rev. Lett.* **96,** 5–8 (2006).
159. Li, D., Müller, M. B., Gilje, S., Kaner, R. B., & Wallace, G. G. Processable aqueous dispersions of graphene nanosheets. *Nat. Nanotechnol.* **3,** 101–105 (2008).
160. Tung, V. C., Allen, M. J., Yang, Y. & Kaner, R. B. High-throughput solution processing of large-scale graphene. *Nat. Nanotechnol.* **4,** 25–29 (2009).
161. Gryglas-Borysiewicz, M., Jouault, B., Tworzydło, J., Lewińska, S., Strupiński, W. *et al.* Transport properties of disordered graphene layers. *Acta Phys. Pol. A* **116,** 838–840 (2009).
162. Nair, R. R., Blake, P., Grigorenko, A. N., Novoselov, K. S., Booth, T. J. *et al.* Fine Structure Constant Defines Visual Transperency of Graphene. *Science.* **320,** 2008 (2008).
163. Berber, S., Kwon, Y. & Tománek, D. Unusually High Thermal Conductivity of Carbon Nanotubes. *Phys. Rev. Lett.* **84,** 4613–4616 (2000).
164. Cai, W., Moore, A. L., Zhu, Y., Li, X., Chen, S. *et al.* Thermal transport in suspended and supported monolayer graphene grown by chemical vapor deposition. *Nano Lett.* **10,** 1645–1651 (2010).
165. Pop, E., Varshney, V. & Roy, A. K. a. K. Thermal properties of graphene: Fundamentals and applications. *MRS Bull.* **37,** 1273–1281 (2012).
166. Ho, C. Y., Powell, R. W. & Liley, P. E. Thermal Conductivity of the Elements. *J. Phys. Chem. Ref. Data* **1,** 279–421 (1972).
167. Trummer, M., Choffat, F., Smith, P. & Caseri, W. Polystannanes : Synthesis , Properties , and Outlook. 448–460
168. Imori, T., Lu, V., Cai, H. & Tilley, T. D. Metal-Catalyzed Dehydropolymerization of Secondary Stannanes to High Molecular Weight Polystannanes. *J. Am. Chem. Soc.* **117,** 9931–9940 (1995).
169. Devylder, N., Hill, M., Molloy, K. C. & Price, G. J. Wurtz synthesis of high molecular weight poly(dibuty1stannane). 711–712 (1996).

170. Okano, M., Matsumoto, N., Arakawa, M., Tsuruta, T. & Hamano, H. Electrochemical synthesis of dialkylsubstituted polystannanes and their properties. *Chem. Commun.* 1799–1800 (1998). doi:10.1039/a804299c
171. Babcock, J. R. & Sita, L. R. Highly Branched , High Molecular Weight Polystannane from Dibutylstannane via a Novel Dehydropolymerization / Rearrangement Process. *J. Am. Chem. Soc.* **7863,** 12481–12482 (1996).
172. Choffat, F., Smith, P. & Caseri, W. Facile synthesis of linear poly(dibutylstannane). *J. Mater. Chem.* **15,** 1789 (2005).
173. Choffat, F., Smith, P. & Caseri, W. Polystannanes: Polymers of a molecular, jacketed metal-wire structure. *Adv. Mater.* **20,** 2225–2229 (2008).
174. Okano, M., Takeda, K., Toriumi, T. & Hamano, H. Electrochemical synthesis of polygermanes. *Electrochim. Acta* **44,** 659–666 (1998).
175. Okano, M. & Watanabe, K. Electrochemical synthesis of stannane – silane and stannane – germane copolymers. **2,** 471–474 (2000).
176. Miles, D., Burrow, T., Lough, A. & Foucher, D. Wurtz Coupling of Perfluorinated Dichlorostannanes. *J. Inorg. Organomet. Polym. Mater.* **20,** 544–553 (2010).
177. Choffat, F., Käser, S., Wolfer, P., Schmid, D., Mezzenga, R. *et al.* Synthesis and Characterization of Linear Poly (dialkylstannane). *Macromolecules* **40,** 7878–7889 (2007).
178. Choffat, F., Wolfer, P., Smith, P. & Caseri, W. Light-stability of poly(dialkylstannane)s. *Macromol. Mater. Eng.* **295,** 210–221 (2010).
179. Trummer, M., Nauser, T., Lechner, M. L., Uhlig, F. & Caseri, W. Stability of polystannanes towards light. *Polym. Degrad. Stab.* **96,** 1841–1846 (2011).
180. Losego, M. D., Grady, M. E., Sottos, N. R., Cahill, D. G. & Braun, P. V. Effects of chemical bonding on heat transport across interfaces. *Nat. Mater.* **11,** 502–506 (2012).
181. O'Brien, P. J., Shenogin, S., Liu, J., Chow, P. K., Laurencin, D. *et al.* Bonding-induced thermal conductance enhancement at inorganic heterointerfaces using nanomolecular monolayers. *Nat. Mater.* **12,** 118–22 (2013).
182. Phelan, P. E. & Niemann, R. C. Effective Thermal Conductivity of a Thin, Randomly Oriented Composite Material. *J. Heat Transfer* **120,** 971 (1998).
183. Jo, I. *et al.* Thermal conductivity and phonon transport in suspended few-layer hexagonal boron nitride. *Nano Lett.* **13,** 550–554 (2013).
184. Min, Y., Akbulut, M., Kristiansen, K., Golan, Y. & Israelachvili, J. The role of interparticle and external forces in nanoparticle assembly. *Nat. Mater.* **7,** 527–38 (2008).
185. Halpin, J. C. & Kardos, J. L. The Halpin-Tsai equations: A review. *Polym. Eng. Sci.* **16,** 344–352 (1976).
186. Rafiee, M. A., Rafiee, J., Wang, Z., Song, H., Yu, Z. Z. *et al.* Enhanced mechanical properties of nanocomposites at low graphene content. *ACS Nano* **3,** 3884–3890 (2009).
187. Li, Y., Jia, W. Z., Song, Y. Y. & Xia, X. H. Superhydrophobicity of 3D porous copper films prepared using the hydrogen bubble dynamic template. *Chem. Mater.* **19,** 5758–5764 (2007).

188. Fabricius, G. & Sundholm, G. The effect of additives on the electrodeposition of copper. *Trans. Inst. Met. Finish.* **83,** 194–198 (2005).
189. Mammeri, F., Le Eric, B., Rozes, L. & Sanchez, C. Mechanical properties of hybrid organic-inorganic materials. *J. Mater. Chem.* **15,** 3787–3811 (2005).
190. Li, C., Bando, Y., Zhi, C., Huang, Y. & Golberg, D. Thickness-dependent bending modulus of hexagonal boron nitride nanosheets. *Nanotechnology* **20,** 385707 (2009).
191. Kudin, K. N., Scuseria, G. E. & Yakobson, B. I. C2F, BN, and C nanoshell elasticity from ab initio computations. *Phys. Rev. B* **64,** 235406 (2001).
192. Narumanchi, S., Mihalic, M., Kelly, K. & Eesley, G. Thermal interface materials for power electronics applications. *2008 11th Intersoc. Conf. Therm. Thermomechanical Phenom. Electron. Syst.* 395–404 (2008). doi:10.1109/ITHERM.2008.4544297
193. Sun, S., Chen, S., Luo, X., Fu, Y., Ye, L. Sun, S. *et al.* Mechanical and thermal characterization of a novel nanocomposite thermal interface material for electronic packaging. *Microelectron. Reliab.* **56,** 129–135 (2015).
194. Losego, M. D. & Cahill, D. G. Thermal transport: Breaking through barriers. *Nat. Mater.* **12,** 382–4 (2013).
195. Koch, G. H., Brongers, M. P. H., Thompson, N. G., Virmani, Y. P. & Payer, J. H. *Corrosion cost and preventive strategies in the United States*. (2002).
196. Stupnišek-Lisac, E., Cinotti, V. & Reichenbach, D. Atmospheric corrosion inhibitors for copperin the electronics industry. *J. Appl. Electrochem.* **29,** 117–122 (1999).
197. Krishnamurthy, A., Gadhamshetty, V., Mukherjee, R., Natarajan, B., Eksik, O. *et al.* Superiority of Graphene over Polymer Coatings for Prevention of Microbially Induced Corrosion. *Sci. Rep.* **5,** 13858 (2015).
198. Pushpavanam, M., Raman, V. & Shenoi, B. A. RHODIUM - ELECTRODEPOSITION AND APPLICATIONS MALATHY. *Surf. Technol.* **12,** 351–360 (1981).
199. Gelling, V. J., Wiest, M. M., Tallman, D. E., Bierwagen, G. P. & Wallace, G. G. Electroactive-conducting polymers for corrosion control: 4. Studies of poly(3-octyl pyrrole) and poly(3-octadecyl pyrrole) on aluminum 2024-T3 alloy. *Prog. Org. Coatings* **43,** 149–157 (2001).
200. Tallman, D. E., Spinks, G., Dominis, A. & Wallace, G. G. Electroactive conducting polymers for corrosion control. *J. Solid State Electrochem.* **6,** 73–84 (2002).
201. Lusk, a T. & Jennings, G. K. Characterization of Self-Assembled Monolayers Formed from Sodium. *Langmuir* **17,** 7830–7836 (2001).
202. Prasai, D., Tuberquia, J. C., Harl, R. R., Jennings, G. K. & Bolotin, K. I. Graphene : Corrosion-Inhibiting Coating. *ACS Nano* **6,** 1102–1108 (2012).
203. Luechinger, N. A., Athanassiou, E. K. & Stark, W. J. Graphene-stabilized copper nanoparticles as an air-stable substitute for silver and gold in low-cost ink-jet printable electronics. *Nanotechnology* **19,** 445201 (2008).
204. Kirkland, N. T., Schiller, T., Medhekar, N. & Birbilis, N. Exploring graphene as a corrosion protection barrier. *Corros. Sci.* **56,** 1–4 (2012).

205. Krishnamurthy, A., Gadhamshetty, V., Mukherjee, R., Chen, Z., Ren, W. *et al.* Passivation of microbial corrosion using a graphene coating. *Carbon.* **56,** 45–49 (2013).
206. Chang, C. H., Huang, T. C., Peng, C. W., Yeh, T. C., Lu, H. I. *et al.* Novel anticorrosion coatings prepared from polyaniline/graphene composites. *Carbon N. Y.* **50,** 5044–5051 (2012).
207. Zhou, F., Li, Z., Shenoy, G. J., Li, L. & Liu, H. Enhanced Room Temperature Corrosion of Copper in the Presence of Graphene. *ACS Nano* **7,** 6939–6947 (2013).
208. Sun, W., Wang, L., Wu, T., Wang, M., Yang, Z. *et al.* Inhibiting the corrosion-promotion activity of graphene. *Chem. Mater.* **27,** 2367–2373 (2015).
209. Sun, W., Wang, L., Wu, T., Pan, Y. & Liu, G. Communication—Multi-Layer Boron Nitride Nanosheets as Corrosion-Protective Coating Fillers. *J. Electrochem. Soc.* **163,** C16–C18 (2016).
210. Liu, Z., Gong, Y., Zhou, W., Ma, L., Yu, J. *et al.* Ultrathin high-temperature oxidation-resistant coatings of hexagonal boron nitride. *Nat. Commun.* **4,** 2541 (2013).
211. Li, L. H., Xing, T., Chen, Y. & Jones, R. Boron Nitride Nanosheets for Metal Protection. *Adv. Mater. Interfaces* **1,** 1–6 (2014).
212. Yi, M., Shen, Z., Zhao, X., Liang, S. & Liu, L. Boron nitride nanosheets as oxygen-atom corrosion protective coatings. *Appl. Phys. Lett.* **104,** (2014).
213. Lopez, B. G., Valdez, S. B., Zlatev, K. R., Flores, P. J., Carrillo, B. M. *et al.* Corrosion of metals at indoor conditions in the electronics manufacturing industry. *Anti-Corrosion Methods Mater.* **54,** 354–359 (2007).
214. Wang, S., Cheng, Y., Wang, R., Sun, J. & Gao, L. Highly thermal conductive copper nanowire composites with ultralow loading: Toward applications as thermal interface materials. *ACS Appl. Mater. Interfaces* **6,** 6481–6486 (2014).
215. Park, J. S., An, Y. J., Shin, K., Han, J. H. & Lee, C. S. Enhanced thermal conductivity of epoxy/three-dimensional carbon hybrid filler composites for effective heat dissipation. *RSC Adv.* **5,** 46989–46996 (2015).
216. Lian, G., Tuan, C. C., Li, L., Jiao, S., Wang, Q. *et al.* Vertically Aligned and Interconnected Graphene Networks for High Thermal Conductivity of Epoxy Composites with Ultralow Loading. *Chem. Mater.* **28,** 6096–6104 (2016).
217. Yao, Y., Zeng, X., Pan, G., Sun, J., Hu, J. *et al.* Interfacial Engineering of Silicon Carbide Nanowire/Cellulose Microcrystal Paper toward High Thermal Conductivity. *ACS Appl. Mater. Interfaces* **8,** 31248–31255 (2016).
218. Eyassu, T., Hsiao, T.-J., Henderson, K., Kim, T. & Lin, C.-T. Molecular Cooling Fan: Factors for Optimization of Heat Dissipation Devices and Applications. *Ind. Eng. Chem. Res.* **53,** 19550–19558 (2014).
219. Li, Q., Guo, Y., Li, W., Qiu, S., Zhu, C. *et al.* Ultrahigh thermal conductivity of assembled aligned multilayer graphene/epoxy composite. *Chem. Mater.* **26,** 4459–4465 (2014).
220. Fang, X., Fan, L. W., Ding, Q., Wang, X., Yao, X. L. *et al.* Increased thermal conductivity of eicosane-based composite phase change materials in the presence of graphene nanoplatelets. *Energy & Fuels* **27,** 4041–4047 (2013).

221. Shtein, M., Nadiv, R., Buzaglo, M., Kahil, K. & Regev, O. Thermally conductive graphene-polymer composites: size, percolation and synergy effects. *Chem. Mater.* 150226101352003 (2015). doi:10.1021/cm504550e
222. Hsu, P. C., Liu, X., Liu, C., Xie, X., Lee, H. R. *et al.* Personal thermal management by metallic nanowire-coated textile. *Nano Lett.* **15,** 365–371 (2014).
223. Gui, X., Wei, J., Wang, K., Cao, A., Zhu, H. *et al.* Carbon nanotube sponges. *Adv. Mater.* **22,** 617–621 (2010).
224. Qin, M., Feng, Y., Ji, T. & Feng, W. Enhancement of cross-plane thermal conductivity and mechanical strength via vertical aligned carbon nanotube@graphite architecture. *Carbon N. Y.* **104,** 157–168 (2016).
225. Sasaki, R. & Shintani, K. Hardness of Pillared-Graphene Nanostructures via Indentation Simulation. *MRS Adv.* **2,** 45–50 (2017).
226. Chen, J., Hamon, M. A., Hu, H., Chen, Y., Rao, A. M. *et al.* Solution properties of single-walled carbon nanotubes. *Science* **282,** 95–8 (1998).
227. Zhi, C., Bando, Y., Tang, C., Honda, S., Sato, K. *et al.* Covalent functionalization: towards soluble multiwalled boron nitride nanotubes. *Angew. Chem. Int. Ed. Engl.* **44,** 7932–5 (2005).
228. Laibinis, P. & Whitesides, G. Comparison of the structures and wetting properties of self-assembled monolayers of n-alkanethiols on the coinage metal surfaces, copper, silver, and gold. *J. Am. Chem. Soc.* **113,** 7152–7167 (1991).
229. Vericat, C., Vela, M. E., Benitez, G., Carro, P. & Salvarezza, R. C. Self-assembled monolayers of thiols and dithiols on gold: new challenges for a well-known system. *Chem. Soc. Rev.* **39,** 1805 (2010).
230. Frey, S., Shaporenko, A., Zharnikov, M., Harder, P. & ALLARA, D. L. Self-assembled monolayers of nitrile-functionalized alkanethiols on gold and silver substrates. *J. Phys. Chem. B* **107,** 7716–7725 (2003).
231. Yegin, C., Nagabandi, N., Feng, X., King, C., Catalano, M. *et al.* Metal-Organic-Inorganic Nanocomposite Thermal Interface Materials with Ultra-Low Thermal Resistances. *ACS Appl. Mater. Interfaces* **9,** 10120–10127 (2017).
232. Ordonez-Miranda, J., Alvarado-Gil, J. J. & Yang, R. The effect of the electron-phonon coupling on the effective thermal conductivity of metal-nonmetal multilayers. *J. Appl. Phys.* **109,** 94310 (2011).
233. Wang, Y., Yang, C., Pei, Q. X. & Zhang, Y. Some Aspects of Thermal Transport across the Interface between Graphene and Epoxy in Nanocomposites. *ACS Appl. Mater. Interfaces* **8,** 8272–8279 (2016).
234. Schiotz, J., Tolla, F. D. Di & Jacobsen, K. W. Softening of nanocrystalline metals at very small grain sizes. *Nature* **391,** 561–563 (1998).
235. Sita, L. R., Terry, K. W. & Shibata, K. Sandorfy Hueckel Molecular Orbital Approximation for Modeling the Electronic Structures of Long-Chain Polystannanes. *J. Am. Chem. Soc.* **117,** 8049–8050 (1995).
236. Bukalov, S. S., Leites, L. A., Lu, V. & Tilley, T. D. Order - Disorder Phase Transition in Poly (di- n -butylstannane) Observed by UV - Vis and Raman Spectroscopy. 1757–1761 (2002). doi:10.1021/ma011249j
237. Takeda, K. & Shiraishi, K. Electronic structure of chain-like polystannane. *Chem.*

Phys. Lett. **195,** 121–126 (1992).
238. Harrypersad, S., Liao, L., Khan, A., Wylie, R. S. & Foucher, D. A. Linear Oligostannanes: A Synthetic and TD-DFT Study. *J. Inorg. Organomet. Polym. Mater.* **25,** 515–528 (2015).
239. Drenth, W., Noltes, J. G., Bulten, E. J. & Creemers, H. M. J. C. Ultraviolet Absorption Spectra of Perethylpolygermanes andPolystannanes. *J. Organomet. Chem.* **17,** 173–174 (1969).
240. Choy, C. L. Thermal Conductivity of Polymers. *Polymer (Guildf).* **18,** 984–1004 (1977).
241. Lu, V. Y. & Tilley, T. D. Poly(diaryl)stannanes: Influence of substituents on the σ - σ * transition energy. *Macromolecules* **33,** 2403–2412 (2000).
242. Nika, D. L., Pokatilov, E. P., Askerov, A. S. & Balandin, A. A. Phonon thermal conduction in graphene: Role of Umklapp and edge roughness scattering. *Phys. Rev. B - Condens. Matter Mater. Phys.* **79,** 1–12 (2009).
243. Lu, V. & Tilley, T. D. -Conjugated Polymers: Poly(diarylstannanes). *Macromolecules* **29,** 5763–5764 (1996).
244. Feng, X., King, C., Devoto, D., Mihalic, M. & Narumanchi, S. Investigation of thermal interface materials using phase-sensitive transient thermoreflectance technique. *Thermomechanical Phenom. Electron. Syst. -Proceedings Intersoc. Conf.* 1296–1307 (2014). doi:10.1109/ITHERM.2014.6892430
245. Incropera, F. P., Lavine, A. S. & DeWitt, D. P. *Fundamentals of Heat and Mass Transfer*. (John Wiley & Sons Inc., 2011).
246. Feng, X., King, C. & Narumanchi, S. General multilayer heat transfer model for optical-based thermal characterization techniques. *Int. J. Heat Mass Transf.* **93,** 695–706 (2016).
247. Malen, J. A., Baheti, K., Tong, T., Zhao, Y., Hudgings, J. A. *et al.* Optical Measurement of Thermal Conductivity Using Fiber Aligned Frequency Domain Thermoreflectance. *J. Heat Transfer* **133,** 81601 (2011).

APPENDIX

Phase-sensitive transient thermoreflectance measurements

Besides the laser flash diffusivity technique, a phase-sensitive transient thermoreflectance (PSTTR) technique was used to measure the thermal properties (including thermal contact resistances and overall thermal resistance/resistivity) of the hybrid nanocomposite materials. The nanocomposite samples were grown on to silicon wafers at varying thicknesses up to 50 μm, following the physical vapor deposition of a 300 nm copper layer on the wafers for electrical conductivity. PSTTR is a modulated optical pump-probe technique that utilizes two lasers to study the thermal properties of multi-layered structures. A pump laser is modulated by a waveform generator and the working frequencies are determined based on the thermal property and thickness of the test samples. The modulated pump laser is directed on to one of the sample surfaces and serves as a heat source. The laser has a $1/e^2$ radius of about 1.5 mm and the maximum power of the laser is 5W, yielding a maximum heat flux of about 2.8 W/mm^2. The induced thermal wave penetrates through the sample, causing the temperature on the opposite surface to oscillate following the same periodicity. A probe laser is applied to this opposite surface to monitor the thermoreflectance change which is proportional to the temperature oscillation. A photodiode captures the reflected probe laser and transmits the optical signal into a lock-in amplifier, which compares the probe laser signal with the original modulation from the waveform generator to extract the phase shift. A schematic of the PSTTR experiment is shown in Figure 54, and further details about the PSTTR technique are described in another publication.[244]

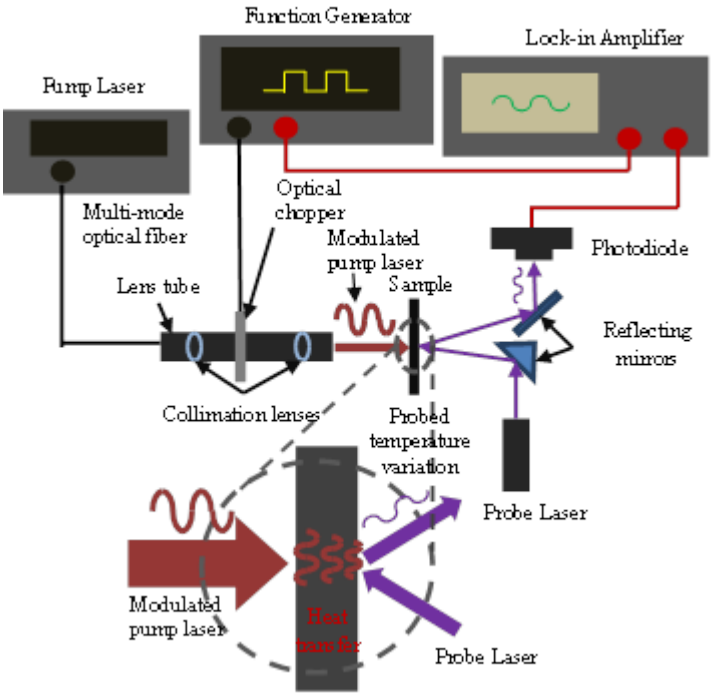

Figure 54 Schematic of the PSTTR technique

Table 13 Parameters used in the heat transfer model to fit the PSTTR data

Materials	Layer thickness (μm)	Density (kg/m^3)	Specific heat (J/kg·K)	Bulk Thermal conductivity (W/m·K)
Silicon[2]	100	2330	712	148
Aluminum[245]	3 ~ 5	2702	903	237
Hybrid nanocomposite	30 ~ 50	7332	440	232

If the thickness, specific heat and density of the hybrid nanocomposite material are accurately measured, then the bulk thermal conductivity can be derived by fitting the relevant heat transfer model to the extracted phase shift. Table 13 lists the parameters used in the heat transfer model to fit the PSTTR data. The hybrid nanocomposite samples were fabricated in two configurations – single-sided and bonded, as demonstrated in Figure 55a and c, and was characterized following a two-step strategy to comprehensively evaluate the thermal properties and performance. First, because the nanocomposite is relatively thin and soft, it needed to be supported for the PSTTR measurements. Therefore, the hybrid nanocomposite material was electrodeposited onto a substrate to form a single-sided structure. In this research, silicon was used as the substrate because the physical and thermal properties have been comprehensively studied, as listed in Table 13. Another advantage associated with silicon is that a highly-polished surface can be obtained, which enhances the specular reflection of the probe laser. The nanocomposite thickness varied from 30 to 50 μm, while the silicon substrate was 100 μm thick (Figure 55b). For these single-sided samples, the bulk thermal conductivity of the hybrid nanocomposite and the interfacial contact resistance were the two fitting parameters. Once these parameters were obtained using PSTTR, the hybrid nanocomposite was then sandwiched between two silicon substrates to fabricate a bonded structure (Figure 55c). The purpose of preparing the bonded structure was to evaluate the nanocomposites thermal performance when it was being used in a TIM configuration - *i.e.* sandwiched between two substrates. The single sided sample was placed in a cylindrical die, and rapidly bonded to a bare silicon substrate with a molten aluminum layer (4-5 μm) at 650 ^{O}C temperature under nitrogen

atmosphere. The physical/thermal properties of the aluminum layer are listed in Table 13, and it is counted as part of the entire interfacial layer. Therefore, when developing the heat transfer model, the interfacial layer was considered to have two solid layers (hybrid nanocomposite and aluminum) and three interfaces. Given that the bulk thermal conductivity of the hybrid nanocomposite, and the contact resistance between the hybrid nanocomposite and silicon substrate were already identified by the characterization of the single-sided samples, only the contact resistances of the other two interfaces (Si-Al and Al-nanocomposite) needed to be determined for the bonded samples. Hence, the four critical unknown parameters were acquired from two independent fitting procedures, and the reliability of the results was consequently very good. By summing the bulk thermal resistances and interfacial contact resistances, the total thermal resistance of the interfacial layer was calculated.

As stated previously, a heat transfer model is required to fit the experimental data, and extract values of the unknown parameters of interest. In this work, the single-sided and bonded samples contained different number of layers. Normally, heat transfer in different configurations may demand different models. Here, due to the similarity between the two structures, we utilize a general heat transfer model that is capable of deriving the phase shift in the structures with arbitrary number of layers. Details on the development of the heat transfer model and the solutions can be found elsewhere.[246] The general solution is presented in Equation 13:

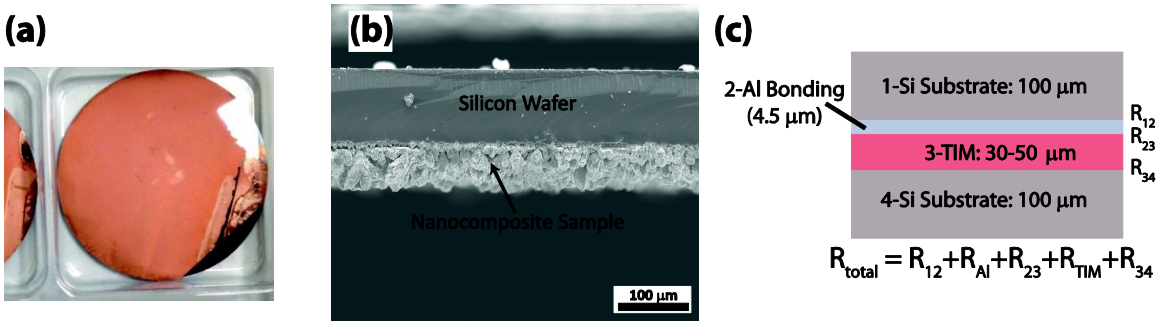

Figure 55 Cu/f-BNNS nanocomposite TIMs deposited on silicon substrate. (b) a scanning electron micrograph (SEM) of the single-sided samples, in which multiple thickness measurements are made and the average is used in the characterization, and (c) cross-section of sandwich configuration of the TIMs between two silicon wafers. Thin aluminum layer was used for diffusion bonding

Φ

$$= \frac{\pi}{4} + \sum_{i=1}^{n} d_i \sqrt{\frac{\pi f}{\alpha_i}} +$$

$$tan^{-1}\left[\frac{-\sum_{i_1,i_2,\ldots i_{n-1}\in\{0,1\}} \mathrm{Im}\left[(1-j)^{i_1+i_2+\cdots+i_{n-1}}\right]\mathcal{RR}_{12}{}^{i_1} * \mathcal{RR}_{23}{}^{i_2} * \cdots * \mathcal{RR}_{n-1,n}{}^{i_{n-1}}}{1+\sum_{i_1,i_2,\ldots i_{n-1}\in\{0,1\}} \mathrm{Re}\left[(1-j)^{i_1+i_2+\cdots+i_{n-1}}\right]\mathcal{RR}_{12}{}^{i_1} * \mathcal{RR}_{23}{}^{i_2} * \cdots * \mathcal{RR}_{n-1,n}{}^{i_{n-1}}}\right] \quad (16)$$

Here, f is the frequency; α_i and d_i are the thermal diffusivity and the thickness of the *i*-th layer, respectively. $RR_{i,i+1}$ is a lumped parameter that includes all the known and fitting parameters in the adjacent layers i and i+1. This treatment enables convenient calculation of the overall phase shift Φ using programming software such as FORTRAN or MATLAB. The samples in this work contained either two or four layers, so i equals 2 or 4. By substituting the numbers into Equation 4, the relevant theoretical phase shifts were calculated, and were then fitted to the experimental data to determine the best value(s) of the fitting (unknown) parameters. A typical fitting graph is shown in Figure 56. In this Figure, discrete experimental data points (blue circles) are very close to the

theoretical phase shift values (red solid line) throughout the entire frequency range. Varying the fitting parameters causes the shape or slope of the solid line to change. When the difference between the theoretical solution and the experimental data reaches a minimum value, the values of the fitting/unknown parameters are considered to have been obtained.

Samples of various thicknesses and incorporating various ligands were prepared for a comprehensive investigation of the thermal properties of the hybrid nanocomposites. The fitted bulk thermal conductivity of the nanocomposite ranged from 211 to 277 W/m·K, at the same level as metallic materials and showing significant improvement compared to the polymer-based or solder TIMs. The thermal contact resistances, by virtue of the electrodeposition process and the material's high mechanical compliance, were also significantly reduced to a competitively low level of around 0.1 $mm^2 \cdot K/W$. By adjusting the thickness and BNNS concentration, the total thermal resistance of the valid bonded samples ranged from 0.38 to 0.56 $mm^2 \cdot K/W$ for 30 to 50 μm BLT, respectively, which are lower than those of almost all traditional TIMs for comparable BLT. For comparison, a high-performance commercial-grade thermal grease that we characterized had a thermal resistance around 15 to 30 $mm^2 \cdot K/W$[192] for 30 to 50 μm bondline thicknesses. A novel thermoplastic film material incorporating highly-aligned micron-sized fibers yielded a thermal resistance of about 10 $mm^2 \cdot K/W1$ for 50 to 75 μm bondline thicknesses. Therefore, the hybrid nanocomposite TIM exhibits superior thermal properties which greatly enable the possibility of its application in high power-density components or harsh-environment electronics.

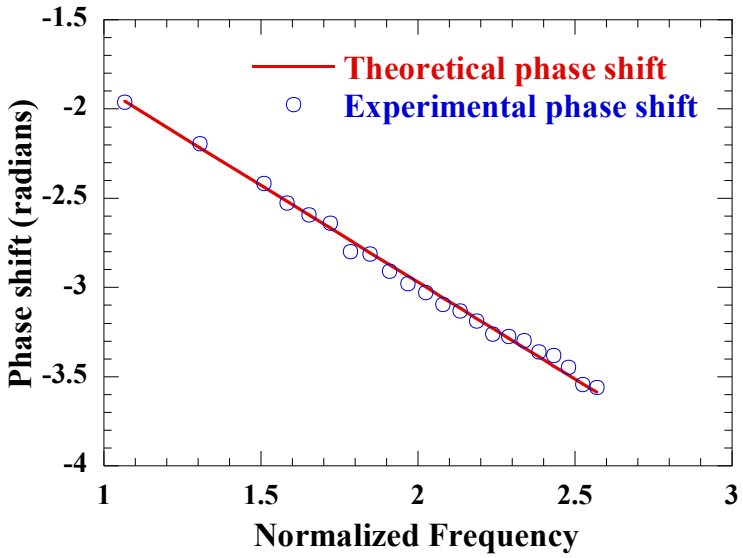

Figure 56 The dependence of phase shifts on normalized frequency for one selected bonded sample. The red solid line is the theoretical phase shift based on the best-fitted value of the fitting parameters, and the circles are experimental data points for the phase shift

To perform the PSTTR measurements, an automatic data acquisition system was employed to collect the experimental data. For each frequency, the sampling time was 60 seconds and the sampling rate was 10 Hz. Hence, there were a total of 600 extracted phase shifts and the average of them was recorded as the phase shift for any given frequency. The random uncertainty with the data acquisition system was estimated to be 5 degrees, while the systematic uncertainty was about 1 degree. In addition to the uncertainty associated with the measurements, the regression analysis also introduced uncertainty into the system. When fitting the model to the experimental data, the difference between the modeling and experimental results was minimized to achieve the best fit, thereby determining the values of the fitting parameters. However, errors came in to the fitting process because of uncertainties in the other modeling parameters (known and unknown).

We implemented a methodology from Malen et al.'s work[247] for the uncertainty analysis. The uncertainty of the fitting parameter was estimated from the uncertainties in the modeling parameters. After the best fit was achieved, each of the modeling parameters was perturbed by a small quantity (its uncertainty), and the regression process was repeated to find the new values of the fitting parameters. Then, the difference between the new and old values was the uncertainty from the fitting process itself. Using this methodology and combining the fitting uncertainty with the experimental uncertainty (random and systematic uncertainty), the overall uncertainty at 95% confidence level was calculated for each fitting parameter.

The experiments were completed using an automated data acquisition system that was built to collect the amplitude and phase extracted from the lock-in amplifier. For each frequency generated from the function generator, the sampling time was 60 seconds and the sampling rate was 10 Hz. Then, the average value of 600 samples that were collected was recorded as the amplitude and phase associated with this frequency. The data acquisition system is estimated to have about 5 degrees random uncertainty. The lock-in amplifier has a systematic uncertainty of about 1 degree. In addition, the regression process to analyze the experimental data also is an important source of error. The reason is that when fitting the experimental data and theoretical results, other modeling parameters, known or unknown, are applied with different levels of uncertainty.

Here, the uncertainty of the to-be-determined parameters is estimated from the uncertainties in the modeling parameters[244]. After determining the best fit, each of the modeling parameters is perturbed by a small quantity (its uncertainty) and the regression

process is repeated to find the new fitted value of the to-be-determined unknowns. Then the difference between the new and old values is the uncertainty from the fitting process used to determine the unknown parameters. Using this methodology and combining fitting uncertainty with the measurement uncertainty (random and systematic uncertainty), the uncertainty of thermal conductivity at 95% confidence level is calculated to be 27%, while that for the R12 and R23 is 31% and 39%, respectively. This leads to an uncertainty of about 16% for the total thermal resistance.